Designing donor-acceptor oligomers and small molecules for photovoltaic applications: Insights from computational studies

A thesis submitted to the Indian Institute of Technology Guwahati for the degree of Doctor of Philosophy

Author:

Mohd Shavez

Supervisor:

Dr. Aditya N. Panda

Department of Chemistry

Indian Institute of Technology Guwahati

Guwahati - 781039

Declaration

I declare that the thesis entitled **"Designing donor-acceptor oligomers and small molecules for photovoltaic applications: Insights from computational studies"** submitted by me for the degree of Doctor of Philosophy is the record of research work carried out by me during the period from July 2016 to September 2021 under the guidance and supervision of Dr. Aditya N. Panda, professor, Indian Institute of Technology Guwahati and has not formed the basis for the award of any degree, diploma, associateship and fellowship, titles in this University or in any other University or other similar institutions of higher learning.

Mohd Shavez
Roll No.: 166122041

INDIAN INSTITUTE OF TECHNOLOGY GUWAHATI
Department of Chemistry
Academic Complex, North Guwahati
Guwahati - 781039 India

Certificate

This is to certify that the thesis entitled "*Designing donor-acceptor oligomers and small molecules for photovoltaic applications: Insights from computational studies*" submitted for the award of degree of Doctor of Philosophy (Ph.D.) by **Mohd Shavez** is the record of research work carried out by him during the period July 2016 to July 2021 under my guidance and supervision, and this work has not formed the basis for the award of any degree, diploma, associateship, fellowship or other titles in this University or in any other University or other similar institutions of higher learning.

Dr. Aditya N. Panda
Thesis supervisor

This dissertation is dedicated to my beloved parents for their endless love, support and encouragement.

Acknowledgements

I take this opportunity to express my profound gratitude and deep regards to my supervisor **Prof. Aditya N. Panda** IIT Guwahati, Assam, for giving me the opportunity to work on my PhD studies in his group. I would like to thank him for his encouragement and constant support throughout my PhD work period.

Besides my advisor, I would like to thank the rest of my thesis committee members: **Dr. Manabendra Sarma**, **Prof. Ashish Kumar Gupta**, and **Prof. Kalyanasis Sahu**, for their insightful comments and encouragement.

I am thankful to IIT Guwahati for providing the PARAM-ISHAN super-computing facility helping me to carry out my computational studies. I am also grateful to IIT Guwahati for financial support.

I thank my labmates Bishwanth and Iban for their company and cooperation in laboratory. I thank Shaad, Asif, Saghir, Gayyur, Adil, and Nasim for motivating and encouraging me during my PhD days.

I am thankful to all of my college, university and IIT friends. I feel myself very lucky as I enjoyed my phd journey with Saghir, Nasim, Munendra, Mehboob, Rashid, Suhaib, Rabindernath, Saddam, and Tipu.

Finally and most importantly, I thank all the members of my family, especially my parents, sisters and brothers for their unconditional support and encouragement.

Synopsis

In recent times, the performance of bulk heterojunction (BHJ) architecture based organic solar cells (OSCs) has improved tremendously, and devices with power conversion efficiencies (PCEs) ∼18% have been reported. A typical BHJ structure comprises of a blend of conjugated polymer/small-molecule as charge donor and fullerene/non-fullerene system as charge acceptor. For increasing PCE of OSCs, many strategies have been employed. However, designing an appropriate active layer material with required electronic and optical properties is still a challenging task. Computational studies, at this juncture, are of great help to pre-scrutinize the organic molecules, and choose the appropriate donor (D) - acceptor (A) combinations before carrying out the experiments. Based on the type of donor molecules used in the active layers, OSCs can be divided into two classes: polymer based and small molecule (SM) based solar cells. In this thesis, we explore the structures, optoelectronic, and charge transfer properties of a variety of systems containing either alternating/random conjugated oligomer or SM based donors with either fullerene or non-fullerene acceptors (NFAs). For the donors, we have chosen the benzodithiophene (BDT) based oligomers and SMs. BDT-based molecular systems have been at the forefront of organic photovoltaic (OPV) cell design, and studying the effects of modification of BDT-based donors would add to our understanding. Considering the sizes of the studied systems in mind, we have used the density functional theory (DFT) and time-dependent DFT (TDDFT) based methods in our studies. Below we provide a chapter-wise overview of the thesis.

Chapter 1: *Introduction*

The chapter 1 starts with an overview of OSC device architectures. This is followed by a brief discussion of the working principle of a typical BHJ based device. Various

parameters such as open-circuit voltage (V_{oc}), current density and fill-factor used for characterization of the OSCs are also discussed in this chapter.

Chapter 2: *Theoretical and computational methods*

This chapter presents the theoretical and computational methods used in the thesis. Basics of the Hartree-Fock theory, DFT and TDDFT are briefly mentioned. Few commonly used DFT functionals for studying ground and excited state properties are also mentioned. The Marcus theory is utilized to compute the rates of charge transfer in the thesis. In this chapter, the Marcus theory is presented in brief. In addition, various parameters in the Marcus' rate formula such as reorganization energy, electronic coupling and free energy changes are also discussed.

Chapter 3: *Designing fluorinated benzodithiophene-triazole based oligomers for high open circuit voltage in organic photovoltaics*

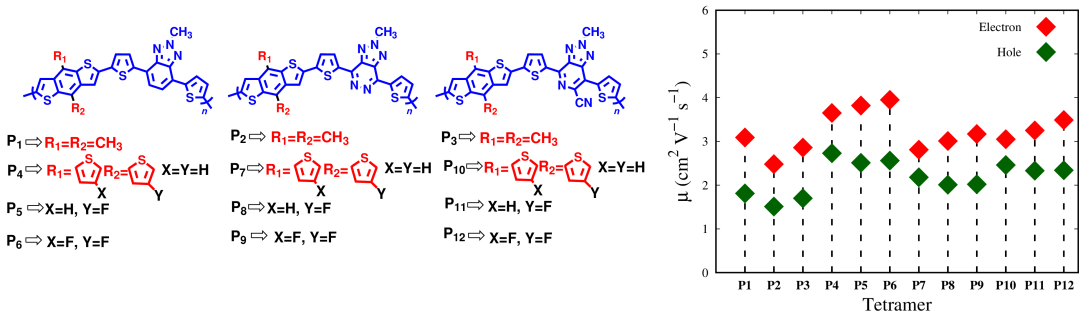

This chapter presents structural, optoelectronic, and charge transport properties of a set of conjugated oligomers in which the monomer unit consists of a BDT (or a modified BDT), a thiophene π spacer, and benzotriazole (TAZ) (or its derivative) as an acceptor. Starting with **P1**, **P2** and **P3**, shown in the figure above, we have replaced the -CH_3 groups by thienyl, monofluorinated thienyl and bifluorinated thienyl rings. This results in three new monomers for each of the parent systems. It should be emphasized that thienyl rings have been shown in the literature to have a positive effect on photovoltaic properties. In addition, many recent reports have shown that fluorination of donor units is beneficial for obtaining

better performances. Our results show that the increase in the number of fluorine atoms in the side chain of BDT lowers both the highest occupied molecular orbital (HOMO) and the lowest unoccupied molecular orbital (LUMO) levels. In addition, fluorine substituted oligomers exhibit higher V_{oc} values. Hole mobilities are larger in the newly designed set of oligomers than in the parent systems. Therefore, it is concluded that better PCEs can be expected in the devices with these newly designed oligomer donors.

Chapter 4: *Halogenation of the side chains in donor-acceptor based small molecules for photovoltaic applications*

In this chapter, structural and optoelectronic properties of a series of BDT-based SM donors, and charge transfer properties of the blends of these SM donors with a [6,6]-phenyl-C61-butyric acid methyl ester (**PCBM**) acceptor are presented. SM donors have many advantages over the polymer donors such as their easier method

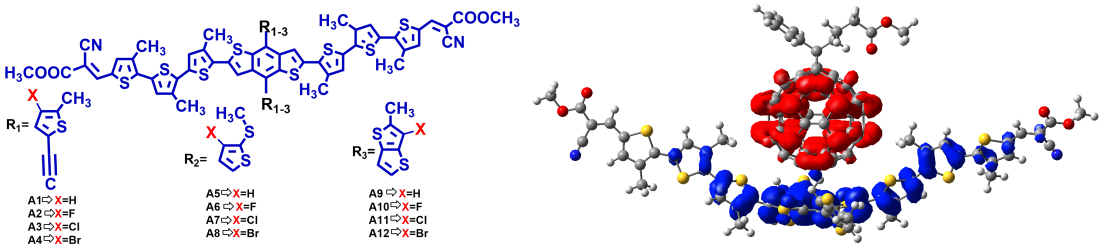

of synthesis, high purity, well-defined molecular structure and large charge carrier mobilities. Typical architecture of SM donor consists of an A-D-A core flanked by end-capping units. While two acceptors help in increasing the electron affinity, end-capping assists in π-conjugation. Here, we have chosen three experimentally studied A-D-A type systems denoted as **A1**, **A5**, and **A9**, shown in the figure above. Starting with these parent SMs, new SMs are designed by substituting one hydrogen atom in each thiophene ring on the lateral side chains of the BDTT unit by either fluorine or chlorine or bromine atoms. Our DFT studies using hybrid functionals show that these newly designed SMs have deeper HOMO levels and hence, higher V_{oc}. In addition, in the blends of halogenated SMs with **PCBM**, energy losses are less, charge transfer rates (k_{CT}) are larger, and charge recombination

rates (k_{CR}) are smaller than the parent systems. Therefore, halogen-substituted SMs are more suitable for the active layers of OSCs, and can be expected to improve PCEs of OSCs, in accordance with many recently reported results.

Chapter 5: *Effects of π bridge units on the properties of donor-π-acceptor type benzodithiophene- thienothiophene based oligomers*

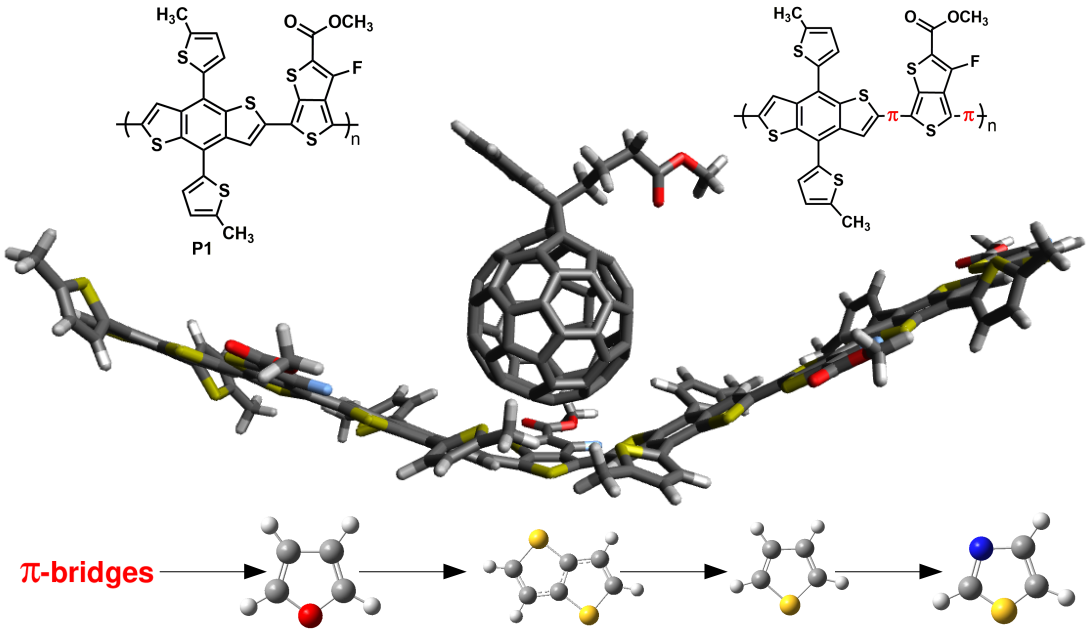

This chapter explores the effect of insertion of a variety of π bridges between donor and acceptor components of an alternating polymer donor. Experimentally studied [4,8-bis(5-(2-ethylhexyl)thiophen-2-yl)benzo[1,2-b:4,5-b′] dithiophene-*alt*-3-fluorothieno[3,4-b]thiophene-2-carboxylate] alternating polymer was chosen for this purpose. As the name suggests, this molecule contains a modified BDT (denoted as BDTT in this thesis) as donor unit and fluorothieno-thiophene-2-carboxylate (TT-F) as an acceptor. For our computational studies, the ethylhexyl groups in the side chains are replaced by methyl groups. π bridge units such as furan, thienothiophene, thiophene, and thiazole are inserted between the BDTT and TT-F units. As an acceptor, the widely used molecule **PCBM** is chosen. For the donor oligomers, ground state and excited state studies are carried out using the PBE0 and HSE06 functionals, respectively. For the donor/acceptor blends, on the other hand, CAM-B3LYP functional is used for all the calculations. Our

results show that the thiazole π bridge based oligomer was more planar compared to the other three π-bridged oligomers. Thiazole π bridge based oligomer is planar, and this results in the deepest HOMO value and the highest V_{oc} for the thiazole based oligomer among all. In addition, rates of charge recombinations in blends of thiophene and thiazole-based oligomers with **PCBM** are smaller than in blends of furan and thienothiophene based oligomers with **PCBM**. Hence, thiophene and thiazole π bridge based oligomers can be considered to be more suitable for OSC active layers.

Chapter 6: *Random donor and non-fullerene acceptor based active layer: effects of insertion of various π linkers*

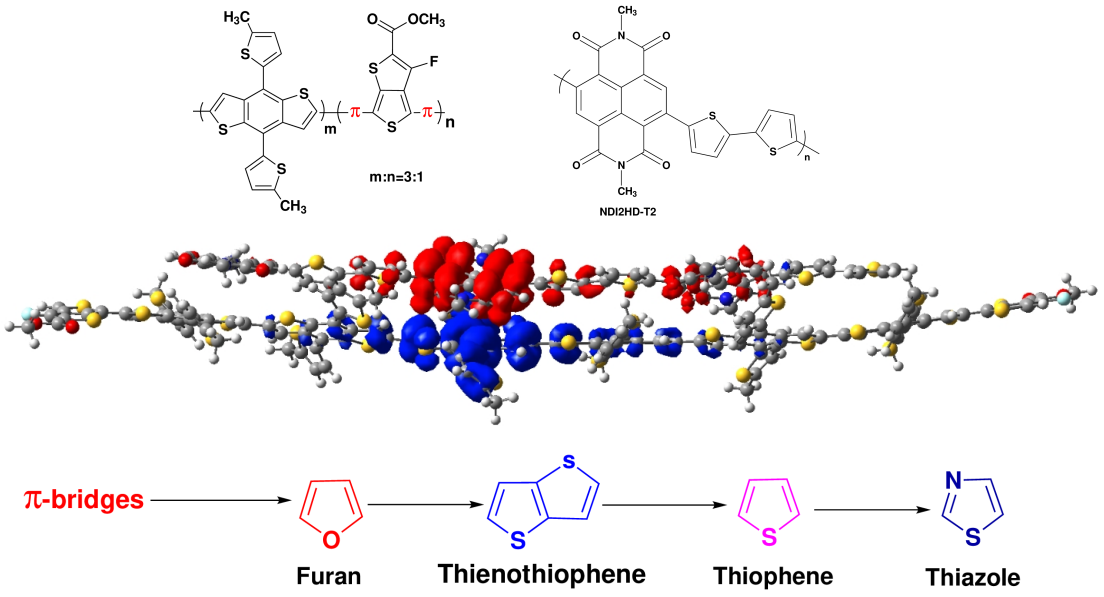

In the previous chapter, an alternating co-oligomer based on BDTT and TT-F was used. In the present chapter, we pick a random co-oligomer based on BDTT and TT-F (denoted as BDTT-*ran*-TT-F) with a 3:1 D/A ratio to study the effect of incorporating π bridges between BDTT and TT-F. Recent reports show that performances of devices based on random oligomers are better than the devices based on alternating polymers. As in the previous chapter, furan, thienothiophene, thiophene, and thiazole units were taken as π bridges. However, in this

case a non-fullerene acceptor, poly{[N,N′-bis(2-hexyldecyl)-naphthalene-1,4,5,8-bis (dicarboximide)-2,6-diyl]-*alt*-5,5′-(2,2′-bithiophene)} (**NDI2HD-T2**) is chosen. **NDI2HD-T2** denoted as **NDI** in this thesis. NFAs have better tunability of the energy levels, low cost, better stability, and stronger absorption in the visible region compared to the fullerene based acceptors. Our results show that the donating strengths of the π bridge units are the following order: furan > thiophene > thienothiophene > thiazole. Exciton binding energy was found to be significantly altered by the presence of additional π spacers in the D/A systems. Charge transfer rates are larger in furan/**NDI** and thiazole/**NDI** systems compared to the thienothiophene/**NDI** and thiophene/**NDI** blends. In addition, k_{CR} value is the smallest in thiazole/**NDI** system. Hence, thiazole/**NDI** based random oligomers can be considered to be a very promising candidate as a π-space for OPV fabrication.

Chapter 7: *Summary and conclusions*

In this chapter, a brief summary of the thesis is presented. Two routes, halogenation and insertion of π bridges, are undertaken to understand the geometric and structural effects on the optoelectronic and photovoltaic properties of donors and blends. In particular, BDT based alternating and random donor oligomers, and **PCBM** or **NDI** acceptors are chosen in our studies. Our first work indicates that fluorinated-based BDT-TAZ oligomers have suitable properties for their use in OSCs. Results of Chapter 4 show that halogen substituted SMs have deeper HOMO levels and higher V_{oc} values than the parent molecules. These newly designed SMs are found to be more suitable for solar cell devices. In Chapter 5, effects of insertion of π bridge units such as furan, thienothiophene, thiophene, and thiazole between the alternating BDTT-based oligomers are studied. Thiazole π bridge was found to be the best spacer among all. Results of Chapter 6 show that the optoelectronic and charge transfer properties of random D-A oligomers with **NDI** as an acceptor can be suitably tuned with different π bridges.

List of articles published/submitted

1. Mohd Shavez and Aditya N. Panda, Assessing effects of different π-bridges on photovoltaic performance of random benzodithiophene-thienothiophene donor and non-fullerene acceptor based active layer, *J. Phys. Chem. A*, **2021**, 125, 9852–9864.

2. Mohd Shavez, Anuj Kumar Ray and Aditya N. Panda, Effect of halogenation of the side chains in donor-acceptor based small molecules for photovoltaic applications: Energetics and charge-transfer properties from DFT/TDDFT studies, *Chemistry Select*, **2021**, 6, 5254–5265.

3. Mohd Shavez and Aditya N. Panda, Effects of π-bridge units on the properties of donor-π-acceptor type benzodithiophene-thienothiophene based polymers for organic solar cells, *Chemical Physics Letters*, **2020**, 756, 137810–137818.

4. Mohd Shavez, Juri Goswami and Aditya N. Panda, Effect of fluorination of the donor unit on the properties of benzodithiophene-triazole based donor-acceptor systems for polymer solar cells: A computational investigation, *Computational and Theoretical Chemistry*, **2019**, 1165, 112564–112572.

Contents

Symbols and abbreviations

α	alpha
β	beta
χ	chi
δ	Lowercase delta
Δ	Uppercase delta
$\Delta\mu$	Difference in dipole moment of ground and first ICT states
ϵ	epsilon
η	eta
λ	lambda
μ	mu
μ_{g}	Ground-state dipole moment
μ_{e}	Excited-state dipole moment
ρ	rho
σ	sigma
π	pi
ϕ	phi
ψ	psi
Ψ	Psi
%	Percentage

Å	Angstrom
BHJ	Bulk-heterojunction
ICT	Intermolecular charge transfer
CAM	Coulomb-attenuating method
DFT	Density functional theory
DFT-D3	Density Functional Theory including Grimme's D3 version of dispersion
E_{b}	Exciton binding energy
$E^{1}_{\mathrm{g,Blend}}$	First excitation energy of blend
$E_{\mathrm{g,Blend}}$	Excitation energy of blend
$E^{\mathrm{ICT}}_{\mathrm{g,blend}}$	Excitation energy of first ICT state of blend
E_{HOMO}	Energy of the HOMO
E_{LUMO}	Energy of the LUMO
E^{1}_{g}	First excitation energy
f_{osc}	Oscillator strength
FF	Fill factor
FMO	Frontier molecular orbital
HF	Hartree-Fock
GGA	Generalized gradient approximation
HOMO	Highest occupied molecular orbital
LUMO	Lowest unoccupied molecular orbital
J	Current
J_{SC}	Output current at short circuit condition

IP	Ionization potential
ITO	Indium tin oxide
K	Kelvin
KS	Kohn-Sham
LDA	Local-density approximation
LSDA	Local spin-density approximation
MO	Molecular orbital
OFET	Organic field-effect transistor
OLED	Organic light-emitting diode
OPV	Organic photovoltaics
OSC	Organic solar cell
PCE	Power conversion efficiency
TDDFT	Time-dependent density functional theory
UV-Vis	ultraviolet-visible
V	Voltage
V_{OC}	Open-circuit voltage
Vis-NIR	Visible near-infrared

List of Figures

List of Tables

Chapter 1

Introduction

In recent decades, there has been a massive increase in energy demand, and currently, this demand is being met by combustion of fossil fuels. Fossil fuels such as oil, gas, coal, and other non-renewable energy are the main energy sources. However, fossil fuels severely affect our environment by increasing the CO_2 concentration which has a terrible impact on our planet. One possible solution to this problem is to find clean, cheap, and renewable energy resources. Solar energy is the most promising energy source among all renewable energy resources. The Sun represents an ideal source of energy from which abundant and clean energy can be obtained. Energy from the sunlight can be collected by photovoltaic technologies, and this is the most promising concept for a scalable power generation to overcome increasing global energy demand.

Solar cells are the devices used for converting sunlight into electricity. Those are also called photovoltaic devices. Photovoltaic devices based on inorganic materials such as mono and multi-crystalline silicon, gallium arsenide (GaAs) and cadmium telluride (CdTe) are in widespread use. These devices exhibit very high efficiency.[3] However, the cost of inorganic photovoltaic cells are generally too high.[3] In this scenario, photovoltaic cells based on organic molecules have emerged as alternatives with the advantages of being low-cost, transparent, and flexible. This is the reason behind the phenomenal growth in the research in organic photovoltaic or solar cells (OSC) in the last few decades. Tang reported the first successful device in 1986 which showed a power conversion efficiency (PCE) of $\sim$1%.[4] In 1995, Heeger and co-workers reported the first bulk-heterojunction (BHJ) architecture based OSC with the conjugated polymer poly(2-methoxy-5-(2′-ethyl-hexyloxy)-1,4-phenylenevinylene) as a donor and a fullerene (C_{60}) as an

acceptor in the active layer.[5, 6] Following this work, a lot of work has been carried out in the last two decades to improve the performance of a device by modifying the active layer. Presence of organic compounds in the active layer paves ways for easy modifications, and this has been shown to greatly affect the PCE. In recent times, PCEs of BHJ based OSCs have reached $\sim$ 15-18%.[7–10]

As mentioned in the previous paragraph, designing the active layer is a key component of device fabrication. Small changes in the structures of conjugated oligomers or small molecules lead to significant changes in the overall properties. In this thesis, we report on the design of conjugated oligomers and small molecules based on benzodithiophene and show the effect of various modifications such as backbone and side chain modulations on the properties. Below we provide a quick overview of the device architecture, the working principle, characterization of a solar cell, and an outline of the thesis work.

1.1 Organic solar cell device architecture

In this section, a brief outline of the three most used OSC architectures is presented. Typically, organic solar cells consist of three layers, an active layer, an anode and a cathode, with the active layer in the middle. While indium tin oxide is usually used as a transparent anode, metal electrodes such as aluminium, magnesium or calcium are used as cathode. The most important part in the device is the morphology of the active layer. Below, we discuss three different active layer architectures: (i) Single-layer OSC, (ii) Bilayer OSC and (iii) BHJ OSC.

1.1.1 Single-layer devices

Single-layer cells have a simple architecture of a single layer of photoactive material sandwiched between the two electrodes (a typical structure is shown in Fig.1.1). In these devices, the absorption is usually small. In addition, poor charge mobility

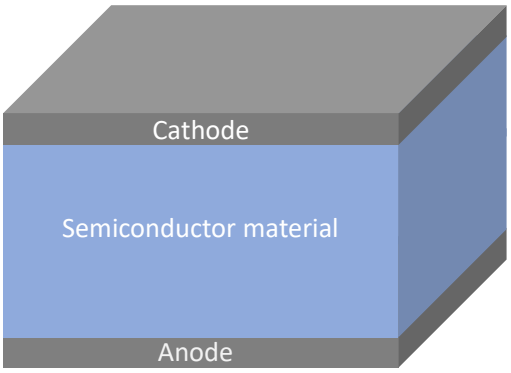

FIGURE 1.1: A single layer device configuration.

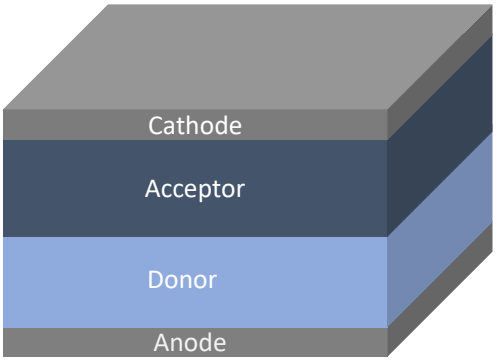

FIGURE 1.2: A bilayer heterojunction based device configuration.

in the organic layer, low interfacial area and large recombination losses result in poor efficiencies.

1.1.2 Bilayer devices

As the name suggests, the active layer in a bilayer cell consists of two layers, a donor (D) layer and an acceptor (A) layer, sandwiched between the two electrodes. A typical bilayer device architecture is shown in Fig.1.2. The bilayer OSCs have shown better performance than the single-layer devices. Separation of the active layer into D and A layers ensures contact with the correct electrode. In addition, charge recombination is reduced. However, the small interfacial area leading to recombination and small exciton diffusion length result in low efficiencies.

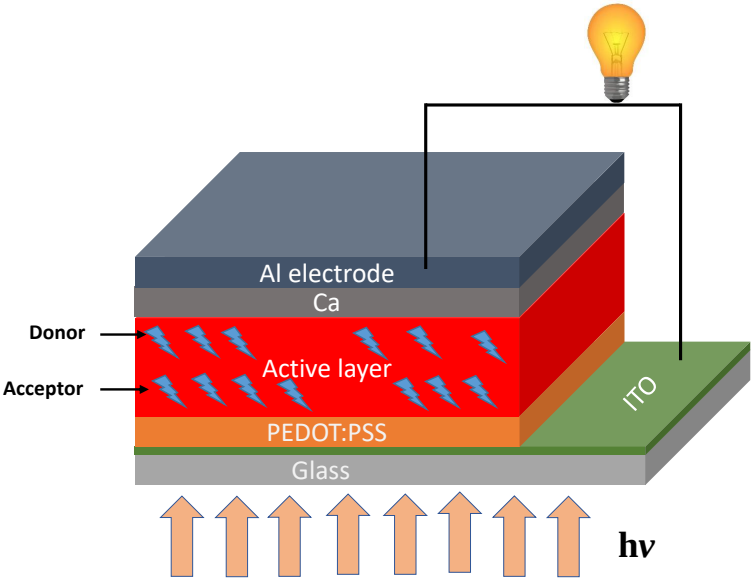

FIGURE 1.3: A bulk heterojunction architecture based device configuration.

1.1.3 Bulk heterojunction (BHJ) device

A smart way to overcome the difficulties associated with a bilayer device is to design an active layer in which the donor and the acceptor layers are intimately blended with each other. This is called a BHJ architecture, proposed by Alan Heeger in 1995.[5] A typical BHJ device configuration is shown in Fig.1.3. BHJ is the current state of art device architecture, and a lot of research is carried out to further improve the efficiencies of devices based on BHJ. A molecular blend of donors and acceptors results in a much larger interfacial area and this reduces the exciton loss. In addition, larger diffusion length allows the excitons to easily get separated into free charges.

1.2 Working principle of OSCs

In OSC devices, the photovoltaic process of converting light into electricity can be explained in following four steps:

(i) Light absorption

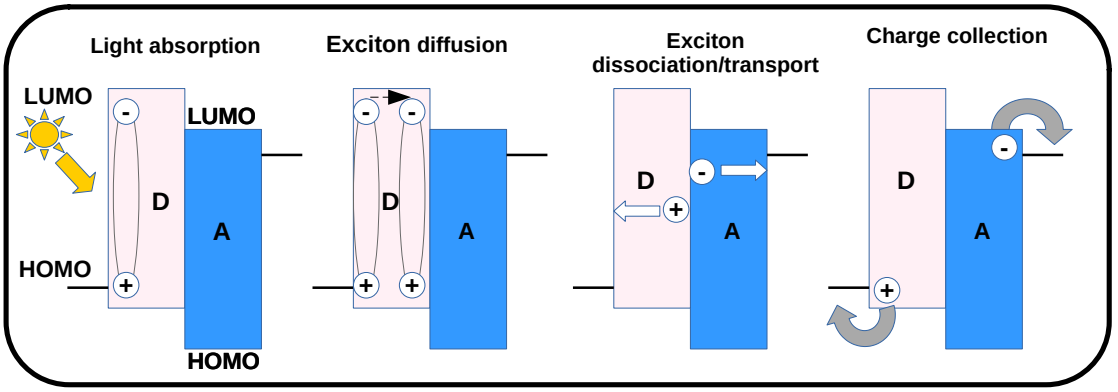

FIGURE 1.4: Working principle of organic solar cell.

(ii) Exciton diffusion

(iii) Exciton dissociation

(iv) Charge transport and collection

These steps are shown in Fig. 1.4.

1.2.1 Light absorption

The first step in the photovoltaic process is the absorption of light by the photoactive material. Absorption of light results in exciting the electron from the highest occupied molecular orbital (HOMO) to the lowest unoccupied molecular orbital (LUMO) level, leaving a hole in the HOMO. This bound electron-hole pair, termed as an exciton, is localized (*Frenkel exciton*) and tightly bound. Typically, organic polymers or small molecules are used as donor materials. Due to their low dielectric constants the binding energy of the exciton is larger than the thermal energy at room temperature.

1.2.2 Exciton diffusion

The lifetime of photo-generated excitons is a few picoseconds. Within its lifetime, the excitons migrate through the organic layer to the D/A interface. This exciton diffusion is usually described in terms of thermally activated hopping.

1.2.3 Exciton dissociation

Once the exciton reaches the D/A interface, it can get dissociated into separated charges via electron or hole transfers. Following conditions should be met for the dissociation to happen: i. the LUMO/LUMO energy level difference between the donor and acceptor must be large enough to ensure an efficient electron transfer, and ii. the orbital overlap between the D and A molecules at the interface should be large enough. The meta-stable state resulting after charge transfer is called a charge transfer state. The dissociated charges are still bound by Coulombic attractions, and this energy needs to be overcome to create separated charges. The rate of charge transfer is usually described by the classical Marcus theory which will be discussed in the Chapter 2.

1.2.4 Charge transport and collection

Once the separated charges are created, those are moved towards the appropriate electrodes. The charge carriers are then collected at the electrodes, and are used in the circuit to produce current.

1.3 Characterization of organic solar cells

The performance of an organic solar is measured in terms of PCE. It is defined as the ratio of usable electric power produced from the incoming power. PCE can be calculated using the following equation:

$$\text{PCE} = \frac{J_{\text{sc}} \times V_{\text{oc}} \times FF}{P_{\text{in}}}, \tag{1.1}$$

where V_{oc} is the open-circuit voltage, J_{sc} is the short-circuit current density, FF is the fill factor and P_{in} is the power density of the incident light.

1.3.1 Open circuit voltage

V_{oc} is defined as the maximum voltage transferred by the solar cell when the current is zero. In case of BHJs, charge separation occurs efficiently at the interface, and hence, V_{oc} depends strongly on the gap between the energy of HOMO of donor and the energy of LUMO of the acceptor. In 2006, Scharber et al.[11] studied a series of different polymer donors with a common acceptor, and proposed an empirical relationship to express V_{oc} as

$$V_{oc} = \frac{1}{e}(|E^{D}_{HOMO}| - |E^{A}_{LUMO}|) - 0.3 \text{ V}, \tag{1.2}$$

where e is the elementary charge, and 0.3 V is an empirical factor. E^{D}_{HOMO} and E^{A}_{LUMO} are the HOMO and LUMO levels of the donor and the acceptor, respectively.

1.3.2 Short-circuit current density

J_{sc} is the maximum current that is generated when the voltage is zero. J_{sc} is calculated as[12]

$$J_{sc} = e \int \text{EQE}(\lambda) \times N(\lambda)\, d\lambda, \tag{1.3}$$

where EQE is the external quantum efficiency. EQE determines an absorbed photon's conversion efficiency into current. $N(\lambda)$ is the number of photons given by the solar spectrum over all frequencies. Hence, absorption ability and band gap of the donor affect the J_{sc}. In addition, it also depends on the exciton diffusion length and carrier mobilities.

1.3.3 Fill factor

FF is one of the key parameters that determine the PCE of the organic-photovoltaic device. It is defined as the ratio between the maximum power (denoted as P_{max}

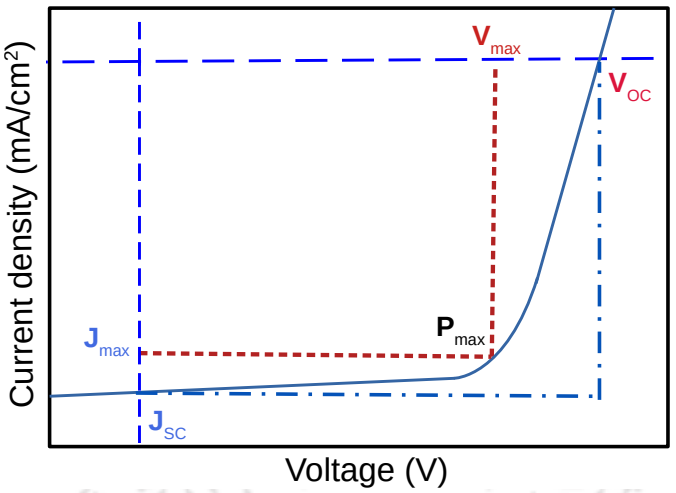

FIGURE 1.5: Current-voltage diagram for an OSC device. J_{sc}, the current at which the voltage is zero, and V_{oc}, the voltage when the current is zero, are shown as vertical and horizontal dashed blue lines, respectively. J_{max} and V_{max} are the current and voltage at the P_{max}, the maximum power point.

in the Fig. 1.5) delivered to an external circuit and the product of V_{oc} and J_{sc} as [13]

$$FF = \frac{J_{max}V_{max}}{J_{sc}V_{oc}}, \tag{1.4}$$

where J_{max} and V_{max} are the current density and voltage, respectively, at the P_{max} point. The above four quantities are shown in Fig. 1.5. As shown in the figure, FF is the ratio of rectangle *1* made with J_{max} and V_{max} from the origin to the rectangle *2* made with J_{sc} and V_{oc} from the origin. In the ideal case, the FF is 100%. In reality, it is 50-70% for the organic solar cells. So, there is a large amount of efficiency fall due to the resistance called parasitic resistance. There are two types of parasitic resistances: shunt (R_{sh}) and series resistances (R_s). R_s affects the applied voltage. If R_s is high, then the voltage drops less on the diode, and the current increases slower with voltage. In addition to these resistances, FF is also affected by charge carrier recombination and carrier lifetime.

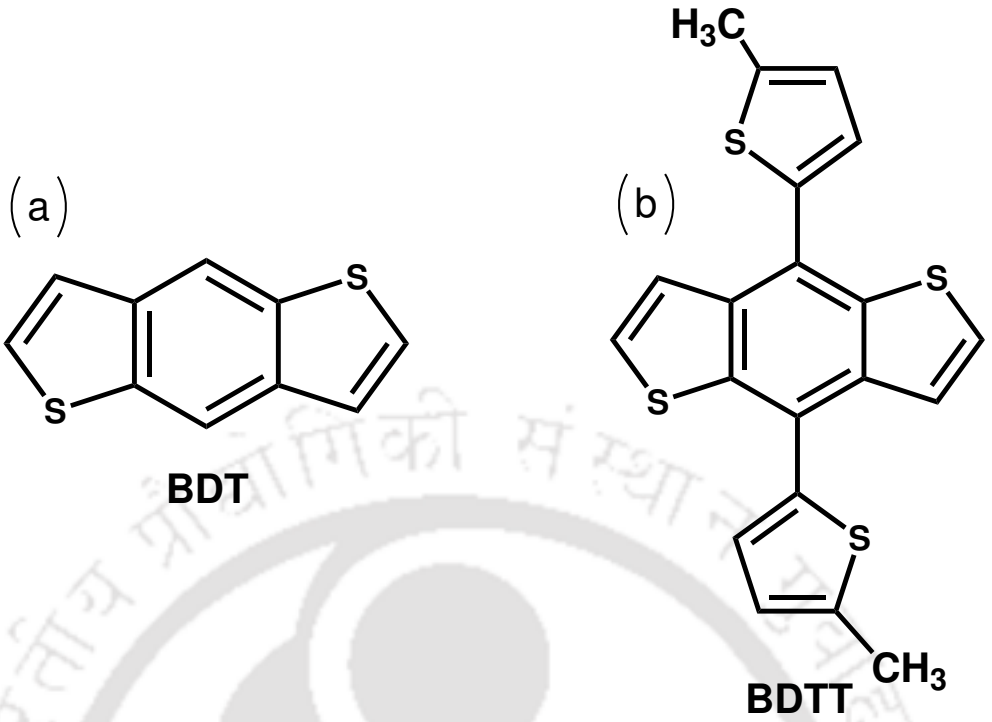

FIGURE 1.6: (a) Molecular structure of BDT unit and (b) BDTT unit.

1.4 Motivation

Bulk heterojunction architecture based OSCs are promoted rapidly in recent times due to various advantages such as wide-area of materials selection, simple preparation procedure, light-weightness, low-cost, transparency and mechanical flexibility.[14–16] In recent times, PCEs of 15-18% have been achieved.[7–10, 17, 18] A typical BHJ structure comprises of an intimate blend of a polymer/small-molecule as donor and a fullerene or a non-fullerene (NF) as acceptor. The improvements in the PCEs are attributed to advanced designing of D-A based polymers (or small-molecules), and in recent times, to the development of NF acceptors.[7–10, 17–25] Having a D-A structure helps in tuning the energy levels and band gaps.[7–10, 14, 17–30] Hence, an understanding of the optoelectronic properties of donor and acceptor molecules is vital to building a better active layer. Here, computational studies play an important role in understanding the structure property relationships of conjugated polymers, small molecules and NF acceptors.

Recently, the interest in benzo[1,2-b:4,5-b′]dithiophene (BDT) (shown in Fig. 1.6(a)) based conjugated polymers, and small molecules has increased considerably.[14, 22, 31, 32] BDT has a rigid planar structure and shows good π-π stacking property. Various modifications of the parent BDT unit has also been carried out to improve its capability as a donor polymer.[14] For example, various heterocyclic units such as furan, thiophene, and thienothiophene have been introduced laterally at 4 and 8 positions of the BDT units. This results in a type of two-dimensional building blocks, and this has been shown to affect the optoelectronic and charge transport properties of the conjugated polymers and small molecules.[33–35] The BDT unit with conjugated alkylthienyl side chains results in 4,8-bis(5-methylthiophen-2-yl)benzo[1,2-b:4,5-b′]dithiophene, (denoted as BDTT in this thesis and shown in Fig.1.6(b)) also has been extensively used. The presence of lateral thiophene units opens up various possibilities of modifications. For example, substitutions by electron-withdrawing or electron-donating groups in side chains result in modifying the molecular geometry, and thereby affecting the performance. Even effects of substitutions in the main chain of BDTT has also been studied.[36–40]

One promising strategy to develop suitable organic materials is by introducing halogen atoms at different positions in the oligomers' side chain. Introduction of the fluorine, chlorine, and bromine atoms in the side chain of a conjugated polymer and small molecule have been shown to improve the PCE of OSCs.[41–44] Another strategy for improving the efficiency of OSCs is the insertion of a π bridge between the donor and acceptor units. A lot of studies in the literature show that introduction of π bridges such as furan, thiophene and thiazole greatly affect the optoelectronic properties. To conclude, BDT based donors have been extensively used, and in this thesis, we aim to contribute towards understanding the effects of substitutions in the donor unit by carrying out various types of structural changes in BDTT.

1.5 Outline of the thesis

In this thesis, we present the results of computational studies on donor-acceptor based small molecules and oligomers. Effects of modification of these donors on the charge transfer and recombination properties when blended with either fullerene or non-fullerene acceptors are also presented. All the studies are carried out at DFT and TD-DFT levels. In chapter 2, theoretical and computational methods are briefly discussed. In chapter 3, the effect of fluorination of the donor unit on the properties of benzodithiophene-triazole based donor-acceptor systems is explored. Fluorine substituted systems are found to have higher V_{oc}, and faster charge mobilities compared to the parent molecules. The ground state geometries, optoelectronic, and charge transfer properties of halogenated thienothiophene benzodithiophene-based small molecules are presented in the chapter 4. The results indicate better rates of charger-transfer in halogenated systems showing that halogentation is an effective way to tune the properties. Chapter 5 focuses on effect of π bridges on the optoelectronic and charge transfer properties in blends of alternating donor-π-acceptor type oligomers with fullerene acceptor. This is followed by the chapter 6 which explores the effect of π linkers on properties of random oligomers, and their blends with non-fullerene acceptor. The overall conclusions of my thesis work are presented in chapter 7. Our studies reveal that electronic, optical, and charge transfer properties can be tuned effectively by introducing halogen atoms and π-linkers in the main and side chains of the donor oligomers.

Chapter 2

Theoretical and computational methods

2.1 Molecular Schrödinger equation

In quantum chemistry, the main task is to solve the time-independent molecular Schrödinger equation (SE) which contains information about the stationary states of a system. The Schrödinger equation for a system of N electrons and M nuclei is written as

$$\hat{H}\Psi_i(x_1, x_2....x_N, R_1, R_2....R_M) = E_i\Psi_i(x_1, x_2....x_N, R_1, R_2....R_M), \quad (2.1)$$

where $\hat{H}$ is the Hamiltonian operator representing the total energy of the system. Ψ is the wave function of i-th state of the system, and E_i is the corresponding energy. In Eq. 2.1, x_i denotes $3N$ spatial, N spin coordinates of electrons, and R_i denotes the $3N$ spatial coordinates of the nuclei. In atomic units, the Hamiltonian operator for a system of N electrons and M nuclei is written as[45]

$$\hat{H} = -\sum_{i=1}^{N}\frac{1}{2}\nabla_i^2 - \sum_{A=1}^{M}\frac{1}{2M_A}\nabla_A^2 - \sum_{i=1}^{N}\sum_{A=1}^{M}\frac{Z_A}{r_{iA}} + \sum_{i=1}^{N}\sum_{j>i}^{N}\frac{1}{r_{ij}} + \sum_{A=1}^{M}\sum_{B>A}^{M}\frac{Z_AZ_B}{R_{AB}}. \quad (2.2)$$

Here, M_A is the mass of nucleus A, Z_A and Z_B are the atomic numbers of nuclei A and B, respectively. R_{AB}, r_{iA} and r_{ij} are the distances between the nuclei A and B, electron i and nucleus A, and the two electrons i and j, respectively. First two terms are the operators for kinetic energies of electrons and nuclei, respectively. The last three terms are the potential energy operators for the electron-nucleus

attraction, the electron-electron repulsion, and the nucleus-nucleus repulsion, respectively.

2.2 Born-Oppenheimer approximation

The Born-Oppenheimer approximation is very important while solving the Schrödinger equation. It is based on the fact that electrons are much lighter than nuclei, and thus react much faster to molecular potential changes. Hence, the wave function can be approximated as a product of nuclear and electronic wave functions. As a result, the kinetic energy of the nuclei can be neglected, and the nucleus-nucleus repulsion term can be made constant. This results in the electronic Hamiltonian operator for N electrons and M nuclei written as

$$\hat{H}_{\text{elec}} = -\sum_{i=1}^{N} \frac{1}{2}\nabla_i^2 - \sum_{i=1}^{N}\sum_{A=1}^{M} \frac{Z_A}{r_{iA}} + \sum_{i=1}^{N}\sum_{j>i}^{N} \frac{1}{r_{ij}}, \tag{2.3}$$

and the electronic wave function as,

$$\Psi_{\text{elec}} = \Psi_{\text{elec}}(r_{i;}R_A). \tag{2.4}$$

Here, Ψ_{elec} is dependent on electronic coordinate, but parametrically on the nuclear coordinate. The corresponding Schrödinger equation is

$$\hat{H}_{\text{elec}}\Psi_{\text{elec}} = E_{\text{elec}}\Psi_{\text{elec}}, \tag{2.5}$$

where E_{elec} is the corresponding electronic energy. The total energy of a system is

$$E = E_{\text{elec}} + \sum_{A=1}^{M}\sum_{B>A}^{M} \frac{Z_A Z_B}{R_{AB}}. \tag{2.6}$$

2.3 Mean-field approximation and Hartree-Fock method

Considering that the N-electron SE is not analytically solvable, the mean-field theory is used to transform the many body problem into a set of coupled one-electron problems. Using the mean-field theory, an N-electron wave function of the form $\Psi(r_1, r_2...r_N)$ is then written as a product of one-electron orbitals as

$$\Psi(r_1, r_2...r_N) = \Phi_1(r_1)\Phi_2(r_2)...\Phi_n(r_N). \tag{2.7}$$

$\Phi_1(r_1)$ can be expressed as $\Phi_1(1)\sigma_1(1)$, where σ is the spin wave function which depends on the spin orientation of the electron. For a fermionic system like the N-electron system, the Ψ_{elec} is expressed by an antisymmetrized product of one-electron wave functions, a Slater determinant,

$$\Psi(r_1, r_2, ...r_N) = \frac{1}{\sqrt{N!}} \begin{vmatrix} \Phi_1(1)\alpha(1) & \Phi_1(1)\beta(1) & \dots & \Phi_M(1)\beta(1) \\ \Phi_1(2)\alpha(2) & \Phi_2(2)\beta(2) & \dots & \Phi_M(2)\beta(2) \\ \vdots & \vdots & \vdots & \\ \Phi_1(N)\alpha(N) & \Phi_N(N)\beta(N) & \dots & \Phi_M(N)\beta(N) \end{vmatrix}, \tag{2.8}$$

where M equals to $N/2$ and $(N+1)/2$ for even and odd N, respectively.

A single Slater determinant is used as an approximation to the electronic wave function in the Hartree-Fock (HF) theory. Here each electron corresponding to $\Phi_i(r)$ satisfies the following equation,

$$\Big(-\frac{1}{2}\Delta_i^2 - \sum_{A=1}^{M} \frac{Z_A}{r_{iA}} + v^{HF}(i) \Big) \Phi_i(r) = \varepsilon_i \Phi_i(r) \tag{2.9}$$

where $i = 1, 2....,N$. $v^{HF}(i)$ is the average potential experienced by the ith electron in the presence of the other electrons. The resulting set of equations is referred to as the HF equations, and the iterative self-consistent field procedure is used to solve those.

In the HF method, electron-electron correlation effects are not considered. The electron-electron correlation effects can be introduced by various post-HF methods such as configuration interaction, Möller-Plesset perturbation theory,[46] algebraic diagrammatic construction method, [47, 48] coupled-cluster based methods such as second-order coupled-cluster (CC2)[49] and multi-configurational methods such as the complete active space self-consistent field (CASSCF) methods.[50, 51] However, these methods are not suitable for studying macromolecules like conjugated polymers because of prohibitive computational costs. Therefore, instead of using ab initio correlated wave function-theory methods, DFT and TD-DFT based methods providing a good balance between accuracy and computational cost are generally used to obtain the structures and properties of conjugated oligomers and small molecules which are used in the active layers of OPVs.

2.4 Density functional theory

DFT is one of the most widely used methods to describe the electronic structure of atoms, molecules, crystals, and surfaces. Electron probability density function, denoted as $\rho(x, y, z)$ is extracted from the wave function. It is a function only three variable (x, y, z), but N-electron wave function depends on $4N$ variable. The single-particle probability density corresponding to a normalized ground-state N-electron wave function is given by,

$$\rho(r) = N \int |\Psi(r, r_2 ...., r_N)|^2 d^3 r_2, ..., d^3 r_N. \tag{2.10}$$

The energy of the system based on the three-dimensional electron density is

$$E = \int E(\rho)\rho(r)dr, \tag{2.11}$$

where $E(\rho)$ is the total energy functional.

The Hohenberg-Kohn theorems provide the basis for DFT.[52] The first Hohenberg-Kohn theorem says that the ground-state electron density function can determine all the properties of a molecule in a ground electronic state. The second Hohenberg-Kohn variation theorem states that energy obtained using a trial density functional is always higher than the true ground state energy.

The Hohenberg-Kohn theory is valid for both interacting and non-interacting electrons. The non-interacting part can be treated easily which constitutes a large portion of the electronic energy, and relatively small portion is associated with the interacting part which can be calculated by a density functional.

The energy of a system can be written as a functional of density

$$E[\rho] = T[\rho] + J[\rho] + v_{ext}[\rho](r) + E_{XC}[\rho], \tag{2.12}$$

where $T[\rho]$ is the kinetic energy, $J[\rho]$ is the Coulomb energy describing electron repulsion, and $v_{ext}[\rho]$ is the external potential. The $E_{XC}[\rho]$ term, a functional of the electron density function related with two terms, originating from the difference of the real and imaginary non-interacting systems are given by

$$E_{XC}[\rho] = \Delta\langle T[\rho]\rangle + \Delta\langle V_{ee}[\rho]\rangle. \tag{2.13}$$

Here, $\Delta\langle T\rangle$ represents the correlation to the kinetic energy deriving from electrons' interacting nature. $\Delta\langle V_{ee}\rangle$ term represents the non-classical corrections to the electron-electron repulsion energy. $T[\rho]$ in terms of the Kohn-Sham orbitals (KS), ψ_i^{KS}, can be defined as

$$T[\rho] = -\frac{1}{2}\sum_{i=1}^{N}\langle\psi_i^{KS}|\nabla_i^2|\psi_i^{KS}\rangle. \tag{2.14}$$

The orbitals ψ_i^{KS} used in equation 2.14 to minimize the energy E are obtained by solving the KS equations,

$$\hat{h}_i^{KS}\psi_i^{KS} = \varepsilon_i^{KS}\psi_i^{KS}, \tag{2.15}$$

where $\hat{h}_i^{KS}$ is the KS one-electron operator and it is defined as

$$\hat{h}_i^{KS} = -\frac{1}{2}\nabla_i^2 - \sum_A^{nuclei} \frac{Z_A}{r_{1A}} + \int \frac{\rho(r_2)}{r_{12}} dr_2 + V_{XC}. \tag{2.16}$$

The exchange correlation potential V_{XC} is a functional derivative of E_{XC} as shown below:

$$V_{XC} = \frac{\delta E_{XC}[\rho(r)]}{\delta \rho(r)}. \tag{2.17}$$

2.5 Approximate exchange-correlation functionals

The exact functionals for the exchange and correlation are unknown, and therefore, various approximations are used to calculate the E_{XC}. Exchange-correlation functionals can be defined by a Jacob's ladder. The different approximations are the local density approximation (LDA), local generalized gradient approximation (GGA), meta-GGA, hybrid, and double-hybrid functional approximations. In the LDA, $E_{XC}(\rho)$ is calculated as a function of the local density only at a given position. The LDA is exact for a homogeneous electron gas and hence, it works well for systems in which the density does not vary too much. When spin is included in the LDA, it results in the local spin-density approximation (LSDA) functional. In the GGA functionals, the density gradient which is the first derivative of the density at the given position is also included. In a *meta*-GGA functional, in addition to the spin densities and their gradients, Laplacians of the spin density are also included. Hybrid functionals are constructed by mixing a fraction of exchange energy functional to the LDA/LSDA or GGA functionals. A hybrid functional can be written as,

$$E_{\mathrm{XC}}^{\mathrm{hybrid}} = aE_{\mathrm{X}}^{\mathrm{exact}} + (1-a)E_{\mathrm{X}}^{\mathrm{DFT}} + E_{\mathrm{C}}^{\mathrm{DFT}}, \tag{2.18}$$

where a is the mixing parameter, $E_{\mathrm{X}}^{\mathrm{exact}}$ is the nonlocal HF exchange energy, $E_{\mathrm{X}}^{\mathrm{DFT}}$ is the local DFT exchange energy, and $E_{\mathrm{C}}^{\mathrm{DFT}}$ is the local DFT correlation energy. For example, the Becke's three-parameter Lee-Yang-Parr (B3LYP) exchange-correlation hybrid functional,[53] can be expressed as

$$E_{\mathrm{XC}}^{\mathrm{B3LYP}} = a_0 E_{\mathrm{X}}^{\mathrm{exact}} + (1-a_0)E_{\mathrm{X}}^{\mathrm{LSDA}} + a_{\mathrm{b}}E_{\mathrm{X}}^{\mathrm{B88}} + a_{\mathrm{c}}E_{\mathrm{c}}^{\mathrm{LYP}} + (1-a_{\mathrm{c}})E_{\mathrm{c}}^{\mathrm{LSDA}}, \quad (2.19)$$

where $E_{\mathrm{X}}^{\mathrm{B88}}$ is the gradient corrected exchange energy obtained from the Becke functional[54], and $E_{\mathrm{c}}^{\mathrm{LYP}}$ is the correlation energy according to the Lee-Yang-Parr functional.[55] The three parameters a_0, a_{b} and a_{c} are optimized to 0.20, 0.72 and 0.81, respectively. There are many other hybrid functionals reported in the literature such as PBE0[56], HSE[57] and O3LYP.[58]

In recent times, range-separated hybrid (RSH) functionals are used in many places, particularly to describe extended π-conjugated systems and charge transfer excitations. The basic idea is to split the electron-electron interaction $(1/r_{12})$ into short-range and long-range parts using the standard error function. In consequence, the correct asymptotic $r_{12} \to \infty$ behavior is retained, where the Coulomb and exchange potentials cancel each other. The equation is written as

$$\frac{1}{r_{12}} = \frac{1-\mathrm{erf}(\mu r_{12})}{r_{12}} + \frac{\mathrm{erf}(\mu r_{12})}{r_{12}}, \quad (2.20)$$

where μ is a range separating parameter. For the exchange energy term, the short-range and long-range terms are treated by the DFT and the exact HF exchange, respectively.

There are various RSH functionals available in the literature, e.g., ωB97XD[59, 60], *lc*-ωPBE[61] and *lc*-BLYP[62] etc. Yanai et al.[63] have proposed a generalized version of Eq. 2.20 by introducing two extra parameters (α and β) in the equation as,

$$\frac{1}{r_{12}} = \frac{1-[\alpha+\beta\ .\ \mathrm{erf}(\mu r_{12})]}{r_{12}} + \frac{\alpha+\beta\ .\ \mathrm{erf}(\mu r_{12})}{r_{12}}, \quad (2.21)$$

where the relations $0 \leq \alpha + \beta \leq 1$, $0 \leq \alpha \leq 1$, and $0 \leq \beta \leq 1$ are satisfied. The parameters α and β incorporate the HF-exchange part over the whole range by a factor of α and the DFT part over the whole range by a factor of 1-(α+β), respectively. This Coulomb-attenuating method (CAM) with three parameters is more flexible than the LR-method. The standard parameters α, β, and μ values are 0.19, 0.46, and 0.33, respectively, for CAM-B3LYP.[63]

DFT has been the method of choice to describe organic donors, acceptors and donor-acceptor blend systems in the literature. Excellent compromise between accuracy and computational efficiency has enabled the DFT methods to treat very large systems containing hundreds of atoms. In the thesis work, I have used DFT based methods for the studies.

2.6 London dispersion corrections

Dispersion interactions can be defined as the attractive part of the van der Waals interaction potential between atoms and molecules that are not directly bonded to each other.[64, 65] Initially, this was noted for rare-gas dimers but later was also noticed in base pair stacking systems. Conventional DFT functionals that do not contain the physics of dispersion interactions often fail in cases where the dispersion interaction plays an important role in determining systems' geometries and thermodynamic properties. Out of various methods developed to incorporate the dispersion interaction, Grimme's DFT-D[66] methods are well-established for dispersion interaction, but the DFT-D3[67] method is the most successful. In DFT-D3, dispersion corrections term includes sixth and eighth-order terms with improving dispersion coefficients and damping function. The total DFT-D3 energy of a system is written as

$$E_{\mathrm{DFT-D3}} = E_{\mathrm{DFT}} + E_{\mathrm{disp}}, \tag{2.22}$$

where E_{DFT} is the energy obtained by the original DFT functional and E_{disp} is the dispersion correction. E_{disp} is the addition of two- and three-body energies

written as

$$E_{\text{disp}} = E^{(2)} + E^{(3)}. \tag{2.23}$$

Out of these two, the $E^{(2)}$ is the most important term.[64] This term with the standard zero damping formula is given as

$$E^{(2)} = -\sum_{n=6,8} s_n \sum_{i,j} \frac{C_n^{ij}}{r_{ij}^n} f_{d,n}(r_{ij}). \tag{2.24}$$

Here, the first sum is over all atom pairs in the system. C_n^{ij} represents the average nth order dispersion coefficients for atom pair ij, r_{ij} is their internuclear distance, and $f_{d,n}(r_{ij})$ is the damping function. $f_{d,n}$ is expressed as

$$f_{d,n}(r_{ij}) = \frac{1}{1 + 6(r_{ij}/(s_{r,n} r_0^{ij}))^{-\alpha_n}}, \tag{2.25}$$

where parameter $s_{r,n}$ is the order-dependent scaling factor of the cutoff radii r_0^{ij}. The "steepness" parameters α_n are not fitted but adjusted such that the dispersion correction is $< 1\%$ of max ($|E_{\text{disp}}|$) for typical covalent bond distances. From Eq. 2.24, the term $E^{(2)}$ with the Becke-Johnson (BJ) damping function is expressed as[68]

$$E_{\text{disp}}^{\text{D3BJ}} = -\sum_{n=6,8} s_n \sum_{i,j} \frac{C_n^{ij}}{(r_{ij})^n + f_{d,n}(r_{ij})^n}, \tag{2.26}$$

where the $f_{d,n}$ function is

$$f_{d,n} = a_1 \sqrt{\frac{C_8^{ij}}{C_6^{ij}}} + a_2. \tag{2.27}$$

Here, parameters $s_{r,n}$, a_1 and a_2 are fitted for each DFT functional. The three-body term $E^{(3)}$ is defined as

$$E^{(3)} = \sum_{\text{ABC}} f_{d,(3)}(\overline{r}_{\text{ABC}}) E^{\text{ABC}}, \tag{2.28}$$

where the sum of is over all atom triples in the molecule. The damping function $f_{d,(3)}$ is defined as

$$f_{d,3}((\overline{r}_{\mathrm{ABC}}) = \frac{1}{1+6(\overline{r}_{\mathrm{ABC}}/(4r_0^{\mathrm{ABC}}/3))^{-16}}. \tag{2.29}$$

Here, $\overline{r}_{\mathrm{ABC}}$ is the geometrically averaged radii. The term E^{ABC} is expressed as

$$E^{\mathrm{ABC}} = \frac{C_9^{\mathrm{ABC}}(3\ \cos\ \theta_{\mathrm{a}}\ \cos\ \theta_{\mathrm{b}}\ \cos\ \theta_{\mathrm{c}}+1)}{(r_{\mathrm{AB}}r_{\mathrm{BC}}r_{\mathrm{CA}})^3}, \tag{2.30}$$

where θ_a, θ_b, and θ_c are the internal angles of the triangle formed by r_{AB}, r_{BC}, and r_{CA}. C_9^{ABC} is the triple-dipole moment constant and is expressed as

$$C_9^{\mathrm{ABC}} = \frac{3}{\pi}\int_0^{\infty} \alpha^A(i\omega)\alpha^B(i\omega)\alpha^C(i\omega)d\omega. \tag{2.31}$$

As the total three-body contribution is very small, C_9^{ABC} is expressed as

$$C_9^{\mathrm{ABC}} \approx -\sqrt{C_6^{\mathrm{AB}}C_6^{\mathrm{AC}}C_6^{\mathrm{BC}}}. \tag{2.32}$$

In the thesis, we have used DFT-D3 version for donor-acceptor blend calculations.

2.7 Time-dependent density functional theory

TDDFT is a density-based formally exact approach and is used widely for investigating excited-state properties and optical spectra.[69, 70] Like the Hohenberg-Kohn theorem for DFT, the Runge-Gross theorem[71] is the basis for TDDFT. It states that there is a one-to-one mapping between the time-dependent external potential $v(r,t)$ and the time-dependent density of the system. In addition, the von Leeuwen theorem[72] is used in a fashion similar to the KS formalism for the ground state, and this is stated as follows: Let us say that there are two many-body systems with different particle-particle interactions, $\omega(r-r')$ and $\omega'(r-r')$. If an external potential $v(r,t)$ produces a time-dependent density $\rho(r,t)$ is system 1, then a unique potential $v'(r,t)$ can be constructed that produces the same

density in system 2. In scenarios where the perturbation is small and the system does not change much from the initial state, it is sufficient to use the first order in perturbation. This is known as linear response formalism. Below we discuss linear response formalism briefly.

Let us suppose that at $t < t_0$, the time-dependent potential is zero. At time t_0, a time-dependent potential, v_1 ($\mathbf{r}$, t) is turned on which results in a change in the density written as

$$\rho(\mathbf{r},t) = \rho_0(\mathbf{r}) + \rho_1(\mathbf{r},t) + \rho_2(\mathbf{r},t) + \rho_3(\mathbf{r},t) + ...^M \tag{2.33}$$

Here, ρ_0 is the ground state density, $\rho_1(\mathbf{r},t)$ the first-order response and $\rho_2(\mathbf{r},t)$ second-order response etc. The linear response term can be written as

$$\rho_1(\mathbf{r},t) = \int dt_1 \int d^3r_1 \chi(\mathbf{r},t,\mathbf{r}_1,t_1) v_1(\mathbf{r}_1,t_1), \tag{2.34}$$

where χ represents the linear density-density response function of the system. The linear response of an interacting system can be calculated as the response of non-interacting KS system as

$$\rho_1(\mathbf{r},t) = \int dt_1 \int d^3r_1 \chi_s(\mathbf{r},t,\mathbf{r}_1,t_1) v_{s1}(\mathbf{r}_1,t_1), \tag{2.35}$$

where χ_s term is the density-density response function for the noninteracting KS electrons. The symbol $v_{s1}(\mathbf{r},t)$ is the linear change of the effective potential, $v_s(\mathbf{r},t)$, of the time-dependent KS system, and it can be written as

$$v_{s1}[\rho](\mathbf{r},t) = v_1(\mathbf{r},t) + \int d^3r_1 \frac{\rho(\mathbf{r}_1,t)}{|\mathbf{r}-\mathbf{r}_1|} + \int dt_1 \int d^3r_1 \frac{\delta v_{XC}[\rho](\mathbf{r},t)}{\delta\rho(\mathbf{r}_1,t_1)} \rho_1(\mathbf{r}_1,t_1) \tag{2.36}$$

where $v_1(\mathbf{r},t)$ is the external potential and second term is the linearized time-dependent Hartree potential. The functional derivative of the XC potential with respect to the density is known as the exchange kernel and is evaluated at the ground state density.

By using equations 2.36, 2.35 and 2.34, we obtain the Dyson equation of TDDFT as

$$\chi(\mathbf{r},t,\mathbf{r}_1,t_1) = \chi_s(\mathbf{r},t,\mathbf{r}_1,t_1) + \int d\tau \int d^3x \int d\tau_1 \int d^3x_1 \chi_s(\mathbf{r},t,\mathbf{x},\tau) \left\{\frac{\delta(\tau-\tau_1)}{|\mathbf{x}-\mathbf{x}_1|} + f_{XC}(\mathbf{x},\tau,\mathbf{x}_1,\tau_1)\right\}\chi(\mathbf{x}_1,t_1,\mathbf{r}_1,t_1). \tag{2.37}$$

This equation is useful to calculate the properties of many-body systems under small perturbation. One of the other linear-response approaches that is widely used is the Casida formalism.[73]

2.8 Marcus theory

The Marcus theory[74] is a semi-classical theory to describe the charge transfer processes, and has been extensively used to calculate charge transfer rates in OSCs. It describes the charge transfer between two weakly coupled sites. Below we provide a quick derivation as shown in Refs.[75–79] In the limit of weak coupling, the interaction between two sites can be treated as a small perturbation, and hence Fermi's Golden rule which treats charge transfer as a radiation less transition is applicable in this regime. Fermi's Golden rule is derived from time-dependent perturbation theory and states that non-adiabatic charge (electron) transfer rate ($k_{i,j}$) between two sites i and j is given as

$$k_{i,j} = \frac{2\pi}{\hbar}|V_{\mathrm{ij}}|^2\ \rho(E_f). \tag{2.38}$$

Here, V_{ij} is the coupling integral (or electronic coupling) defined as $\langle\psi_i|\hat{V}|\psi_j\rangle$. ρ is the density of states representing the thermal distribution of final electronic states. The Eq. 2.38 includes sum over all the probability densities. Within the Franck-Condon approximation, the above equation can be rewritten as

$$k_{i,j} = \frac{2\pi}{\hbar}|V_{\mathrm{ij}}|^2\ \mathrm{FCWD}. \tag{2.39}$$

Here, FCWD is the Franck-Condon weighted density of states. It is noted that the vibrational degrees of freedom are treated classically here. In the high temperature limit, i.e., $\hbar\omega << kT$, and $|V_{ij}| << \lambda$, i.e, weak coupling regime, FCWD is expressed as

$$\text{FCWD} = \sqrt{\frac{1}{4\pi k_B T\lambda}} \exp\left(-\frac{(\lambda + \Delta G_{ij})^2}{4\lambda k_B T}\right). \tag{2.40}$$

In the above equation, λ and ΔG_{ij} represent total reorganization energy and change in the free energy, respectively. k_B and $\hbar$ are the Boltzmann and reduced Planck's constants, respectively. Inserting this into the Eq. 2.39 results in the Marcus equation as

$$k_{i,j} = \frac{|V_{ij}|^2}{\hbar}\sqrt{\frac{\pi}{\lambda k_B T}} \exp\left(-\frac{(\lambda + \Delta G_{ij})^2}{4\lambda k_B T}\right). \tag{2.41}$$

2.9 Reorganization energies

λ, the reorganization energy as shown in Eq. 2.41, is the energy associated with the structural modifications of the system during the charge transfer. λ is usually divided into two different contributions as

$$\lambda = \lambda_{int} + \lambda_{ext}. \tag{2.42}$$

Here, λ_{int} and λ_{ext} are the internal and external reorganization energies, respectively. The internal geometry rearrangement in a system following addition or removal of a charge gives the internal reorganization energy. Considering D/A systems like the ones we are interested in, λ_{int} is the sum of the reorganization energies of donor (λ_D) and that of the acceptor (λ_A) written as λ_{int} can be written as

$$\lambda_{int} = \lambda_D + \lambda_A. \tag{2.43}$$

The λ_D and λ_A can be calculated using the four-point method[80–82] as $\lambda_D = E^+(D^0) - E^+(D^+)$ and $\lambda_A = E^0(A^-) - E^0(A^0)$. Here $E^+(D^+)$ and $E^+(D^0)$ represent the energies of donor cations at cation-optimized and at optimized ground-state geometries, respectively. Similarly, $E^0(A^-)$ and $E^0(A^0)$ are the energies of neutral acceptor at optimized anion and optimized neutral geometries, respectively.

The λ_{ext} contains the effect of polarization of the surrounding medium. Usually, the Marcus' implicit two-sphere formula in a continuum solvent[83, 84] shown in the Eq. 2.44 is used:

$$\lambda_{ext} = \frac{1}{4\pi\varepsilon_0}(\Delta e)^2 \left(\frac{1}{2a_1} + \frac{1}{2a_2} - \frac{1}{R}\right)\left(\frac{1}{\varepsilon_{op}} - \frac{1}{\varepsilon_0}\right). \tag{2.44}$$

Here a_1 is the donor radius, a_2 is the acceptor radius, and R is the distance between the center of donor and acceptor, respectively. ε_{op} and ε_0 are optical and zero-frequency dielectric constants of the surrounding media, respectively. Δe is the charge transferred from donor to acceptor. But explicit computation of λ_{ext} has been a topic of intense study, and various methodologies have been suggested for its accurate computation.[85–88] Instead of calculating this parameter explicitly, a parameter found for similar systems is usually used in literature. This method has worked well in many cases. For example, the external reorganization energy for composites with fullerene or substituted fullerene systems is around 0.1-0.3 eV[84, 89, 90] and a value within this range has been used at many places in literature providing good results.[89, 91–93] In the thesis, we have used a value of 0.3 eV for λ_{ext}.

2.10 Electronic coupling and the generalized Mulliken-Hush theory

The electronic coupling (denoted as V_{ij} in Eq. 2.41) describes the strength of coupling between initial and final diabatic states. As mentioned in the section 2.8, this is defined as $\langle\psi_i|\hat{V}|\psi_j\rangle$, where ψ_i and ψ_j are the two diabatic states. Since

the value depends on the two wave functions, it is very sensitive to the positions of the molecules, and their internuclear distance. Various methods are proposed in the literature for its evaluation. In the following, we will only briefly describe the generalized Mulliken-Hush (GMH) method.

The GMH method was developed by Cave and Newton[94, 95] based on the work of Mulliken[96, 97] and Hush.[98] Derivations of the GMH formula can be found in Refs.[99, 100] Consider a two-state system described by adiabatic wave functions ψ_1 and ψ_2 corresponding to the two adiabatic energies E_1 and E_2. Starting with two diabatic states ϕ_a and ϕ_b, the above two adiabatic states can be written as

$$\begin{aligned} \psi_1 = \quad & c_a\phi_a \quad + c_b\phi_b \\ \psi_2 = \quad & -c_b\phi_a \quad + c_a\phi_b. \end{aligned} \tag{2.45}$$

As the overlap between the two diabatic states is zero, we have

$$c_a c_b = \frac{V_{\mathrm{ij}}}{E_2 - E_1}. \tag{2.46}$$

The transition dipole moment between the ground and excited states can be written in terms of the adiabatic states as μ_{12}=$\langle\psi_1|\mathbf{r}|\psi_2\rangle$. Using Eq. 2.45, μ_{12} can be put in the diabatic basis as

$$\mu_{12} = c_a c_b \left(\langle\phi_b|r|\phi_b\rangle - \langle\phi_a|r|\phi_a\rangle\right). \tag{2.47}$$

This expression can be rewritten using the Eq. 2.46 as

$$\mu_{12} = \frac{V_{\mathrm{ij}}}{E_2 - E_1} \left(\langle\phi_b|r|\phi_b\rangle - \langle\phi_a|r|\phi_a\rangle\right). \tag{2.48}$$

Rewriting $\langle\phi_b|r|\phi_b\rangle$ and $\langle\phi_a|r|\phi_a\rangle$ in adiabatic basis, Eq. 2.48 can be written as

$$\mu_{12} = \frac{V_{\mathrm{ij}}}{E_2 - E_1} \sqrt{(\mu_{11} - \mu_{22})^2 + 4\mu_{12}^2}. \tag{2.49}$$

Here μ_{11} and μ_{22} are the adiabatic μs. Rearranging Eq. 2.49 results in the GMH formula as

$$V_{\mathrm{ij}} = \frac{\mu_{12}(E_2 - E_1)}{\sqrt{(\mu_{11} - \mu_{22}) + 4\mu_{12}^2}}. \tag{2.50}$$

We have used the Eq. 2.50 in our studies.

2.11 Free energy changes and exciton binding energy

As mentioned already, ΔG in Eq. 2.41 is the Gibbs free energy of the reaction. A negative value of ΔG indicates the feasibility of a process, and in our case, the charge transfer between two sites. ΔG_{CT}, the Gibbs free energy for a charge transfer process, is calculated using the Rehm-Weller equation[101, 102] as

$$\Delta G_{\mathrm{CT}} = \mathrm{IP_D} - \mathrm{EA_A} - E_{\mathrm{g}}^1 + E_{\mathrm{coul}}. \tag{2.51}$$

Here $\mathrm{IP_D}$ and $\mathrm{EA_A}$ are the adiabatic ionization potential of the donor and electron affinity of the acceptor, respectively. These two terms are calculated as $\mathrm{IP_D} = E^+(\mathrm{D}^+) - E^0(\mathrm{D}^0)$ and $\mathrm{EA_A} = E^0(\mathrm{A}^0) - E^-(\mathrm{A}^-)$. Here $E^0(\mathrm{D}^0)$ and $E^-(\mathrm{A}^-)$ are the energies of neutral donor at optimized neutral, and anion acceptor at optimized anion geometries. E_{g}^1 in Eq. 2.51 is the lowest excitation energy of the donor. E_{coul} in Eq. 2.51 is the Coulombic interaction energy between the cation of donor and anion of acceptor. This is computed as[103] $E_{\mathrm{coul}} = \sum_{g\in D, h\in A} \frac{q_{\mathrm{g}} q_{\mathrm{h}}}{\epsilon\, r_{\mathrm{gh}}}$, where q_{g} and q_{h} are the partial charges on atoms g and h of the donor and acceptor, respectively. r_{gh} is the distance between the two atoms and ϵ is the dielectric constant. In our work, we approximate this interaction energy as the negative of exciton binding energy (denoted as E_{b}). E_{b} is defined as the difference between the fundamental and optical bandgaps.[104, 105]

As discussed in the Chapter 1, charge transfer process competes with the charge recombination process in an OSC. The Gibbs free energy for charge recombination, denoted as ΔG_{CR}, is estimated as:[93, 103, 106, 107]

$$\Delta G_{\mathrm{CR}} = \mathrm{IP_D} - \mathrm{EA_A}. \tag{2.52}$$

Chapter 3

Designing fluorinated benzodithiophene-triazole based oligomers for high open circuit voltage in organic photovoltaics

---

In this chapter, structural, optoelectronic, and charge transport properties of fluorinated benzodithiophene-triazole-based oligomers are investigated. A part of the content of this chapter is published in *Computational and Theoretical Chemistry*, **2019**, 1165, 112564.

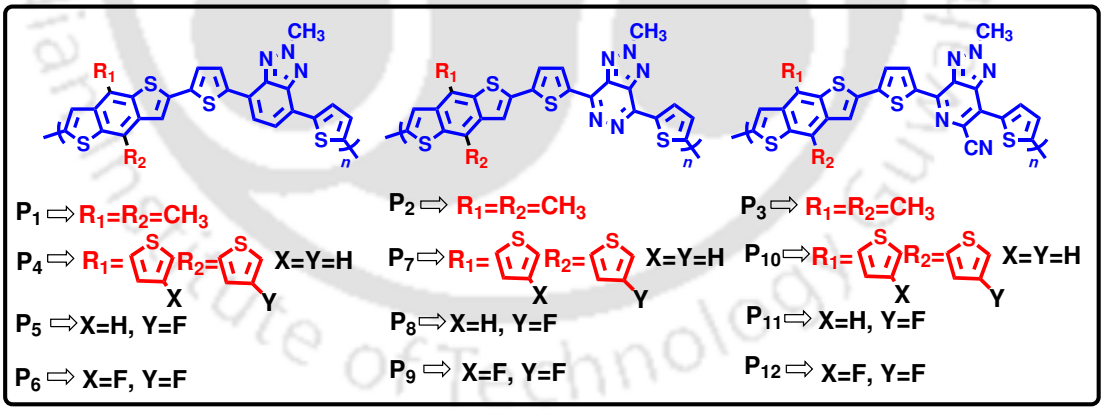

Figure: Effect of fluorination on the properties of BDT-TAZ based oligomers

3.1 Introduction

In recent times, BDT has emerged as one of the widely used donor materials.[14, 22, 31, 32, 108–111] BDT has a rigid planar conjugated structure and shows good stacking property, which is beneficial to achieve tunable energy levels, suitable bandgaps and enhance the charge carrier mobilities. Ultra low bandgap polymers based on fluorene-substituted thiadiazoloquinoxaline acceptor and BDT donor units[110] have been able to deliver PCEs up to 8.15%. Simultaneously fluorinated and alkylthiolated BDTT based polymers[112] produced devices with PCE up to 9.72%. In one of the earlier works, a device based on BDT and benzotriazole (denoted as **P1**) reported a PCE $\sim$ 4%.[1] Follow-up work by You and co-workers[2] reported medium bandgap conjugated polymers based on BDT and either pyridazine-fused triazole (denoted as **P2**) or a cyano substituted pyridine-fused triazole (denoted as **P3**). For **P3**, the highest PCE value of 8.4% has been obtained. Structural modifications such as replacement of alkyl groups by thienyl groups in BDT have shown improvements in the planarity, charge carrier properties and PCE.[113] Moreover, when the thienyl group in the BDT unit was further modified by introducing electron withdrawing fluorine (-F) atom, it resulted in an increase of PCE up to 8.6%.[39]

Understanding the structure property relationship is vital to gain details of mechanisms of various processes. In this scenario, computational studies help to get a quick look at various properties at the molecular level before an experiment is carried out.[32, 114–120] In the present work, we have modified the parent molecules, **P1**, **P2** and **P3** as follows: in the first case, the alkyl groups in benzodithiophene are replaced by thienyl rings producing **P4**. **P4** is again modified by replacing one of the hydrogens in one of the thienyl rings by a fluorine atom resulting in **P5**. When a hydrogen atom in the second thienyl ring of **P5** is replaced by a fluorine atom, the result is **P6**. These **P1** and **P4-P6** compounds form the first set. In a similar way, **P2** and **P3** are modified to produce the derived molecules **P7-P9** and **P10-P12**, respectively, resulting in two other sets of molecules (see

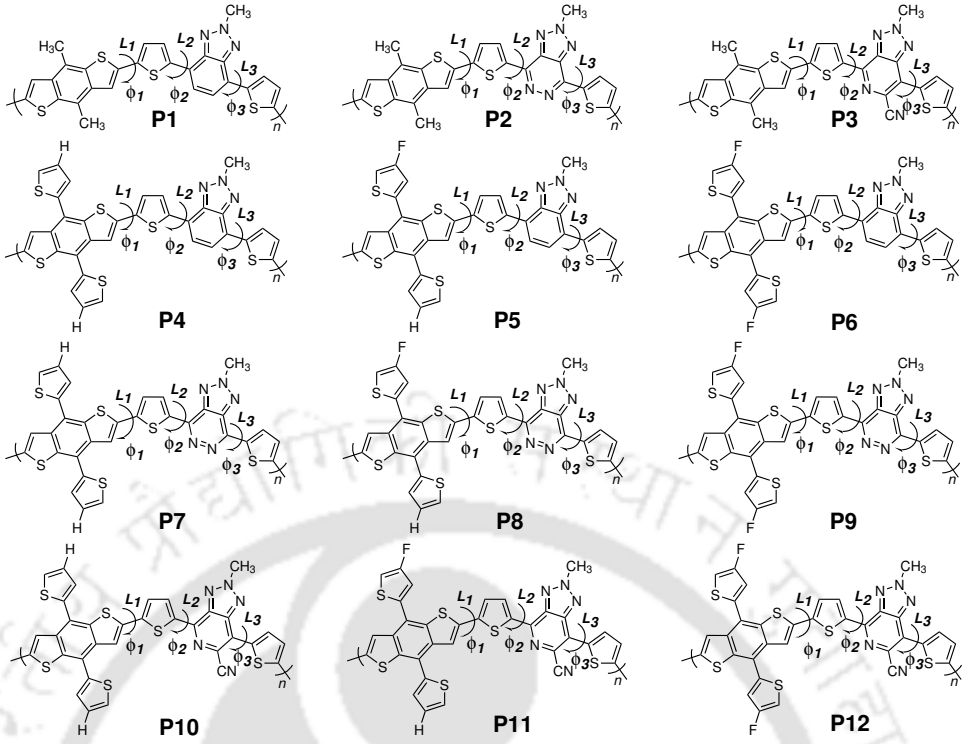

FIGURE 3.1: Molecular structures of the donor-acceptor repeating units, where n= 1-4. Selected bonds and dihedral angles are labeled as L_i and ϕ_i, i =1, 2, 3,..., respectively. The bridge-bonds between monomeric units are also included in counting L_is.

Figure 3.1 for all the structures). Following optimizations of the geometries, various properties of the oligomers are calculated and their dependence on the chain length are discussed. This is followed by a comparison of charge mobilities. In conclusion, we comment upon the suitability of these oligomers for solar cells.

3.2 Computational Methodologies

DFT based methods are used to study the present systems. Ground state optimization studies are carried out with both the B3LYP[55] and HSE06[121] functionals. This is to be noted that B3LYP has been one of the preferred choices for studying the ground states of conjugated donor-acceptor oligomers, but recent literature reports have shown that various long-range corrected functionals and especially the screened hybrid HSE06 produce very good results, comparable with the experimental results.[114, 118, 122, 123] The 6-31G(d,p) basis set

TABLE 3.1: The HOMO and LUMO values (eV) of **P1-P3** tetramers. HOMO values are calculated using Model 2 as described in main text. Similarly, LUMO values presented here are calculated using Model 6.

Compounds	HSE06		B3LYP		Exp.[1, 2]	
	E_{HOMO}	E_{LUMO}	E_{HOMO}	E_{LUMO}	E_{HOMO}	E_{LUMO}
P1	-5.14	-3.15	-5.15	-3.16	-5.29	-2.87
P2	-5.33	-3.41	-5.35	-3.42	-5.66	-3.73
P3	-5.39	-3.54	-5.41	-3.56	-5.67	-3.83

was used in all the calculations. Vibrational frequencies are calculated for all the optimized geometries and those are found to be real. In addition, as shown in Table 3.1, the calculated HOMO and LUMO energies of **P1-P3** at HSE06 and B3LYP level are close to the experimental values. Hence, we report the ground state geometries of neutrals, cations and anions computed with HSE06 only. We note here that the HOMO and LUMO energies are calculated using the models as described below. Various models[124–126] have been proposed to estimate the HOMO and LUMO energies to reproduce experimental values. Recently, Hückel method based models[125] have been found to be quite successful. In our calculations, four different models are examined to estimate the HOMO values: (1) in Model 1, the energy of HOMO from the neutral singlet ground state optimized geometry; (2) in Model 2, the difference between the total energy of neutral singlet ground state and the total energy of oxidized (+1) doublet; (3) in Model 3, the energy difference between the first excitation energy (E_g^1) and the αHOMO energy of the neutral triplet state; (4) in Model 4, the single point energy of αLUMO of oxidized doublet state. Mean absolute error (MAE) values are calculated for the three experimentally prepared molecules and as shown in the Table A1 (see Appendix A), the smallest mean absolute error (MAE) value occurs for Model 2. As the HOMO energies calculated using the Model 2 are in better agreement with the experimental values, these energies are considered as the HOMO values.

For LUMOs, six different models were used: (1) in Model 1, the energy of LUMO from the neutral singlet ground state optimized geometry; (2) in Model 2, the difference between the total energy of neutral singlet ground state and the

TABLE 3.2: First excitation energy (E_g^1 in eV) and maximum absorption wavelength (λ_{max} in nm) data obtained various functionals with the 6-31G(d,p) basis set. Experimental values are taken from Refs.[1, 2]

	PBE0		B3LYP		CAM-B3LYP		ωB97XD		Exp.
	E_g^1	λ_{max}	E_g^1	λ_{max}	E_g^1	λ_{max}	E_g^1	λ_{max}	E_g^1
P1	1.99	624.37	1.86	664.06	2.42	511.13	2.52	491.46	1.98
P2	1.92	645.16	1.79	692.08	2.41	513.90	2.52	491.66	1.93
P3	1.85	671.91	1.72	720	2.32	534.30	2.42	510.78	1.84

single point energy of reduced (-1) doublet; (3) in Model 3, the energy of αHOMO of reduced (-1) doublet; (4) in Model 4, the difference between the energy of neutral singlet ground state optimized geometry and the single point energy of neutral triplet state; (5) the αHOMO energy of the neutral triplet state and (6) the energy of the HOMO obtained using the Model 2 plus E_g^1 (obtained from TD-DFT calculations). As in calculations of HOMO values, we computed MAEs in the cases of LUMO energies for various models. As shown in Table A2 (see Appendix A), MAE is smallest for the Model 6, and hence, the Model 6 is considered for all the systems to compute the LUMO values.

For **P1**, **P2** and **P3**, absorption spectra are calculated using four different functionals, PBE0, B3LYP, CAM-B3LYP and ωB97XD with the 6-31G(d,p) basis set. As shown in Table 3.2, E_g^1 of **P1-P3** obtained at the TD-PBE0/6-31G(d,p) level agree better with the experimental values.[1, 2] Hence, we have used the PBE0 functional for all the newly designed systems. EA, IP, and λ are calculated at HSE06/6-31G(d,p) level based on the neutral and charged optimized geometries. All calculations were carried out using Gaussian 09 software.[127]

3.3 Theoretical methodology for charge transport properties

Charge transport process is usually described by two types of models: coherent band and the thermally activated hopping models.[128, 129] Band model is used

in perfectly ordered systems at low temperatures. Hole and electron charge carrier properties fall in the regime of coherent band theory.[128] However, at room temperature the charge transfer generally follows the hopping model.[130–132] In the present investigation, we have used the hopping model to compute the charge transport rate and mobilities of the charges. Charge hopping rate (k_{hop}) between two adjacent molecules can be described by the Marcus theory[133, 134] and is expressed as

$$k_{\mathrm{hop}} = \frac{V_{\mathrm{ab}}^2}{\hbar}\left(\frac{\pi}{\lambda k_{\mathrm{B}} T}\right)^{\frac{1}{2}} \exp\left(-\frac{\lambda}{4\mathrm{k_B T}}\right). \tag{3.1}$$

This expression is the same Marcus' formula that was presented in Chapter 2. However, in this case, ΔG is put to zero for the self-exchange process. Here V_{ab} is the charge transfer integral, λ is the reorganization energy, T is the room temperature and k_{B} and $\hbar$ are the Boltzmann and Planck's constants, respectively. As it is clear from the expression, the charge transfer rate depends on the charge transfer integral and reorganization energy.

The charge transfer integral describes the strength of electronic coupling between two identical and symmetric molecules. These values for holes (V_{h}) and electrons (denoted as V_{e}) are calculated as [135, 136]

$$V_{\mathrm{h}} = \frac{E_{\mathrm{HOMO}} - E_{\mathrm{HOMO-1}}}{2} \text{ and } V_{\mathrm{e}} = \frac{E_{\mathrm{LUMO+1}} - E_{\mathrm{LUMO}}}{2}. \tag{3.2}$$

Here E_{HOMO}, $E_{\mathrm{HOMO-1}}$, $E_{\mathrm{LUMO+1}}$ and E_{LUMO} are the energies of HOMO, HOMO-1, LUMO+1 and LUMO, respectively. The charge hopping mobility μ_{hop} can be estimated from the relation

$$\mu_{\mathrm{hop}} = \frac{eD}{k_{\mathrm{B}} T}, \tag{3.3}$$

where e is the electronic charge, k_{B} is the Boltzmann constant, T is the room temperature and D is the diffusion constant. The diffusion constant is calculated

from k_{hop} as[131, 137]

$$D = \frac{1}{2} k_{\text{hop}}\, l^2, \tag{3.4}$$

where l is the distance between two adjacent molecules. Hence, the mobility can be expressed as[135, 138]

$$\mu_{\text{hop}} = \frac{el^2}{2k_{\text{B}}T} k_{\text{hop}}. \tag{3.5}$$

3.4 Results and discussion

3.4.1 Optimized geometries and electronic properties of all polymers

Ground-state geometries affect the optoelectronic properties, π-π stacking, charge-transfer integral and charge mobilities in polymers.[139, 140] Hence, it is necessary to analyze the ground-state structures. The structures of the tetramers of all the compounds are shown in Figures 3.2 and A1-A3 (see Appendix A). Lengths of selected bonds, denoted as L_i, and values of the selected dihedral angles, denoted as ϕ_i, are tabulated in Tables A3 and A4, respectively (see Appendix A). As observed in Table A3, the selected optimized bond lengths do not change too much with the oligomer size which indicates that tetramers can be used to describe the structures of the polymers. The L_i values of all the oligomers are between 1.43-1.45 Å and these values are shorter than that of a typical C–C single bond (1.54 Å). This hints at double bond character of these bonds due to π electron delocalization. Replacement of methyl group by thienyl group brings a lot of changes in the dihedral angles. As reported in Table A4, the ϕ_i values of the oligomers are in the range 0–12°. When the methyl group in **P1** was replaced by thienyl group resulting in **P4**, it was found that ϕ_1 increased substantially from 2.87 to 10.19°. Similarly, in case of dimer, ϕ_1 and ϕ_5 were found to increase from 0.96 to 10.09° and from 2.96 to -3.47°, respectively. Likewise, in trimer, the dihedral angles ϕ_1,

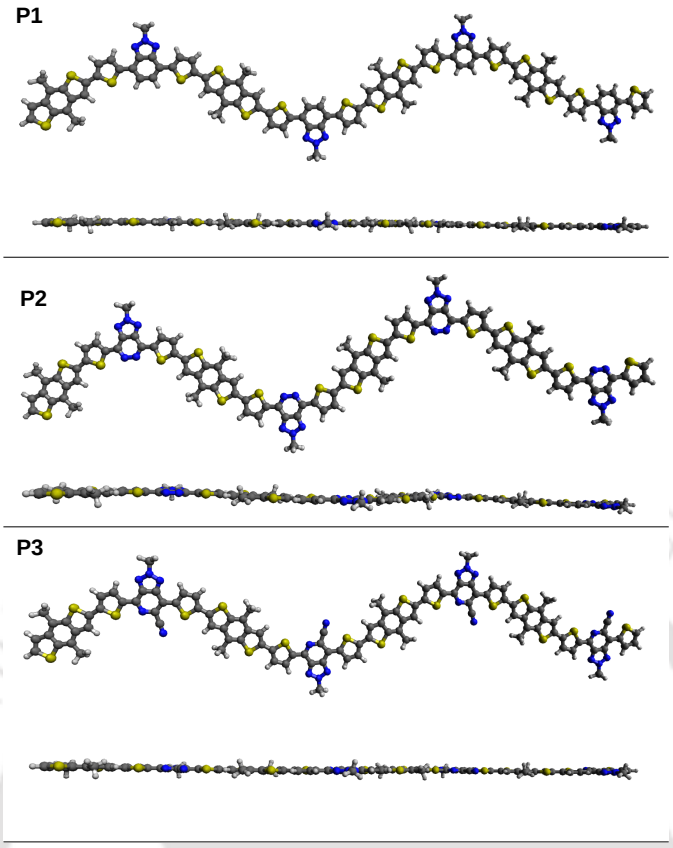

FIGURE 3.2: Optimized ground state geometries for tetramers of **P1**-**P3** calculated at HSE06/6-31G(d,p) level. Colour code: white (H), grey (C), yellow (S), and blue (N).

ϕ_2, ϕ_5 and ϕ_9 changed from 1.44 to -10.70°, 0.00 to 1.84°, 0.88 to -2.28° and 0.51 to -9.33°, respectively. Similar results were obtained in the case of tetramer too. When **P4** is modified to **P5** and further to **P6** by introduction of fluorine atoms, the changes in dihedral angle values were found to be small. From **P2** to **P7** monomers, it was observed that the dihedral angle values ϕ_1 increased from 2.38 to 11.03°. In case of dimers, the values of ϕ_1, ϕ_4 and ϕ_5 were observed to change from 1.32, 1.12 and 1.17 to -10.88°, -2.10° and -2.43°, respectively. Similarly, in trimer, ϕ_1, ϕ_8 and ϕ_9 were found to be increased from 2.06, 1.05 and 0.42 to 11.44°, 9.87° and 9.89°, respectively. Similar trends are observed in cases of **P3** to **P12**.

3.4.2 HOMOs, LUMOs and V_{oc}

As is known, suitable positioning of the frontier molecular orbitals is a primary requirement for the construction of OPVs. Calculated HOMO and LUMO values

TABLE 3.3: Energies of frontier molecular orbitals of all the tetramers and **PCBM**. ΔE_{LL} is the difference between the LUMO energies of the donors **P1-P12** and of **PCBM**. V_{oc} values of all tetramer/**PCBM** devices are also shown. All the energies are in eV.

Compounds	E_{HOMO}		E_{LUMO}		ΔE_{LL}	V_{oc}(V)	
	Calc.	Exp.	Calc.	Exp.		Calc.	Exp.
P1	-5.14	-5.29	-3.15	-2.87	1.15	0.54	0.68
P2	-5.33	-5.66	-3.41	-3.73	0.89	0.73	0.95
P3	-5.39	-5.67	-3.54	-3.83	0.76	0.79	0.96
P4	-5.15		-3.16		1.14	0.55	
P5	-5.21		-3.22		1.08	0.61	
P6	-5.28		-3.29		1.01	0.68	
P7	-5.33		-3.38		0.92	0.73	
P8	-5.40		-3.45		0.85	0.80	
P9	-5.48		-3.52		0.78	0.88	
P10	-5.38		-3.51		0.79	0.78	
P11	-5.46		-3.57		0.73	0.86	
P12	-5.53		-3.64		0.66	0.93	
PCBM		-6.00		-4.30			

of tetramers of **P1-P12** are tabulated in Table 3.3. As the Table shows, replacements of the methyl groups in **P1**, **P2** and **P3** by thienyl groups resulting in **P4**, **P7** and **P10**, respectively, change the HOMO and LUMO values slightly. From **P4** to **P5** , the HOMO value decreases by 0.06 eV, and from **P4** to **P6** the value decreases 0.13 eV. A similar trend is seen in case of LUMOs of **P4** to **P6**. Similar results are obtained for **P7** to **P9** and for **P10** to **P12**. Overall, it is observed that both the HOMO and LUMO energies decrease as the number of fluorine atoms increases. As such, **P12** has the smallest of HOMO and LUMO values. Fullerene derivatives are one of the most widely used electron acceptors. Hence, we have chosen $PC_{61}BM$ (**PCBM**) as the electron acceptor in this work. Experimentally determined HOMO and LUMO values of **PCBM** are also tabulated in Table 3.3, along with the differences between the LUMO of **PCBM** and those of tetramers, ΔE_{LL}. All the ΔE_{LL} values are larger than 0.3, which ensures efficient electron transfer.

V_{oc} values of all oligomers are in the range 0.54 - 0.93 V (see Table 3.3). As observed, **P1** and **P12** have the lowest and the highest V_{oc} values, respectively. It is

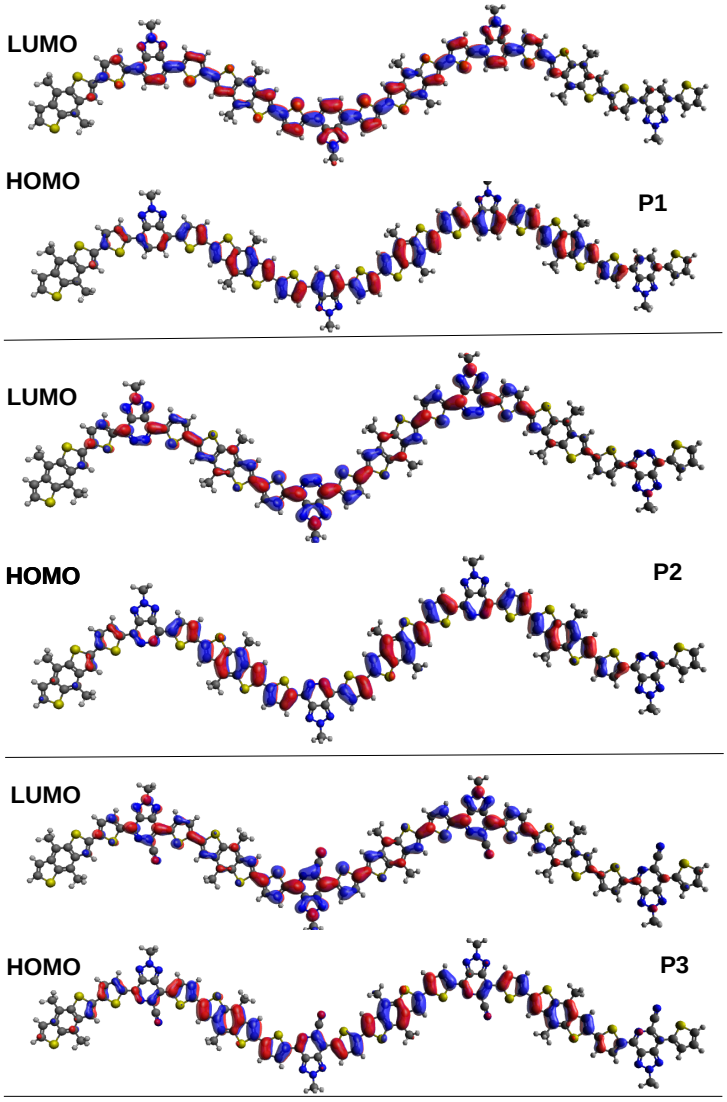

FIGURE 3.3: HOMO and LUMO orbitals for the tetramers of **P1** -**P3** at HSE06/6-31G(d,p) level.

found that the introduction of thienyl group does not affect the V_{oc} values. Rather, substitution of thienyl hydrogen(s) by fluorine atom(s) results in increasing the V_{oc}. From **P4** to **P5**, the V_{oc} value increases by 0.06 V, while after difluorination on BDT, the difference doubles. A similar trend is seen in cases of derivatives of **P2** and **P3**. The calculated V_{oc} values sequence are **P1** < **P4** < **P5** < **P6** < **P2** ≈ **P7** < **P10** < **P3** < **P8** < **P11** < **P9** < **P12**.

Contours plots of HOMOs and LUMOs of **P1**-**P3** and **P4**-**P12** are shown in Figures 3.3 and A4-A6 (see Appendix A). These orbitals are mainly localized in

TABLE 3.4: Percentage contributions of the three different fragments to HOMOs ($\%_{HOMO}$) and LUMOs ($\%_{LUMO}$) of **P1- P12** oligomers.

Fragments	**P1**		**P2**		**P3**		**P4**		**P5**		**P6**	
	$\%_{HOMO}$	$\%_{LUMO}$	$\%_{HOMO}$	$\%_{LUMO}$	$\%_{HOMO}$	$\%_{LUMO}$	$\%_{HOMO}$	$\%_{LUMO}$	$\%_{HOMO}$	$\%_{LUMO}$	$\%_{HOMO}$	$\%_{LUMO}$
1	41.91	27.15	52.29	20.60	51.53	19.55	42.01	31.22	40.61	32.29	39.30	33.45
2	39.71	38.07	36.70	34.23	35.46	33.92	39.31	36.49	39.98	36.22	40.63	35.87
3	18.28	34.55	11.00	45.16	12.84	46.48	18.65	32.28	19.29	31.42	19.93	30.54
	P7		**P8**		**P9**		**P10**		**P11**		**P12**	
	$\%_{HOMO}$	$\%_{LUMO}$	$\%_{HOMO}$	$\%_{LUMO}$	$\%_{HOMO}$	$\%_{LUMO}$	$\%_{HOMO}$	$\%_{LUMO}$	$\%_{HOMO}$	$\%_{LUMO}$	$\%_{HOMO}$	$\%_{LUMO}$
1	54.79	22.94	53.24	23.79	51.83	24.69	54.83	21.40	53.26	22.13	51.72	22.89
2	34.79	33.43	35.77	33.40	36.77	33.33	33.12	33.28	34.17	33.23	35.17	33.17
3	10.50	43.60	10.90	42.72	11.33	41.97	12.04	45.30	12.55	44.62	13.10	43.93

the central part of the tetramer oligomers. Electron densities in case of HOMOs are delocalized over electron donating BDT units, bridge thiophenes as well as benzene, pyridazine and pyridine rings of the electron acceptor units and these are of π-bonding type. In the case of LUMOs, the densities are delocalized over all the units except one of the donor BDT units towards the terminus. This hints at possibility of charge transfer character.

Fragment contributions to the MOs are calculated using the Hirshfeld analysis using the Multiwfn software.[141] Three fragments are defined: fragment 1 consists of all the BDT units, fragment 2 is made up of all the eight bridge thiophene units and fragment 3 consists of all the triazoles. Percentage contributions of these fragments to the frontier MOs for **P1**-**P12** are shown in Table 3.4. For the HOMO of **P1**, there is almost an equal contribution from fragments 1 and 2. Similar results are obtained for HOMOs of **P4**-**P6** as **P4**-**P6** are derived from **P1**. For HOMOs of **P2** and **P3**, there are much larger contributions by the BDT units than the bridge-thiophenes and the triazoles. Similar results are obtained for **P7**-**P12**. For LUMOs, while there is a comparatively smaller contribution from fragment 1 in **P1**, there is almost an even contribution from all the three fragments in **P4**-**P6**. For **P2** and **P3**, the contributions by fragment 1 are comparatively much smaller than the other two and the trend remains the same for **P7**-**P12**.

To have a better understanding of the percentage contributions, another set of analysis has been carried out for all the tetramers where each unit (BDT, thiophene and triazole) is considered as a fragment. The results are tabulated

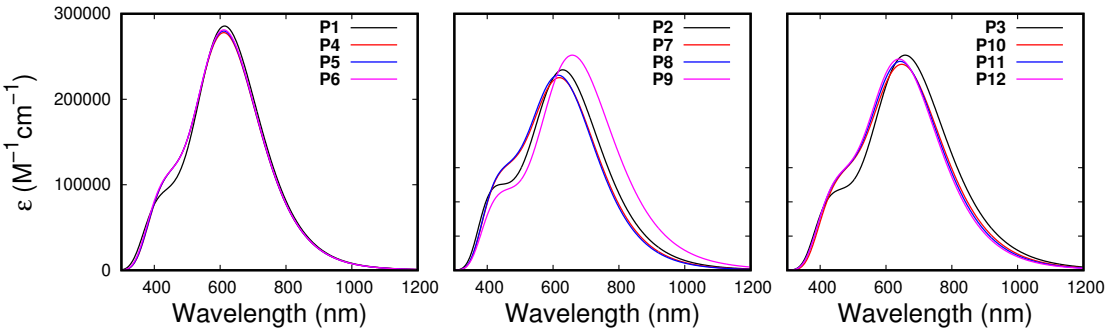

FIGURE 3.4: Absorption spectra of the investigated tetramers. Half-width at half-maximum height is 2685 cm^{-1}.

in Table A5 (see Appendix A). The data in the table shows that contributions of BDT/ thiophene/triazole units increase as we move towards the centre of the tetramers. For **P1** and **P4-P6**, the contributions remain similar. From **P2** to **P7-P9** and from **P3** to **P10-P12**, contributions of the units remain similar except that the two central BDT units contribute a little more in the cases of new tetramers than those in the parent compounds.

3.4.3 Spectral properties

Computed absorption spectra are shown in Figure 3.4. As observed in the figure and shown in Table 3.5, λ_{max} of parent compounds match very well with the experimental results. Computed λ_{max} values for **P1**, **P2** and **P3** tetramers are 624.37, 645.16 and 671.49 nm while the experimental values are 626, 641 and 673 nm[1, 2], respectively. Comparing **P1** with **P4**, **P5** and **P6**, it is clear that there is very little difference in the absorption spectra of these tetramers. In **P4-P6**, λ_{max} values are 623.68, 623.40 and 623.42 nm, respectively. Similar observations can be made in the other two cases, although the derived compounds are slightly blue-shifted in comparison to the parent ones. λ_{max} values for tetramers of **P7-P9** are little smaller and the values decrease with addition of fluorine atoms. For **P10-P12**, maximum absorption wavelengths are 665.53, 660.37 and 655.66 nm, respectively and as was the case with **P7-P9** versus **P2**, these values are smaller than the parent **P3** and decrease with addition of fluorine atoms. It is

TABLE 3.5: Electronic transition data for $S_0 \rightarrow S_1$ for all the tetramers. E_g^1, λ_{max}, f_{osc}, η_λ, H and L denote excitation energy, maximum wavelength, oscillator strength, light-absorption efficiency, HOMO and LUMO, respectively.

Compounds	E_g^1(eV)	λ_{max}(nm)	Configurations	f_{osc}	η_λ	E_g^1(eV)
P1	1.99	624.37	H→ L(0.76)	6.52	0.99	1.98
P2	1.92	645.16	H→ L(0.76)	5.16	0.99	1.93
P3	1.85	671.91	H→ L(0.76)	5.67	0.99	1.84
P4	1.99	623.68	H→ L(0.72)	6.27	0.99	
P5	1.99	623.40	H→ L(0.70)	6.32	0.99	
P6	1.99	623.42	H→ L(0.70)	6.36	0.99	
P7	1.94	638.74	H→ L(0.72)	4.83	0.99	
P8	1.95	634.87	H→ L(0.72)	4.91	0.99	
P9	1.96	631.27	H→ L(0.70)	4.98	0.99	
P10	1.86	665.53	H→ L(0.76)	5.29	0.99	
P11	1.88	660.37	H→ L(0.76)	5.38	0.99	
P12	1.89	655.66	H→ L(0.72)	5.47	0.99	

also noteworthy that the order of λ_{max} of the derived compounds follow the same order as those of the parent compounds (see Fig. 3.4).

Other details of $S_0 \rightarrow S_1$ transitions including molecular orbitals involved, f_{osc} and light-absorption efficiency (η_λ) of tetramers are also shown in Table 3.5. As is observed, all the transitions are HOMO to LUMO excitations and the corresponding oscillator strengths are very large. η_λ is expressed as[106, 142]

$$\eta_\lambda = 1 - 10^{-f_{osc}}, \tag{3.6}$$

Values of η_λ are calculated considering the $S_0 \rightarrow S_1$ transition peaks. It is observed that all tetramers show good light-absorption efficiencies.

Instead of comparing f_{osc} values, a better relative comparison is usually made in terms of specific absorption strength (f_M). f_M is defined as the absorption strength per unit mass.[143, 144] Light harvesting capability of a polymer can be understood in terms of f_M and E_g^1. A plot of f_M values versus E_g^1 is shown in Figure 3.5, for the tetramers. This figure shows that **P3** has the smallest E_g^1 amongst all and additionally, it has the second largest f_M value. Hence, this would be considered as the most efficient to harvest light. Among **P4**-**P12**, **P10**-**P12**

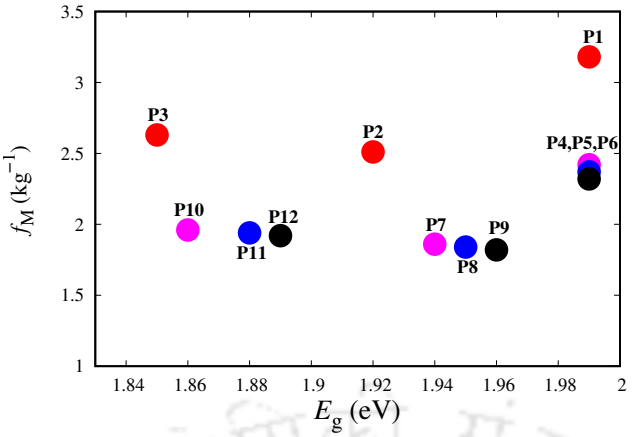

FIGURE 3.5: The relation between specific-absorption strength and transition energies.

have lowest E_g^1 and f_M values ≈ 2. **P4-P6** tetramers show the largest f_M and E_g^1, hence can be considered as having low light harvesting efficiency. It is to be noted that **P1** is having the largest f_M and E_g^1 values and hence, will be the poorest harvestor.

3.4.4 IPs and EAs

IPs and EAs are used to determine the hole and electron transfer barriers in donor-acceptor polymers. A smaller IP and a larger EA hint at easier injections of holes and electrons, respectively. Both vertical and adiabatic IPs/EAs are calculated in this study. These are defined as follows:

$$\mathrm{IP}(v) = [E^+(\mathrm{M}^0) - E^0(\mathrm{M}^0)] \tag{3.7}$$

$$\mathrm{IP}(a) = [E^+(\mathrm{M}^+) - E^0(\mathrm{M}^0)] \tag{3.8}$$

$$\mathrm{EA}(v) = [E^0(\mathrm{M}^0) - E^-(\mathrm{M}^0)] \tag{3.9}$$

$$\mathrm{EA}(a) = [E^0(\mathrm{M}^0) - E^-(\mathrm{M}^-)], \tag{3.10}$$

where $E^+(\mathrm{M}^0)/E^-(\mathrm{M}^0)$ are the energies of the cations/anions calculated at optimized structures of neutral molecules. $E^+(\mathrm{M}^+)/E^-(\mathrm{M}^-)$ are the energies of optimized structures of the cations/anions and $E^0(\mathrm{M}^0)$ are the energies of neutral

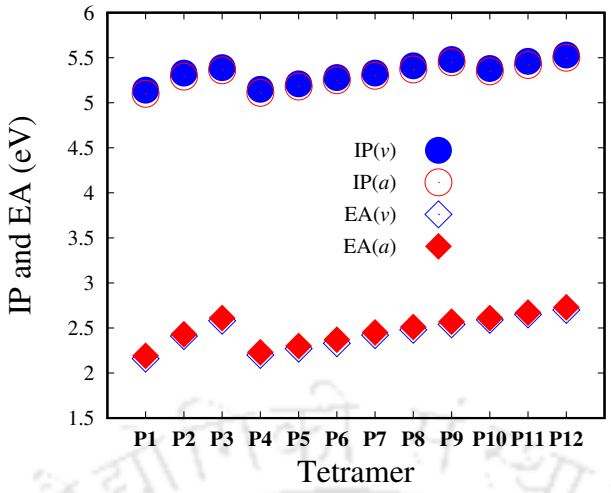

FIGURE 3.6: EA(v,a) and IP(v,a) values for all the studied tetramers.v and a stand for vertical and adiabatic values, respectively.

molecules in the ground state. Here, v and a represent vertical and adiabatic values, respectively. The IP and EA values for all the oligomers are plotted in Figure 3.6. As these show, the parent molecules follow the order **P1** < **P2** < **P3**, for both IP and EA values. Among the tetramers of **P4-P12**, the lowest IP was found for **P4**, and the largest EA was found for **P12**. As the number of hetero atoms like fluorine or substituents like CN are introduced, the values increase. As such, the series **P4-P6** have the lowest IP values. In each series, gradual introduction of F atom leads to an increase in IP values resulting in increased difficulty for hole injection. EAs of **P10-P12** tetramers are the largest amongst the series showing that the presence of -CN improves the EAs. As was the case with IPs, in each series, introduction of F- atom results in an increase in EA.

3.4.5 Reorganization energies

λ, intramolecular reorganization energy, is a sum of internal and external reorganization energies. Contribution of λ_{ext}, attributed to effect of surroundings, is small and in this study, we consider only the internal $\lambda(\lambda_{\text{int}})$. λ_{int} is the energy arising out of the geometry modifications occurring in a charged system derived from a neutral system. As is evident from Eq. 3.1, the lower

TABLE 3.6: Intramolecular reorganization energies for holes (λ_h) and electrons (λ_e) calculated at the HSE06/6-31G(d,p) level.

Compounds	λ_h(eV)				λ_e(eV)			
	n=1	n=2	n=3	n=4	n=1	n=2	n=3	n=4
P1	0.227	0.140	0.095	0.076	0.211	0.121	0.079	0.061
P2	0.235	0.142	0.097	0.075	0.207	0.111	0.072	0.055
P3	0.215	0.135	0.094	0.071	0.174	0.094	0.061	0.047
P4	0.204	0.125	0.087	0.068	0.208	0.118	0.080	0.062
P5	0.206	0.126	0.089	0.068	0.208	0.120	0.083	0.062
P6	0.207	0.128	0.090	0.069	0.218	0.123	0.084	0.063
P7	0.209	0.121	0.084	0.066	0.202	0.110	0.074	0.057
P8	0.214	0.123	0.085	0.067	0.203	0.112	0.075	0.057
P9	0.216	0.126	0.087	0.068	0.210	0.114	0.076	0.058
P10	0.196	0.120	0.083	0.064	0.177	0.098	0.066	0.050
P11	0.197	0.122	0.085	0.065	0.177	0.100	0.068	0.051
P12	0.198	0.124	0.087	0.066	0.185	0.103	0.069	0.051

the λ, the faster is the charge transport. The internal hole and electron reorganization energies (λ_h and λ_e, respectively) can be calculated by the following formulas[145, 146]: $\lambda_h = [E^+(M^0) - E^+(M^+)] + [E^0(M^+) - E^0(M^0)]$ and $\lambda_e = [E^-(M^0) - E^-(M^-)] + [E^0(M^-) - E^0(M^0)]$. Here $E^0(M^+)/E^0(M^-)$ represents the single-point energy of the neutral molecule calculated at cationic/anionic geometries. As the Table 3.6 shows, λ_h values of the derived tetramers are smaller than those of respective parent compounds, e.g., values for **P4**-**P6** are smaller than those for **P1** and so on. As such, λ_h values for **P4**-**P12** tetramers are similar and vary within 0.064 to 0.069 eV. In contrast, λ_e values of **P4**-**P12** tetramers show a larger range of variation, between 0.050 to 0.063, compared to λ_h values. For all the new tetramers, λ_es are always slightly larger than the values for respective parent tetramers. It is also observed from the table that both λs decrease with increase in the conjugated chain length.

TABLE 3.7: Charge transfer integral V_{ab}(eV), intermolecular distance D (Å), charge transport rates k_{hop} (s^{-1}) and mobilities μ_{hop} (cm^2 V^{-1} s^{-1}) of all tetramer oligomers.

Compounds	V_{ab}		D	$k_{hop} \times 10^{-13}$		μ_{hop}	
	hole	electron		hole	electron	hole	electron
P1	0.0512	0.0586	3.5	7.59	12.97	1.81	3.09
P2	0.0461	0.0497	3.5	6.34	10.41	1.51	2.48
P3	0.0476	0.0492	3.5	7.13	11.98	1.70	2.86
P4	0.0514	0.0565	4.0	8.77	11.72	2.73	3.65
P5	0.0494	0.0578	4.0	8.08	12.26	2.51	3.82
P6	0.0501	0.0593	4.0	8.23	12.69	2.56	3.95
P7	0.0450	0.0472	4.0	7.00	9.02	2.18	2.81
P8	0.0437	0.0491	4.0	6.46	9.68	2.01	3.01
P9	0.0444	0.0507	4.0	6.50	10.18	2.02	3.17
P10	0.0469	0.0458	4.0	7.89	9.79	2.46	3.05
P11	0.0463	0.0479	4.0	7.48	10.45	2.33	3.25
P12	0.0467	0.0497	4.0	7.51	11.22	2.34	3.49

3.4.6 Charge transfer integrals, rates of diffusion and charge mobilities

Charge transfer integrals, transfer rates and hopping mobilities are calculated using Eqs. 3.2, 3.1 and 3.5, respectively. Transfer rate calculations are performed at room temperature. For the charge transfer integrals, as mentioned already, parent molecules were π-stacked at a distance of 3.5 Å. On the other hand, π-stacks of tetramers of **P4-P12** were formed at 4.0 Å. Scanning of the stacking distance was carried out for few of the stacked tetramers at RI-M062X-D3 level using the Turbomole software[147] to arrive at either 3.5 Å or 4.0 Å. Introduction of side rings, which happen to be not in the plane of the main chain, increases the stacking distances in the **P4-P12** oligomers. Intermolecular distances, hole/electron transfer integrals, charge transfer rates and mobilities are listed in Table 3.7. π-stacked structures of all the tetramers are shown in Figures A7 and A8 (see Appendix A).

V_{ab} values of the new tetramers, **P4-P12**, differ from the values for **P1-P3** as seen in the Table 3.7. In particular, V_{ab} (hole) values of **P4**, **P7** and **P10** are closest to that of **P1**, **P2** and **P3**, respectively. The hole coupling value decreases

from **P4** to **P5**, but increases again for **P6**. The electron coupling value increases from **P4** to **P6** as the number of fluorine atoms on BDT increases. Similar trends are observed for **P7-P9** and for **P10-P12**, for both hole and electron coupling values. As is observed in Table 3.7, electron transfer rates are larger than hole transfer rates in all tetramer oligomers. **P4** and **P2** have the largest and the smallest hole transfer rates, respectively. On the other hand, **P7** has the smallest and **P1** has the largest of the electron transfer rates. The k_{hop}(hole) decreases from **P4** to **P5** and increases again for **P6**, in accordance with the V_{ab} values. Similar results are obtained for **P7-P9** and for **P10-P12**. The trend is different for k_{hop}(electron). The values increase from **P4** to **P6**, **P7** to **P9** and **P10** to **P12**, as the number of fluorine atoms increases.

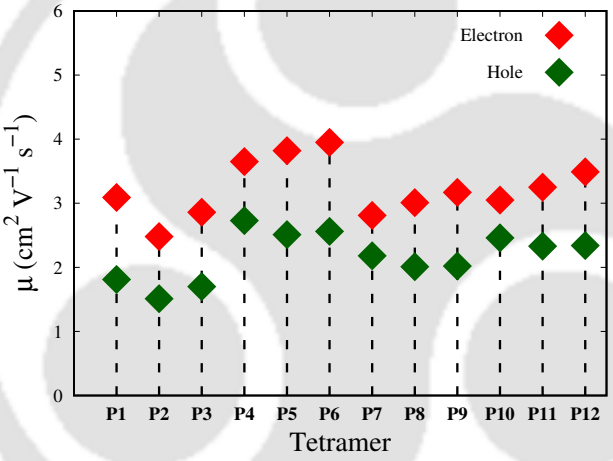

FIGURE 3.7: Electron and hole mobilities of all the tetramers.

As observed in Table 3.7, electron mobilities are always larger than the hole mobilities. As shown in Figure 3.7, new set of oligomers **P4-P12** possess larger hole and electron mobilities than the values for corresponding parent systems. The hole mobility decreases from **P4** to **P5** and increases again for **P6**, in accordance with the trend showed in charge transfer rates. Similarly, **P7-P9** and **P10-P12** follow the order displayed by the hole transfer rates, although the differences in values between single- and doubly-fluorinated compounds is very small. For μ_{hop}(electron), the values increase as the number of F-atoms increase, again following the trend displayed in the case of k_{hop}(electron). It is clear that **P4-P12** with better charge mobilities are expected to be more efficient in charge extraction.

3.4.7 Conclusions

A detailed DFT study has been carried out to understand the structural, optical, electronic and charge transport properties of a series of BDT-triazole based oligomers, where fluorine atoms are successively introduced into the BDT part. Initial studies are carried out to confirm our use of density functionals for ground states as well as for the excitation calculations. Introduction of electron withdrawing fluorine atoms in oligomers helps in lowering HOMO and LUMO levels. All fluorinated and non-fluorinated tetramers exhibited good light absorption efficiency. It was found that **P4**-**P12** tetramers have better hole and electron mobilities compared to their parent oligomers. Hence, with better charge extraction property, better PCEs are expected with these oligomers.

Chapter 4

Halogenation of the side chains in donor-acceptor based small molecules for photovoltaic applications

In this chapter, structural, optoelectronic, and charge transfer properties of halogenated small molecule donors based molecules are investigated. A part of the content of this chapter is published in *ChemistrySelect*, **2021**, 6, 5254.

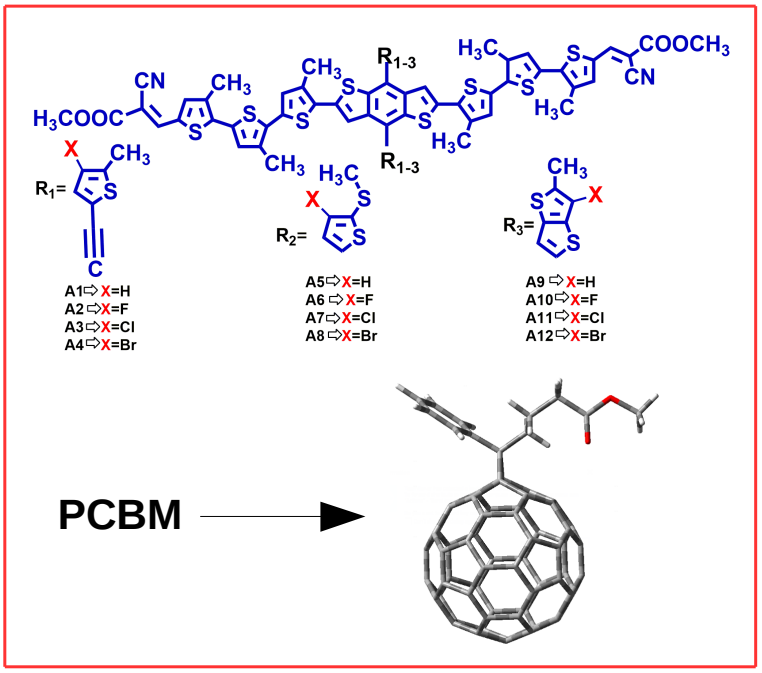

Figure: A-D-A based small molecules, the halogenated SMs, and **PCBM**.

4.1 Introduction

Recently, Chu et al.[35] have reported three A-D-A type small molecules (SMs) based on BDT core with three different lateral flexible side chains: 2-ethynyl-5-octylthiophene (TB), 2-(octylthio)thiophene (TS) and 2-(2-ethylhexyl) thieno[3,2-b]thiophene (TT). In addition, the central BDT unit is symmetrically connected by three octylthiophene units with end-capping by cynoacetate on each side. It was observed that incorporation of π-conjugated lateral side chains affected the optoelectronic properties producing a very high value of V_{oc} of 0.98 V. BHJ devices based on the above three SMs, denoted as **A1**, **A5**, and **A9** in our study, with TB, TS and TT side chains, respectively, produced PCE values of 3.59%, 4.98% and 5.05%. Our group has been interested in understanding the effects of substitutions on the donor units in OPV cells.[92, 148] Keeping in mind that halogen substitution has a large effect on the optoelectronic and photovoltaic properties as discussed in previous paragraph, we have modified **A1**, **A5** and **A9** systems by substituting one hydrogen atom in each of the thiophene rings on the lateral side chains of the BDT donor unit by either two fluorine or two chlorine or two bromine atoms. Hence, each of the above three molecules produce three new molecules and we denote those as **A2**-**A4**, **A6**-**A9**, and **A10**-**A12**, respectively. As a result, three sets of four SMs each are studied in this work. Schematic pictures of the resultant SMs are shown in the Figure 4.1. We would like to mention here that systematic computational studies showing the effect of halogen substitution on the electronic structure and optical properties of D-A blends are scarce and in particular, effects of chlorine and bromine substitutions have not been explored much. Hence, we aim to carry out DFT studies to understand the structural features of the newly designed donors and shed light on photovoltaic properties of the blends of these SMs with **PCBM** acceptor. Although the non-fullerene acceptors have become very prominent in recent times, fullerenes are still used due to their various advantages.[149–151] Use of fullerene acceptor in a device has recently produced a PCE $\sim$ 17%.[151] In the next section, we describe the computational aspects of our studies. This

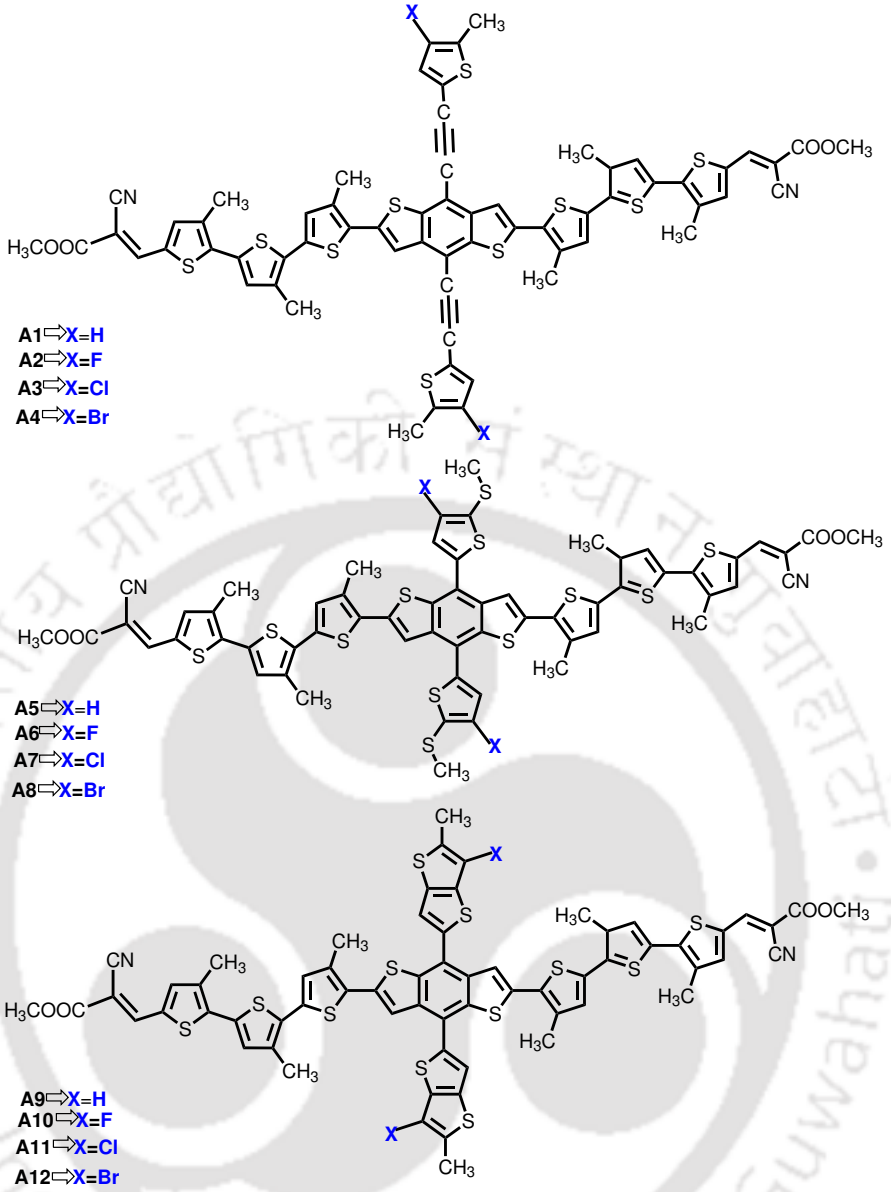

FIGURE 4.1: Molecular structures of the investigated molecules **A1**-**A12**.

is followed by the Results and Discussion section and then, the conclusions in the last section.

4.2 Computational Details

Two separate sets of DFT calculations are performed: one for the SM donors and **PCBM**, and the other one for the SM/**PCBM** blends. Ground state geometry

TABLE 4.1: Energies of HOMOs (E_{HOMO} in eV) and LUMOs (E_{LUMO} in eV) for **A1**, **A5** and **A9** obtained in chloroform solvent using B3LYP, HSE06, and PBE06 functionals and 6-31G(d, p) basis set.

Compounds	B3LYP		HSE06		PBE0		Exp.[35]	
	E_{HOMO}	E_{LUMO}	E_{HOMO}	E_{LUMO}	E_{HOMO}	E_{LUMO}	E_{HOMO}	E_{LUMO}
A1	-4.94	-3.15	-4.77	-2.98	-5.18	-3.38	-5.31	-3.63
A5	-5.02	-3.16	-4.93	-3.07	-5.26	-3.39	-5.40	-3.67
A9	-4.98	-3.16	-4.83	-3.00	-5.22	-3.38	-5.35	-3.64

TABLE 4.2: The calculated first excitation energies (E_{g}^{1} in eV) in chloroform solvent using four different functionals, CAM-B3LYP, PBE06, ωB97XD and B3LYP, with the 6-31(d,p) basis set.

Compounds	CAM-B3LYP	PBE0	ωB97XD	B3LYP	Exp.[35]
	E_{g}^{1}(eV)	E_{g}^{1}(eV)	E_{g}^{1}(eV)	E_{g}^{1}(eV)	E_{g}^{1}(eV)
A1	2.42	1.94	2.52	1.79	1.76
A5	2.45	1.97	2.54	1.86	1.75
A9	2.45	2.00	2.54	1.83	1.78

optimizations of the SM donors are carried out at DFT level using B3LYP, PBE0 and HSE06 global hybrid functionals with 6-31G(d,p) basis set. All these calculations included Grimme's D3 version of dispersion correction. Solvent effect of chloroform was taken into account by employing a C-PCM. Table 4.1 shows that the values of HOMO of **A1**, **A5**, and **A9** at PBE0/6-31G (d,p) level are closer to the corresponding experimental values. Hence, ground state optimizations for all the other SMs are performed at the PBE0/6-31G (d,p) level.

For the twelve SM donors, vertical excitation calculations are performed at TD-DFT level in chloroform solvent using B3LYP, PBE0, CAM-B3LYP and ωB97XD functionals with 6-31G(d,p) basis set. For **A1**, **A5**, and **A9**, the results listed in Table 4.2 show that B3LYP functional produces better E_{g}^{1} compared to the other functionals. Thus, the B3LYP functional is chosen for TD-DFT studies of all newly designed SMs. With energies of HOMO and E_{g}^{1}s at hand, LUMO energies of **A1**-**A12** are calculated as: $E_{\mathrm{LUMO}} = E_{\mathrm{HOMO}} + E_{\mathrm{g}}^{1}$. The LUMO energies are also shown in the Table 4.1. As mentioned in the Introduction, **PCBM** is used as the acceptor in our studies. The structure of **PCBM** is also optimized at PBE0/6-31G(d,p) level. Energy of the LUMO for **PCBM** is again calculated by adding its first excitation energy to the energy of HOMO.

For the donor/acceptor (SMs/**PCBM**) blends, optimized geometries are obtained at the CAM-B3LYP/6-31G(d,p) level. There are various possibilities for donor-acceptor arrangements, e.g. face-on, tip-on, and edge-on structures. However, it has been verified in many cases that face-on arrangement increases the electron coupling and contributes the most to the charge transfer in the donor/acceptor bi-molecular systems.[103, 152–156] Therefore, we have chosen to use face-on models for our systems. In the above optimizations, Grimme's D3 version of dispersion correction was also included. Vertical excitation energies for these blends at the ground state optimized geometries are also calculated at CAM-B3LYP/6-31G(d,p) level. It is to be noted here that excited states with intermolecular charge transfer (ICT) characters play very important roles in photovoltaic device operation. Therefore, CAM-B3LYP functional which includes long-range corrections is used here to deal with those ICT excited states of the blends. All the above mentioned electronic structure calculations are performed using the Gaussian 09 software package. Post processing of the excited state calculations to analyze characters of excited states and charge-transfer lengths are carried out using the Multiwfn[141] software.

4.3 Results and discussion

4.3.1 Donor SMs

4.3.1.1 Molecular geometries in ground state

In the active layer of an OPV device, geometry conformation of a molecule has a large effect on its photo-physical properties which affects the performance of the device. Optimized geometries of all the SMs in ball and stick model are shown in Figures 4.2 and B1-B2 (see Appendix B) . The carbon-carbon single bond lengths of **A1**-**A12** molecules are between 1.41 to 1.44 Å, which are shorter than that of typical carbon-carbon single bond (1.54 Å). Dihedral angles ϕ_1, ϕ_2 and ϕ_3 are marked in Figures 4.2 and B1-B2 and the values are tabulated in Table

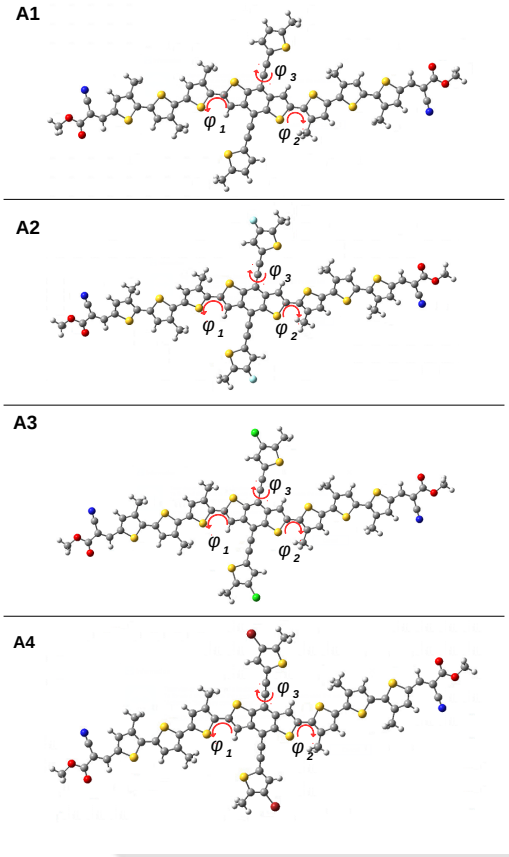

FIGURE 4.2: Optimized ground state geometries for **A1**-**A4** calculated at PBE0/6-31G(d,p) level.

4.3. While ϕ_1 and ϕ_2 are the dihedral angles between the BDT ring and the adjacent thiophene units along the main chain, ϕ_3 represents the angle between the BDT ring and the lateral side chain. Values of ϕ_1 and ϕ_2 for **A1** are 18.5° and 22.6°, respectively. Minor changes in values ϕ_1 and ϕ_2 are observed when the two hydrogen atoms in **A1** are replaced by two halogen atoms resulting in **A2**-**A4**. Similar trends are found in cases of **A5**-**A8** and **A9**-**A12**. This shows that substitutions in the side-chains even by heavy halogens have little effect on the dihedral angles in the main chain. Presence of triple bonds along the side chains of **A1**-**A4** results in planar structures for these systems while keeping the halogen substituted thiophene rings far from the main chain. As shown in the Table 4.3, values of ϕ_3 for **A5**-**A8** and **A9**-**A12** also remain very close to each other even though the substituted thiophene/thienothiophene rings are now directly attached to the main BDT chain.

TABLE 4.3: Selected dihedral angles (ϕ in degree) of the optimized ground-state structures of all **A5-A12**. ϕ_1, ϕ_2 and ϕ_3 are seen in Figures 4.2 and B1-B2

.

Compounds	ϕ_1	ϕ_2	ϕ_3
A5	20.5	24.9	53.7
A6	19.9	24.1	54.4
A7	19.5	23.4	54.9
A8	19.6	23.4	54.9
A9	19.7	26.8	55.3
A10	19.3	24.1	55.8
A11	18.6	23.3	55.8
A12	18.5	23.2	55.9

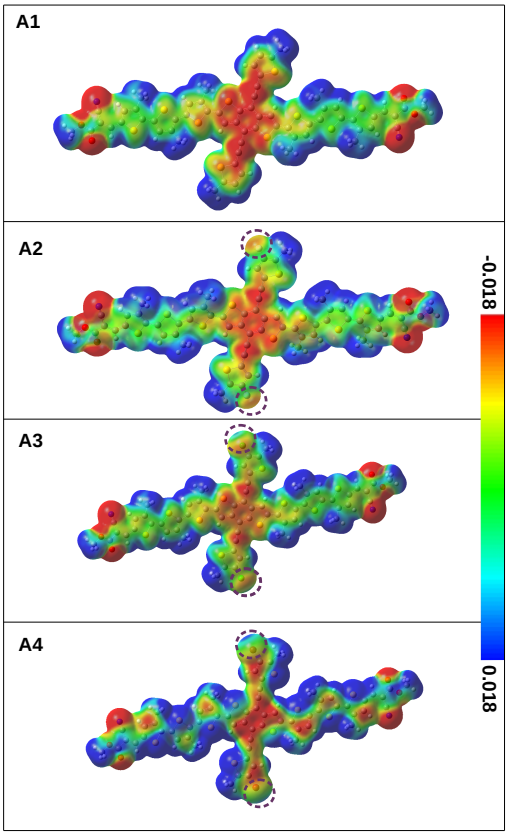

FIGURE 4.3: The molecular electrostatic potentials (ESPs) drawn on isosurfaces of electron density for **A1-A4**. An iso value of 0.001 is used. Brown colored circles indicate the locations of the halogen atoms.

The effect of incorporating different halogen atoms is also examined using electrostatic potential (ESP) maps for the SM donors. The ESP maps are shown in the Figures 4.3 and B3 (see Appendix B). The red color indicates negative ESP

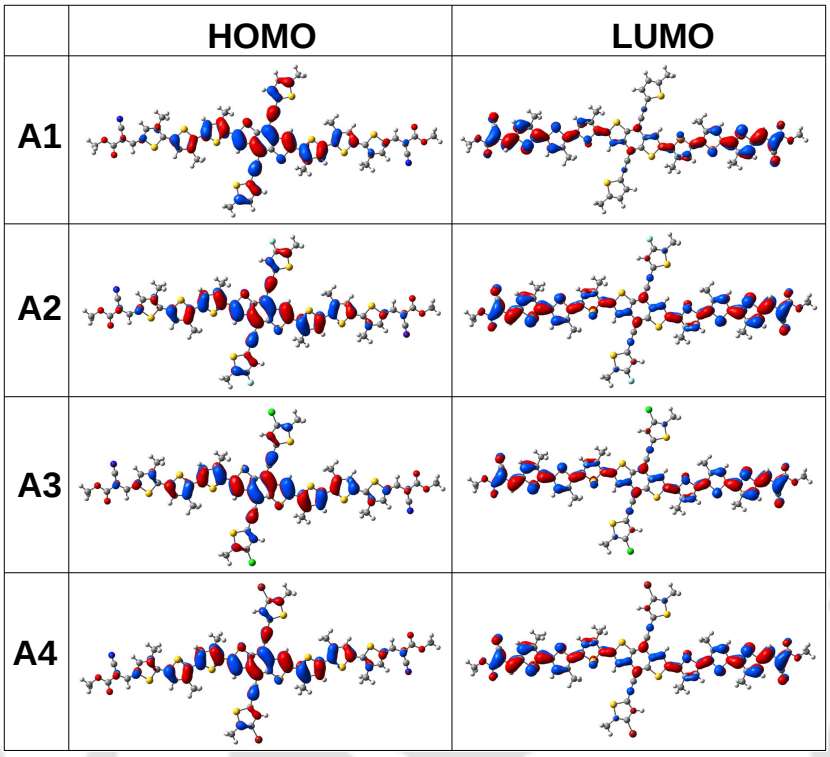

FIGURE 4.4: HOMOs and LUMOs of **A1**-**A4** SMs computed at the PBE0/6-31G(d,p) level in chloroform solvent (isovalue of 0.02 a.u.).

or electron-rich areas, and similarly, the blue color indicates electron-deficient regions. The introduction of halogen atom changes the ESP maps, as shown in these figures. The region around the most electronegative and least polarizable fluorine atom is understandably negative. On the other hand, the regions around chlorine and bromine atoms are comparatively less negative, and the appearances of positive potential regions are observed. This shows the presence of σ-holes along the C-X axes for chlorine and bromine substituted systems.

4.3.1.2 Frontier molecular orbitals, open-circuit voltages and energy losses

Plots of HOMOs and LUMOs for **A1**-**A12** are shown in Figures 4.4 and B4-B5 (see Appendix B). As Figure 4.4 shows, HOMOs are mainly distributed over the donor BDT units and the adjacent thiophene rings. On the other hand, LUMOs of these SMs are mainly over the acceptor cyanoacetate units and thiophene units.

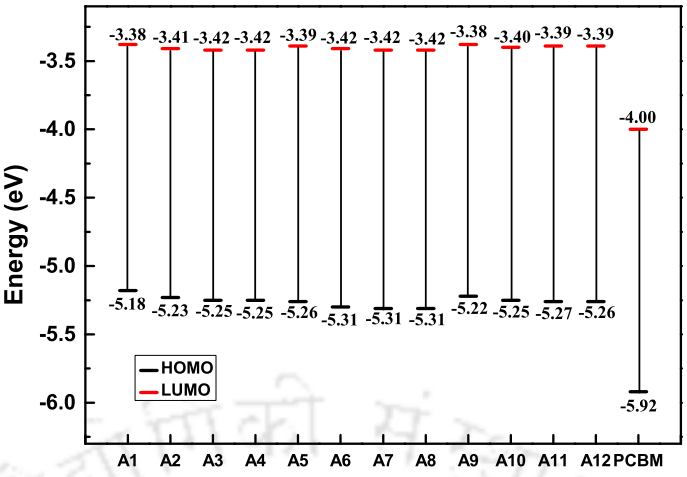

FIGURE 4.5: Calculated HOMO and LUMO energy levels of SMs. These results are obtained at PBE0/6-31G(d,p) level in chloroform solvent.

As shown in Figures B4-B5, similar distributions are observed in the cases of **A5**-**A8** and **A9**-**A12** SMs. This shows that halogen substitution in the lateral side chains has little effect on the electron density distribution of the SMs.

A basic requirement for efficient OSC devices is the matching HOMO/LUMO levels of the donors with those of the acceptor. Energies of HOMOs (E_{HOMO}) and LUMOs (E_{LUMO}) determine physical parameters such as V_{oc} and ΔE_{LL}. The calculated E_{HOMO} and E_{LUMO} values of **A1**-**A12** are shown in Figure 4.5. It is to note that the order of the HOMO energies of **A1**, **A5** and **A9** matches with the experimental results.[35] Better electron-accepting character of thio-substituted side thiophene rings results in the lowest E_{HOMO} for **A5**. Halogen atoms have a crucial effect on the energies of HOMOs and LUMOs of the SMs. Compared to **A1**, **A2**, **A3** and **A4** show lower HOMO and LUMO values because of the electron-withdrawing nature of the halogens. Similar trends are observed in cases of **A5**-**A8** and **A9**-**A12**. It is to be noted that chlorine and bromine substituted SMs have the same E_{HOMO}s and these energies are slightly smaller than the fluorinated SMs as chlorine and bromine atoms with unoccupied $3d$ and $4d$ orbitals can accept the delocalized the π-electrons.[157, 158]

As displayed in Table 4.4, the calculated V_{oc} values of **A1**, **A5**, and **A9** are in good agreement with the experimental results. V_{oc} values of all the SMs are in the

TABLE 4.4: Open circuit voltages (V_{oc} in volt) and driving force (ΔE_{LL} in eV) for the twelve SM donors. energies are in eV. Experimental V_{oc} values are 0.85, 0.96 and 0.97 V for **A1**, **A5** and **A9**, respectively.

Donors	**A1**	**A2**	**A3**	**A4**	**A5**	**A6**	**A7**	**A8**	**A9**	**A10**	**A11**	**A12**
V_{oc}	0.88	0.93	0.95	0.95	0.96	1.01	1.01	1.01	0.92	0.95	0.97	0.96
ΔE_{LL}	0.62	0.59	0.58	0.58	0.61	0.58	0.58	0.58	0.62	0.60	0.61	0.61

range 0.88 V to 1.01 V. In the case of **A1**-**A4**, it is observed that substitutions of the thienyl hydrogen atoms by fluorine atoms result in an increase in V_{oc} by 0.05 V. But chlorine and bromine substitutions increase the V_{oc} value by 0.07 V each. Results for **A5**-**A8** and **A9**-**A12** sets are similar to the first set, i.e. halogenated SMs have larger V_{oc}s. While the V_{oc} values of **A6**-**A8** are the same, the values for the three halogenated SMs in the third set differ slightly from each other and this is similar to the results of the first set. It is also clear that V_{oc} values of **A6**-**A8** are the largest among the twelve SMs. Hence, the newly designed SMs with deeper HOMO values and higher V_{oc} values, are more suitable for OSCs devices. The calculated HOMO and LUMO energies of **PCBM** are also shown in Figure 4.5. ΔE_{LL} values, the energy difference between the LUMO energy of the donor and **PCBM**, are shown in Table 4.4. All ΔE_{LL} values of all SMs have larger than 0.3 eV and this ensures an efficient electron separation at the donor/acceptor interface.

Minimizing photon energy losses (E_{loss}) is important to optimize PCEs. Typical E_{loss} values for inorganic or perovskite solar cells are between 0.3-0.6 eV[159] while the values are 0.7-1.0 eV for OSCs.[160, 161] E_{loss} is defined as[162–164]: E_{loss}= E_g^1- eV_{oc}, where E_g^1 is the first excitation energy of the donor system. Hence to have a smaller E_{loss}, smaller E_g^1 and larger V_{oc} values are required. Calculated E_{loss} values are also plotted in Figure 4.6. E_{loss} values of **A1**-**A12** are in the range of 0.88 - 0.92 eV which are within the reported values.[160, 161] As shown in Figure 4.6, halogen substituted SMs have slightly smaller E_{loss} values than the parent SMs. In addition, it is also observed that the values of E_{loss} for halogen substituted SMs are close to each other and that chlorine and bromine substituted SMs have exactly the same E_{loss} values.

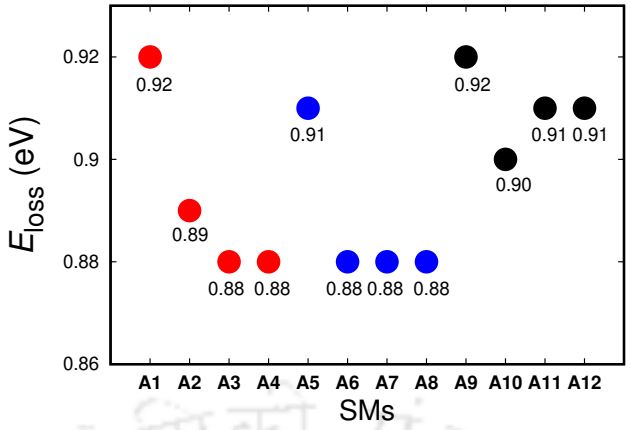

FIGURE 4.6: Energy losses (E_{loss}) of **A1-A12** systems. Three sets of SMs, corresponding to **A1-A4**, **A5-A8** and **A9-A12**, are marked in three different colors, red, blue and black, respectively.

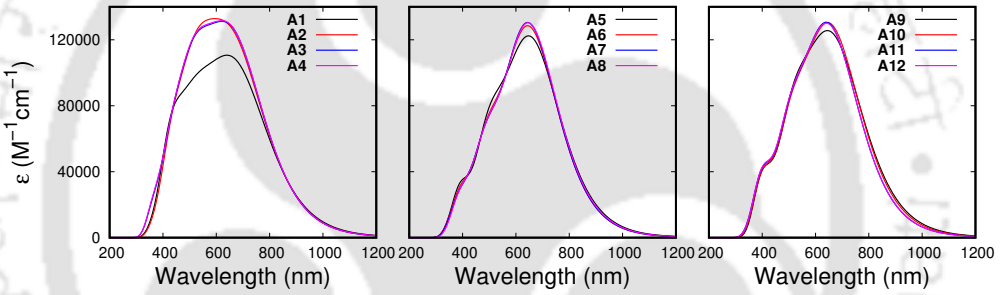

FIGURE 4.7: Simulated absorption spectra of all **A1-A12** SMs in chloroform solvent. A full width at half-maximum value of 2500 cm^{-1} is used.

4.3.1.3 Light absorption properties

One of the most important aspects in OSCs is to increase intake of photons which results in improving the J_{sc}. For this, absorption spectra of the donor should match with the solar spectrum so that more solar energy is utilized. Below we discuss absorption spectra of all the molecules.

Simulated absorption spectra are presented in Figure 4.7. Corresponding E_{g}^{1} s (and λ_{max} s), percentage contributions of HOMO $\rightarrow$ LUMO transitions, f_{osc} s, and η s of **A1-A12** SMs are tabulated in Table 4.5. Figure 4.7 shows that absorption spectra for halogenated SMs remain very similar to spectra of parent

TABLE 4.5: First excitation energies (E_g^1 in eV), maximum absorption wavelength (λ_{max} in nm), % contributions of H→L transitions (denoted as $C_{H\rightarrow L}$), oscillator strengths (f_{osc}) and light absorption efficiency (η) data obtained at TD-B3LYP/6-31G(d,p) level, for all **A1**-**A12** SMs. Experimental E_g^1 values are 1.76, 1.75 and 1.78 eV for **A1**, **A5** and **A9**, respectively.

Compounds	E_g^1, λ_{max}	$C_{H\rightarrow L}$	f_{osc}	η
A1	1.79, 690	95	2.05	0.99
A2	1.81, 681	95	2.30	0.99
A3	1.82, 678	95	2.44	0.99
A4	1.82, 678	95	2.44	0.99
A5	1.86, 664	95	2.60	0.99
A6	1.88, 656	95	2.78	0.99
A7	1.89, 655	94	2.83	0.99
A8	1.89, 655	94	2.83	0.99
A9	1.83, 675	95	2.49	0.99
A10	1.85, 668	94	2.65	0.99
A11	1.87, 662	94	2.66	0.99
A12	1.87, 662	94	2.66	0.99

systems. But absorption intensities of the halogenated systems are larger in comparison to the parent systems. Quantitative comparisons in Table 4.5 indicate that computed E_g^1 values of parent molecules are 1.79, 1.86, and 1.83 eV, respectively showing good match with the experimental values.[35] Table 4.5 also shows that λ_{max} peaks of **A1**-**A12** originate from $S_0\rightarrow S_1$ transitions and these $S_0\rightarrow S_1$ transitions are contributed mostly by HOMO→LUMO excitations. f_{osc} values for these transitions are very large and it is observed that f_{osc} values increase with an increase in the size of halogen atoms. It is also observed that the absorption peaks for halogenated SMs are slightly blue shifted compared to the parent spectra, in accordance with recent studies.[165] Values of η are calculated by considering the $S_0\rightarrow S_1$ transitions in all the cases. Table 4.5 shows that all SMs have good light absorption efficiencies.

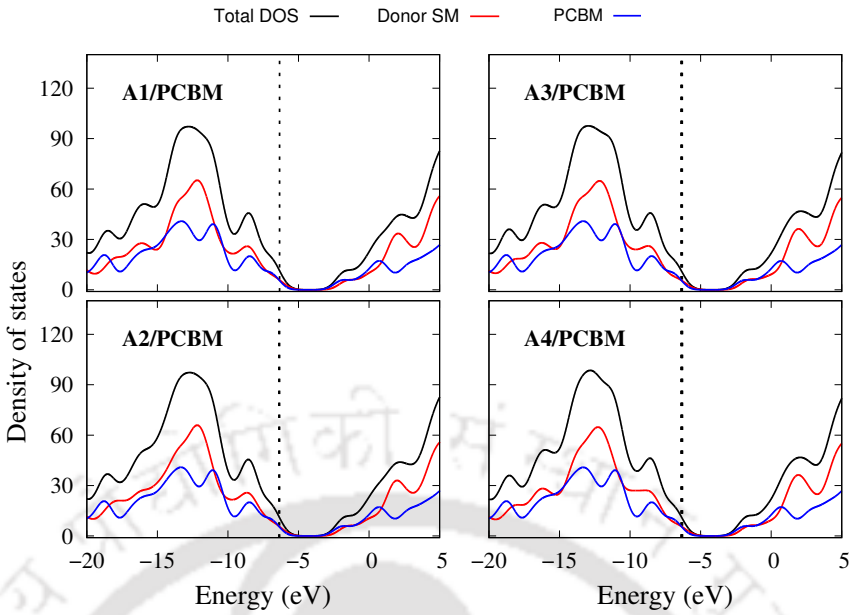

FIGURE 4.8: TDOS, and PDOS from fragments SM donor and **PCBM** acceptor for **A1-A4/PCBM**.

4.3.2 A1-A12/PCBM composite systems

4.3.2.1 Structures and properties

Important processes like charge-separation and recombination occur at donor-acceptor interfaces and therefore, understanding the interactions and energetics at the interfaces arising out of the halogen substitutions can provide a better idea about the performance of the systems. To study the interfacial geometries, full geometry optimizations are carried out for all the donor-acceptor blends in which initial structures have the **PCBM** molecule vertically above the SM unit in face-on fashions. Optimized structures of composite systems of **A1-A12/PCBM** are shown in Figures B6-B8 (see Appendix B). Optimized stacking distances between **A1-A12** and **PCBM** are found to be in the range of 3.5 to 4.0 Å, in accordance with typical D-A distances.[166, 167]

TDOS for halogenated interfaces are compared against the TDOS of the parent system in Figure B9 (see Appendix B). As observed, TDOSs of halogenated complexes and that of parent systems are almost the same showing very minor

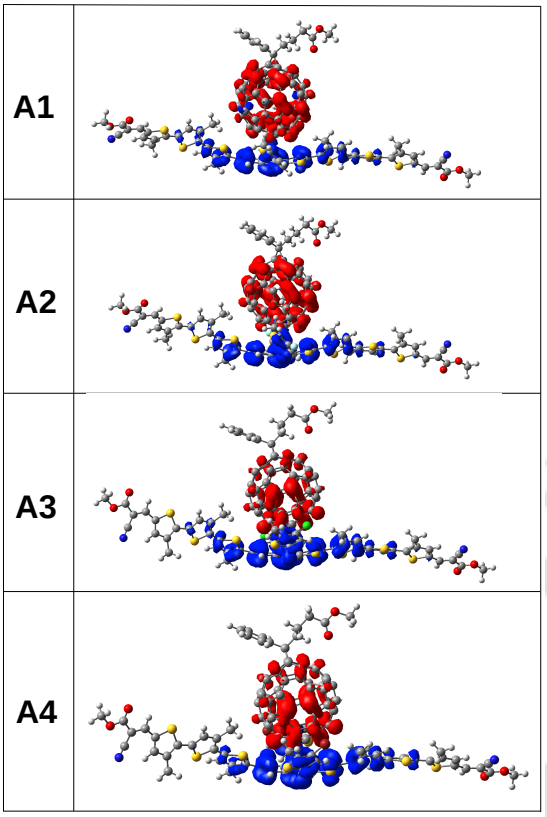

FIGURE 4.9: Charge density difference (CDD) maps for the S_{15}, S_{16}, S_{12}, and S_{12} states of the **A1**, **A2**, **A3** and **A4** composite systems, respectively. These are first ICT states for these four composites. Red and blue colors represent electrons and holes, respectively.

differences. To find the percentage contribution of fragments to TDOS, PDOS are calculated by dividing the interfaces into two fragments: fragment 1 consists of the donor SMs and fragment 2 of the **PCBM**. The results are shown in Figures 4.8. Around the Fermi level, both fragments contribute similarly to TDOS. But between -10 to -5 eV, and 0 to 5 eV, contributions of donor SMs are much larger than the **PCBM**. Similar situations are observed for other two sets as shown in Figures B10- B11 (see Appendix B).

Results of TDDFT studies and analysis of the results by Multiwfn software are shown in the Table 4.6. In particular, excitation energies of first ICT states, corresponding f_{osc}s, charge transfer lengths (l^{CT}) of the twelve composites are tabulated. ICT states are identified by looking at the charge density difference (CDD) plots with holes localized on donor SMs and electrons localized on the

TABLE 4.6: Excitation energies ($E^{\mathrm{ICT}}_{\mathrm{g,blend}}$) of the first intermolecular charge transfer (ICT) states in the blends, corresponding oscillator strengths (f_{osc}) and charge transfer lengths (l^{CT}) for the first ICT excited states of **A1-A12/PCBM** systems.

Compounds	ICT state	$E^{\mathrm{ICT}}_{\mathrm{g,blend}}$	f_{osc}	l^{CT}(Å)
A1/PCBM	S_{15}	3.07	0.028	3.62
A2/PCBM	S_{16}	3.10	0.073	5.20
A3/PCBM	S_{12}	2.97	0.223	5.09
A4/PCBM	S_{12}	2.96	0.225	5.13
A5/PCBM	S_{16}	3.10	0.001	4.52
A6/PCBM	S_{19}	3.22	0.005	5.84
A7/PCBM	S_{19}	3.23	0.006	5.77
A8/PCBM	S_{15}	3.10	0.009	5.87
A9/PCBM	S_{17}	3.09	0.004	4.98
A10/PCBM	S_{17}	3.14	0.005	5.20
A11/PCBM	S_{17}	3.15	0.005	5.16
A12/PCBM	S_{17}	3.15	0.005	5.19

PCBM acceptor. CDD plots for **A1-A4/PCBM**, **A5-A8/PCBM** and **A9-A12/PCBM** are shown in Figures 4.9, B12 and B13, respectively (see Appendix B). As shown in Figure 4.9, S_{15}, S_{16}, S_{12}, and S_{12} states are the first ICT states for **A1-A4/PCBM** composites. The corresponding excitation energies are 3.07 eV, 3.10 eV, 2.97 eV, 2.96 eV, respectively. Table 4.6 also shows that the f_{osc}s for the first ICT states of the halogenated composites are comparatively larger than the parent composites. l^{CT} is defined as the distance between centroids of hole and electron during electron excitation.[168, 169] From the Table 4.6, values of l^{CT} for **A1-A4/PCBM** are 3.62 Å, 5.20 Å, 5.09 Å, and 5.13 Å, respectively. It is observed that l^{CT} values for halogenated SMs are larger compared to that of parent SM. Larger l^{CT} values of fluorine, chlorine and bromine substituted SMs indicate easier separation of the exciton in halogenated cases. Similar observations are obtained for **A5-A8/PCBM** and **A9-A12/PCBM** systems.

IPs, EAs, first excitation energies of SM-**PCBM** blends ($E^{1}_{\mathrm{g,Blend}}$) and E_{b} are listed in Table 4.7. E_{b} is one of the key parameters in OPVs and is directly related to the charge separation. It originates from the Coulombic interaction between the electron-hole pair, and this energy needs to be overcome for efficient

TABLE 4.7: Calculated ionization potentials (IP in eV) and electron affinities (EA in eV), interfacial lowest excitation energies ($E^1_{g,Blend}$ in eV) and exciton binding energies (E_b in eV) for all **A1-A12/PCBM** systems.

Compounds	IP	EA	$E^1_{g,Blend}$	E_b
A1/PCBM	5.67	2.69	2.47	0.51
A2/PCBM	5.74	2.71	2.47	0.56
A3/PCBM	5.72	2.70	2.47	0.56
A4/PCBM	5.73	2.69	2.47	0.57
A5/PCBM	5.68	2.72	2.46	0.50
A6/PCBM	5.71	2.73	2.47	0.51
A7/PCBM	5.71	2.73	2.47	0.51
A8/PCBM	5.71	2.74	2.47	0.50
A9/PCBM	5.71	2.74	2.46	0.51
A10/PCBM	5.79	2.76	2.46	0.57
A11/PCBM	5.80	2.76	2.46	0.58
A12/PCBM	5.80	2.76	2.46	0.57

charge-separation. Theoretically, E_b is defined as the difference between the fundamental and optical bandgaps.[104, 105] While fundamental gap corresponds to the difference between the IP and EA, optical gap is $E^1_{g,Blend}$. A smaller E_b value is beneficial for the separation of electron and hole. The calculated values of E_b for **A1-A12/PCBM** are in the range of 0.51-0.58 eV, in good agreement with typical experimental values.[105] As the Table shows, the values of E_b for **A2-A4/PCBM** SMs are slightly larger compared to the value for parent molecule. Similar trend is obtained for **A9-A12/PCBM** set. But in the case of **A5-A8/PCBM**, E_b values are very close to each other. Since the $E^1_{g,Blend}$ values of the blends are almost the same, the difference in the E_b values arise from the IP values as shown in the Table 4.7. In addition, it is also observed that halogenated systems in each set have very similar E_b values. Hence, exciton dissociation in halogenated blends will be as difficult/easy as in the parent blends.

4.3.2.2 Intermolecular charge transfer and charge recombination rates

Exciton dissociation is a charge-separation process from the locally excited SM ***/PCBM** state to the charge transfer SM$^+$**/PCBM**$^-$ state. Similarly, the charge

recombination process is a transformation from the $SM^+/\mathbf{PCBM}^-$ state to the ground state of the SM/**PCBM** composite. Therefore, faster charge transfer (k_{CT}) and slower charge recombination rates (k_{CR}) are required for better performance of a solar cell device. It is worth mentioning here that the Marcus equation is derived from the Fermi's golden rule using the assumption that $k_BT >> \hbar\omega$, i.e. in high-temperature, and weak coupling limits. Therefore, the theory does not take tunneling effects into account which is very important in low-temperature regime. The inclusion of quantum effects results in Marcus-Levich-Jortner theory.[170–172] Nevertheless, the classical Marcus theory is frequently used to compute the charge transfer rates in OPVs[173–177] and it has been shown to work well. Keeping this in mind, we have chosen to use the Marcus formula for our rate calculations. As shown in Eq. 2.41, these rates depend on λ, V_{DA}, and ΔG. Values of all these parameters are displayed in Table 4.8. As mentioned already, λ is the reorganization energy arising out of the geometry modifications occurring during charge gain or loss processes. It is worth mentioning here that λ values for CT and CR processes are usually calculated separately using either average of reorganization energies of reactant/product CT states or reactant/product CR states.[178–180] In our case, on the other hand, a single value for λ is used for both CT and CR processes, and this procedure has worked well for other systems, as shown in the literature.[91, 181, 182] λ values of **A1-A12/PCBM** systems are in the range of 0.50-0.53 eV and hence, λs for parent SMs and halogen substituted SMs are very close to each other.

V_{DA}, the electronic coupling between donor and acceptor describing the strength of the interaction between the initial and final charge-localized states, is key to determining the rates of charge transfer and charge recombination. It has been highlighted in the literature that electronic couplings are sensitive to the choice of density functionals, and usually, range-separated functionals perform better than the global hybrid functionals.[183, 184] Calculated μ_{trans}, $\Delta\mu$, and V_{DA} values of **A1-A12/PCBM** are tabulated in Table 4.8. The evolution of V_{DA} in each set showing that halogen substituted SMs have larger V_{DA} values than the parent SM indicates a clear effect of halogen substitution. $|V_{DA}|$ values for **A1-A4/PCBM**

TABLE 4.8: Calculated parameters for computing the rates of charge-transfer and charge-recombination for all the twelve systems. Transition dipole moments (μ_{trans}), and differences in dipole moments between the ground and the charge-transfer excited states ($\Delta\mu$) are in atomic units. Total reorganization energy (λ), Gibbs free energy change for charge-transfer (ΔG_{CT}) and charge-recombination (ΔG_{CR}), and charge-transfer integral (V_{DA}) are in eV. Charge transfer and charge recombination rates k_{CT} and k_{CR} are in s^{-1}.

Compounds	μ_{trans}	$\Delta\mu$	V_{DA}	ΔG_{CT}	ΔG_{CR}	λ	k_{CT}	k_{CR}
A1/PCBM	-0.188	-2.27	-0.25	-0.43	-1.88	0.50	1.33×10^{15}	1.08×10^{-1}
A2/PCBM	-0.188	-1.48	-0.38	-0.45	-1.93	0.51	3.22×10^{15}	3.78×10^{-2}
A3/PCBM	0.272	-0.68	0.93	-0.43	-1.95	0.51	1.81×10^{16}	1.25×10^{-2}
A4/PCBM	0.168	-1.33	0.36	-0.44	-1.95	0.51	2.78×10^{15}	1.91×10^{-2}
A5/PCBM	0.064	2.12	0.09	-0.42	-1.95	0.53	1.61×10^{14}	1.14×10^{-2}
A6/PCBM	-0.145	4.21	-0.11	-0.40	-2.00	0.52	2.18×10^{14}	9.25×10^{-4}
A7/PCBM	-0.200	4.43	-0.15	-0.40	-2.00	0.52	3.67×10^{14}	1.13×10^{-3}
A8/PCBM	-0.115	3.36	-0.11	-0.39	-2.00	0.52	1.90×10^{14}	7.25×10^{-4}
A9/PCBM	0.03	4.23	0.02	-0.44	-1.91	0.52	1.01×10^{13}	3.69×10^{-3}
A10/PCBM	0.022	2.03	-0.03	-0.48	-1.94	0.52	2.65×10^{13}	1.62×10^{-3}
A11/PCBM	-0.018	1.27	-0.04	-0.5	-1.95	0.53	4.57×10^{13}	3.61×10^{-3}
A12/PCBM	-0.016	1.64	-0.03	-0.49	-1.95	0.53	2.28×10^{13}	2.17×10^{-3}

are 0.25 eV, 0.38 eV, 0.93 eV, 0.36 eV, respectively, and this shows that chlorine substituted SM has the largest $|V_{DA}|$ value in the set. Same trend is followed in **A5-A8/PCBM** and **A9-A12/PCBM** sets.

ΔG_{CT} is the driving force for charge separation at the SM/**PCBM** interfaces. Negative values of ΔG_{CT} in Table 4.8 indicate thermodynamically feasible electron transfer processes in all the systems. It is also observed that the values of $|\Delta G_{CT}|$ for all the four systems in **A1-A4** and **A5-A8** sets remain similar to each other. But in the case of **A10-A12/PCBM**, $|\Delta G_{CT}|$ values are little larger than the value in **A9/PCBM**. Eq. 2.41 shows that k is dependent on two factors; $|V_{DA}|$ and $|\Delta G+ \lambda|$. k increases as the absolute value of sum of ΔG and λ becomes smaller. In addition, k is also directly proportional to $|V_{DA}|$. k_{CT} values of **A1-A12/PCBM** are listed in Table 4.8. k_{CT} value increases from **A1/PCBM** to **A3/PCBM** and then decreases for **A4/PCBM**, in accordance with the V_{DA} values. Similar results are obtained for the other two sets of blends. Therefore, halogen substituted blends always have larger charge-transfer rates than the parent systems. In addition, chlorine substituted complexes have largest k_{CT} values which

is mainly caused by larger V_{DA} values of **A3**, **A7** and **A11**. As mentioned already, ΔG_{CR} was calculated as the difference between the adiabatic ionization potential of the donor and adiabatic electron affinity of the **PCBM**. As shown in Table 4.8, the calculated values of $|\Delta G_{CR}|$ for halogenated systems are slightly larger than the corresponding parent systems. In addition, the values for the halogenated systems remain very close to each other in a particular set. k_{CR} values in the first two sets, **A1**-**A4** and **A5**-**A8**, follow a similar trend. For these two, k_{CR} values for the halogenated blends are always one/two order smaller than the parent systems. In contrast, **A10**-**A12** blends show slightly smaller recombination rates than that of **A9**/**PCBM**. In all the three sets, fluorine substituted blends show the smallest k_{CR} values. Looking at the above k_{CT} and k_{CR} values, it can be concluded that halogen substituted SMs are better suited than the parent SMs for OPV cells.

We would like to note here that performance of a BHJ device is greatly influenced by blend morphology at the interface,[185–187] in addition to molecular architecture which is considered in our present study. While wave function or DFT based computational molecular design is important since it provides information about energy levels, morphology of the active layer is of utmost importance as has been shown in many studies.[185–188] It has been highlighted that better device performance upon halogenation may not be due to energetics alone, rather it is morphology dependent.[152, 155, 156] Experimentally controlling the blend morphology at the interface has been a difficult task. Computational modeling of the interface morphology is even a bigger challenge. Multi-scale simulations, combining quantum and classical simulations, provide better ideas about blend morphology and its effect on the interfacial processes. We aim to take our present molecular level designing studies further to shed light on the blend architecture and its effect on the OPV performance in near future.

4.4 Conclusions and outlook

In summary, we systematically investigated the effects of substitutions of fluorine, chlorine, and bromine atoms in lateral side chains of BDT based three A-D-A systems. These three A-D-A systems differ by having three different lateral side chains. Hence, nine new halogenated small molecules are designed based on three reported SMs. To explore variations in physical and optoelectronic properties, HOMO and LUMO energies, absorption spectra, and charge transfer properties of these donor/**PCBM** blends are studied using DFT/TD-DFT calculations. There is little effect of incorporation of halogens, both small and large, on the geometries of the donors as the substitutions happen only in the side-chain thiophenes. Halogen substituted SMs are found to possess deeper HOMO values compared to the parent systems, and this results in larger V_{oc} values for the halogenated SMs. All **A1**-**A12** exhibit excellent light absorption properties. Calculated E_{loss} values demonstrate that fluorinated, chlorinated, and brominated SMs have smaller E_{loss} values compared to the parent SMs.

Charge transfer and charge recombination rates are calculated using the Marcus equation. Halogen substituted SMs are found to have relatively larger k_{CT} and smaller k_{CR} values than the parent molecules. Therefore, these halogenated SMs are more suitable for OPV fabrication than the parent systems.

Chapter 5

Effects of π bridge units on the properties of donor-π-acceptor type benzodithiophene-thienothiophene based oligomers

---

In this chapter, structural, optoelectronic, and charge transfer properties of donor-π-acceptor type benzodithiophene-thienothiophene based alternating oligomers are investigated. A part of the content of this chapter is published in *Chemical Physics Letters*, **2020**, 756, 137810.

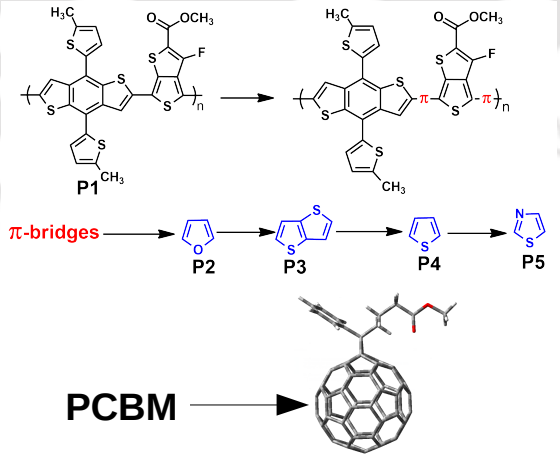

Figure: π-bridge-based alternating conjugated donor-acceptor systems and **PCBM**.

5.1 Introduction

In recent years, there are many reports in which added π bridges between donor and acceptor units have resulted in increased PCEs.[189–193] Introduction of π bridges affects the structure, conjugation pattern and length of the polymer donor resulting in modified photophysical properties. D-π-A polymers based on the donor BDTT, π bridge thiophene, and acceptor benzothiadiazole (BT) have been shown to produce devices with PCE value over 2%.[194] In 2012, Guo et al.[195] reported a device with an active layer consisting of donor BDTT, π bridges thienothiophene and acceptor benzothiadiazole based polymer which showed a PCE value of ∼6.03%. A device based on donor BDTT, π bridges thienothiophene and acceptor benzoxadiazole polymer[196] was found to have a PCE of 7.05%. Lu et al.[197] synthesized a polymer which contained donor BDTT, π bridges thiophene and alkyl thiophene, and acceptor alkylthieno[3,4-c] pyrrole-4,6-dione (TPD) units with the highest PCE of 6.08%. In 2012, Hou and coworkers'[198] device based on donor BDTT, π bridge thiophene and acceptor thieno[3,4-b] thiophene showed a PCE value of ∼7.5%. In 2013, Chang and coworkers[199] developed polymers based on BDTT, π bridges furan, thiophene and selenophene, and acceptor diketopyrrolopyrrole (DPP) units. The resulting devices produced PCEs ∼ 4.7%, 6.5% and 7.2%, respectively. In 2015, Liu et al. designed a device with BDTT, π bridge thienothiophene (TT), and acceptor TPD, and reported a PCE 7.71%.[200] Zhong and coworkers[201] reported a device based on polydithieno-benzodithiophene, π bridge thiophene and acceptor perylene-bisimide units which showed a PCE of 8.4% in 2016. You et al. have reported OSCs based on BDTT donor, π bridge thiophene and acceptors such as fluorinated benzotriazole (FTAZ) and pyridine-fused triazole (m-PyCNTAZ). In this case, PCEs over 7%[1, 2] have been obtained. BDTT-free phthalimide-based polymers have been reported to achieve PCEs ∼ 13.3%.[190]

As the above discussion shows, introduction of π bridge affects the photovoltaic performance of the OSCs. Keeping this in mind and to explore the effect of insertion of π bridges into the conjugated backbone of a donor polymer,

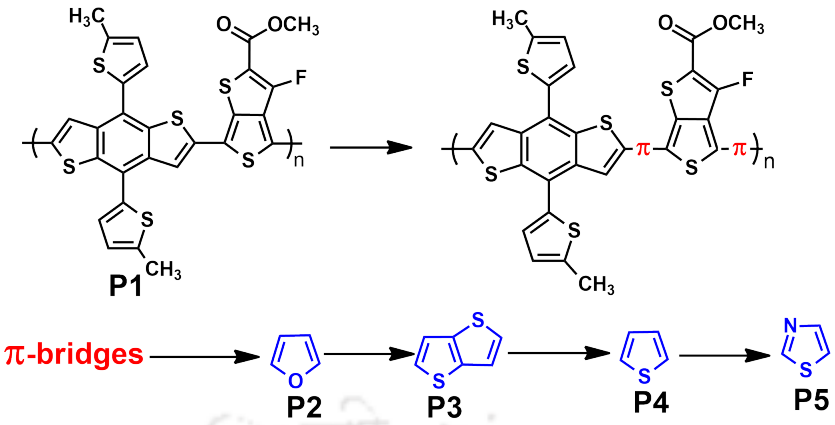

FIGURE 5.1: Molecular structures of **P1**-**P5** repeating units, where n=1-4. **P2**-**P5** are obtained by incorporation of four different π-bridges, as shown, between donor and acceptor units.

we have chosen poly [4,8-bis(5-(2-ethylhexyl) thiophen-2-yl) benzo[1,2-b:4,5-b'] dithiophene-alt-3-fluorothieno[3,4-b]thiophene-2-carboxylate] (P(BDTT-*alt*-TT-F)) (denoted as **P1**)[202] polymer which contains the donor BDTT and acceptor fluorothieno-thiophene-2-carboxylate (TT-F) units and modified the parent system by incorporation of different types of π bridges. For **P1**, a PCE value of 6.47% has been obtained. In our study, four π bridge units furan, thienothiophene, thiophene, and thiazole are introduced between the BDTT and TT-F units. This results in four new D-π-A systems, **P2**, **P3**, **P4**, and **P5**, respectively. Single units of these designed D-π-A oligomers are shown in Figure 5.1. Using computational studies based on density functional theory methods, we aim to have a detailed insight into the effect of the π bridge units on the structures of these donors, and photovoltaic properties of OSCs. Following geometry optimizations, absorption spectra and V_{oc} values are calculated. As highlighted before, **PCBM** and modified **PCBM** are still widely used as acceptors. In addition, the Ref.[202] also used a fullerene derivative as an acceptor. Hence we have used **PCBM** in the present study. This is followed by geometry optimizations of the oligomer-**PCBM** blends. Later, charge transfer properties at donor/acceptor interface are computed by employing the Marcus theory[203] for analyzing the k_{CT} and k_{CR} rates. We conclude our findings of work in the Conclusion section.

TABLE 5.1: Energies of the highest occupied molecular orbital (HOMO) and lowest unoccupied molecular orbital (LUMO) for $(\mathbf{P1})_4$ obtained in chloroform solvent using B3LYP, PBE0, and HSE06 functionals, and 6-311G(d,p) basis set. LUMO values are obtained by adding the first excitation energy (E_g^1) to the HOMO energy. All the energies are in eV.

P1	B3LYP	PBE0	HSE06	Exp.[202]
E_{HOMO}	-5.20	-5.36	-5.00	-5.24
E_{LUMO}	-3.47	-3.63	-3.27	-3.66

5.2 Computational Methodologies

Ground state geometries of all the donor oligomers are optimized at the DFT level with different hybrid functionals such as B3LYP, PBE0, and HSE06 using the 6-311G(d,p) basis set. Experimental studies in Ref.[202] used the chloroform solvent. In our calculations, solvent effect of chloroform (with dielectric constant 4.711) is taken into account by employing the conductor-like polarizable continuum model of solvation (CPCM).[204] We have considered oligomer chain lengths up to n=4. From now onwards, we will denote $(\mathbf{P1})_4$ as **P1** only. Similarly, other tetramers will be denoted as **P2**-**P5** only. As reported in Table 5.1, the calculated HOMO value of **P1** at PBE0/6-311G(d,p) level is in good agreement with the experimental value and hence, PBE0 functional is chosen for describing the ground-state properties of the **P2**-**P5** oligomers and the method is denoted as CPCM-PBE0/6-311G(d,p). Adiabatic electron affinities and ionization potentials of tetramers are calculated at PBE0/6-311G(d,p) level based on neutral, and anion/cation optimized geometries. It is to be noted that anion and cation geometries are optimized at the same level of theory.

Using the ground state optimized geometries, excitation energies and absorption spectra are calculated by the TD-DFT method with various functionals such as CAM-B3LYP, HSE06, and PBE0, and using the 6-311G(d,p) basis set. As shown in Table 5.2, the value of λ_{max} obtained for **P1** using HSE06/6-311G(d,p)

TABLE 5.2: Calculated maximum absorption wavelengths (λ_{max} in nm), first excitation energies (E_g^1 in eV) and oscillator strengths (f_{osc}) of **P1** tetramer in chloroform solvent using three different hybrid functionals with the 6-311G(d,p) basis set on the basis of the ground-state optimized structure at the CPCM-PBE0/6-311G(d,p) level.

P1	λ_{max}	${E_g}^1$	f_{osc}	Exp.[202]
CAM-B3LYP	529	2.34	3.63	703
PBE0	650	1.90	3.04	
HSE06	716	1.73	2.40	

method compares very well with the experimental result. Hence, the optical properties of all five molecules are calculated at HSE06/6-311G(d,p) level and we denote the method as TD-CPCM-HSE06/6-311G(d,p). The LUMO levels of the oligomers are calculated as $E_{LUMO} = E_{HOMO} + {E_g}^1$. As observed in the Table 5.1, the resultant value with PBE0 functional for **P1** matches well with the experimental value. All these calculations are carried out using the Gaussian 09 software packages.

To model the interfaces, blends of tetramers of the donors with **PCBM** are prepared by having the **PCBM** molecule vertically above the donor tetramers at a distance of ~ 3.5 Å. Since these blend systems are very large, the PBE functional is chosen for the optimization. The computational efficiency of these optimization calculations is further improved by using the resolution of identity (RI) method for electron repulsion integrals. In addition, van der Waals interactions are taken into account by Grimme's empirical dispersion correction scheme (denoted as D3)[64] All these calculations are carried out with the def2-SV(P) basis set using the TURBOMOLE V7.1 software.[147] We denote the above method as RI-PBE-D3/def2-SV(P). Following geometry optimizations, single point calculations are performed at M06-2X/6-311G(d,p) level in chloroform solvent (denoted as CPCM-M062X/6-311G(d,p)) using the Gaussian 09 software. Parameters such as vertical ionization potentials (IPs, computed as the energy difference between the single point energy of the radical cation and the energy of the neutral system) and electron affinities (EAs, computed as the energy difference between the total energy of the neutral system and single point energy of the radical anion system) are calculated at

this level of theory. M06-2X functional is chosen for the blends as this functional has performed well for other donor-acceptor blends in literature.[115, 163, 205] For these donor-acceptor blends, excited states which include charge-transfer states are calculated using the CAM-B3LYP range-separated functional with 6-311G(d,p) basis set (denoted as TD-CPCM-CAMB3LYP/6-311G(d,p)). For analyzing the excited state properties, the Multiwfn software package is utilized.

5.3 Results and discussion

5.3.1 Ground state molecular geometries

Conformation of a molecule has a great effect on the photophysical properties. In Figure 5.2, structures of optimized ground-state geometries of all the five tetramers are shown. As observed, **P5** with thiazole π bridge units exhibits a planar structure. All other tetramers are non-planar. In the case of **P1**, each junction between the BDTT and TT-F units has a non-zero dihedral angle which is due to the steric hindrance between the adjacent atoms. In **P2**, the adjacent TT-F, furan and BDTT units are in the same plane. But whenever the fluorine atom of TT-F and oxygen atom of furan are close, a non-zero dihedral angle is produced making the system non-planar. Similarly, non-zero dihedral angles appear at the junctions of TT-F and other units in cases of **P3** and **P4**. Dihedral angles (ϕs as indicated in Fig. C1 (see Appendix C)) of the tetramers are tabulated in Table 5.3. Taking the example of ϕ_1, it is observed that introduction of π bridge units furan, thienothiophene, thiophene, and thiazole results in decrease in the value of ϕ_1. This value is the smallest for **P5**. When **P2** is modified to **P3** by replacing the furan π bridge unit by thienothiophene, the change in ϕ_1 - ϕ_{15} values are observed to be larger. But changing the bridge units to thiophene units results in smaller changes in the dihedral angles ϕ_1 - ϕ_{15}. In case of **P5** which contains the π bridge thiazole, all the ϕ_1 - ϕ_{15} values are found to be very small making the molecule planar. The carbon-carbon single bond values of **P1**- **P5** tetramers are between

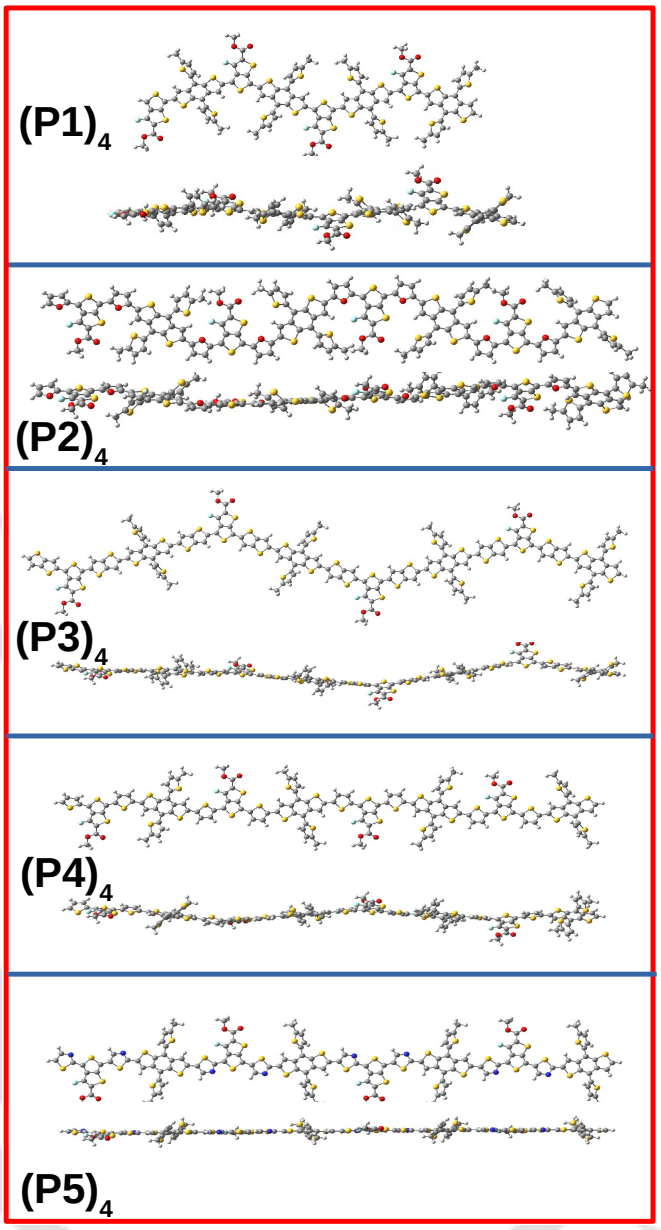

FIGURE 5.2: Optimized geometries of tetramers of **P1**, **P2**, **P3**, **P4** and **P5**. For each tetramer, both top and side views are shown. The results are obtained at CPCM-PBE0/6-311G(d,p) level of theory.

1.41-1.44 Å, which are shorter than that of the C-C single bond (1.54 Å). Planarity of **P5** hints at better light absorption properties compared to others.

TABLE 5.3: Selected dihedral angles(ϕ (deg)) of the optimized structures of all oligomers in their neutral ground states at CPCM-PBE0/6-311G(d,p) level. ϕ_1-ϕ_{15} are seen in Figure 1.

Tetramers/Angles	**P1**	**P2**	**P3**	**P4**	**P5**
ϕ_1	-19.47	-3.47	-15.16	-13.59	-0.69
ϕ_2	27.33	-0.51	-18.46	10.41	1.91
ϕ_3	-18.33	-13.54	28.83	-26.79	-1.00
ϕ_4	27.17	0.09	13.65	13.89	1.17
ϕ_5	-19.94	-4.06	-15.27	-11.24	-1.13
ϕ_6	28.35	-0.80	-18.73	11.83	2.51
ϕ_7	-17.04	-13.42	29.97	-26.25	-1.41
ϕ_8		0.02	14.98	14.48	-0.08
ϕ_9		-3.70	-13.86	-12.10	-0.80
ϕ_{10}		-1.06	-18.05	10.13	0.22
ϕ_{11}		-13.68	27.93	-27.21	-1.21
ϕ_{12}		0.20	8.70	13.01	0.12
ϕ_{13}		-4.39	-15.78	-12.25	-1.70
ϕ_{14}		-2.40	-19.86	10.90	-7.32
ϕ_{15}		0.79	31.25	-31.37	0.74

5.3.2 Frontier molecular orbitals and open-circuit voltages

Energies of frontier molecular orbitals, especially those of HOMO and LUMO, influence V_{oc} and ΔE_{LL}.[116] An ideal donor material should have relatively smaller HOMO level to achieve larger V_{oc}. Energies of HOMOs and LUMOs of **P1-P5** are tabulated in Table 5.4. The π bridges have a significant effect on the energies of HOMOs and LUMOs. The HOMO energy levels are in the following order: **P2** (-5.11 eV) > **P4** (-5.26 eV) > **P3** (-5.27 eV) > **P1** (-5.36 eV) > **P5** (-5.47 eV). While the HOMO values of **P3** and **P4** are closer to that of **P1**, the level for **P2** with furan π bridges is much larger lying at -5.11 eV. We note here that there is a vast literature on furan, thiophene, thienothiophene and thiazole as π bridges and their effects on photovoltaic properties. Wang et al.[206] observed that changing the π bridge from furan to thiophene and then to thienothiophene resulted in uplifting the HOMO levels. Similar observation was made by Liu et al.[207] for furan and thiophene π bridges. In general, thienothiophene π bridges induce larger steric hindrance which produces a larger HOMO level. Du et al.[208]

TABLE 5.4: Energies of HOMO (E_{HOMO} in eV) and LUMO (E_{LUMO} in eV) of all **P1**-**P5** tetramers and **PCBM**. Driving force (ΔE_{LL} in eV) and open-circuit voltages (V_{oc}in V) of all the oligomers are also shown. E_{H}s are obtained at CPCM-PBE0/6-311G(d,p) level. E_{LUMO} are obtained by adding E_{g}^{1} values to the E_{HOMO} values.

Compounds	E_{HOMO}	E_{LUMO}	ΔE_{LL}	V_{oc}(V)
P1	-5.36	-3.63	0.67	0.76
P2	-5.11	-3.48	0.81	0.51
P3	-5.27	-3.55	0.75	0.67
P4	-5.26	-3.57	0.73	0.66
P5	-5.47	-3.85	0.45	0.87
PCBM	-6.19	-4.30		

showed that π bridges thiophene and thienothiophene induced minor effects on the HOMO and LUMO values. Hence, the variation of HOMO and LUMO levels with respect to the π bridges depends on the molecular structure. In our case, similar to the results of Du et al[208], both thiophene and thienothiophene based tetramers exhibit similar HOMO and LUMO energy levels. Furan having the smaller oxygen heteroatom is not expected to induce any steric hindrance. In addition, high electronegativity of the oxygen atom helps to lower the HOMO level. But in our case, the structure of the tetramer results in up-shifting the HOMO value. Thiazole is a weak electron donor, exhibits stronger electron affinity and helps in reducing the steric hindrance with the neighboring unit. As a result, its incorporation as a π bridge is a well known strategy to lower the HOMO/LUMO levels.[209–212] In our case too, **P5** having thiazole π bridge units has the deepest HOMO among the tetramers. The LUMOs follow the order: **P2** (-3.48 eV) > **P3** (-3.55 eV) > **P4** (-3.57 eV) > **P1** (-3.63 eV) > **P5** (-3.85 eV). These LUMO levels are higher-lying than that of **PCBM** (ca. -4.30 eV). Hence, efficient charge transfer is expected in the devices.

Table 5.4, in addition to showing the HOMO/LUMO energies of the donors, also shows the HOMO/LUMO energies of **PCBM** acceptor and the calculated V_{oc} values. The calculated value of 0.76 V for **P1** is in good agreement with the experimental value of 0.81 V.[202] As shown, **P2** and **P5** have the smallest and

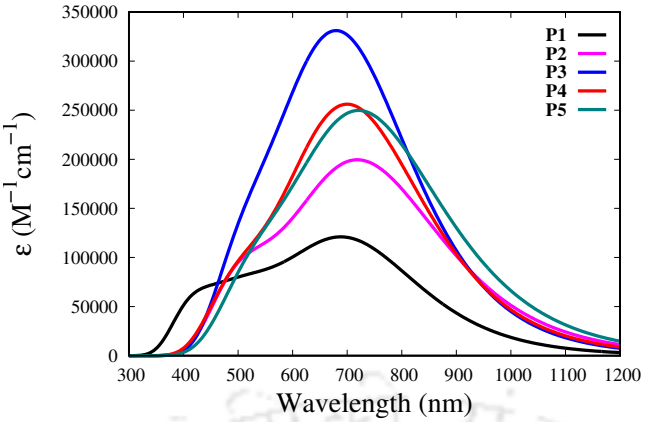

FIGURE 5.3: Simulated absorption spectra of **P1**-**P5** at the TD-CPCM-HSE06/6-311G(d, p) level. Half- width at half-maximum height is 2500 cm^{-1}.

largest V_{oc} values, respectively. The V_{oc} values are in the following order: **P5** > **P1** > **P3** > **P4** > **P2**. As such, all of the newly designed tetramers exhibit suitable values of V_{oc}. Table 5.4 also shows the ΔE_{LL} values. All ΔE_{LL} are larger than 0.3 eV, which ensures efficient exciton dissociation.

HOMOs and LUMOs of $(\mathbf{P1})_4$ and $(\mathbf{P2})_4$-$(\mathbf{P5})_4$ are shown in Figures C2 and C3, respectively (see Appendix C). As the Figure C2 shows, HOMO is distributed over the whole molecule. For the LUMO, the distribution is over the whole molecule except the terminal BDTT unit. Addition of π bridges does not change the scenario much and as shown in Figure C3, similar distributions are observed.

5.3.3 Optical absorption and excited-state properties

As observed in the previous section, structural modifications of the parent molecule **P1** affect the conjugation and the HOMO-LUMO energies. Such structural changes will also affect the absorption ability of the donor. J_{sc} is dependent on the absorption ability of the donor, and a strong absorption to match the solar spectrum is required. As mentioned before, the calculated λ_{max} for **P1** is 716 nm, which is in good agreement with the experimental result of 703 nm.[202]

TABLE 5.5: First excitation energies (E_g^1), maximum absorption wavelengths (λ_{max}), contributions of HOMO to LUMO excitations for $S_0 \rightarrow S_1$, oscillator strengths (f_{osc}), light absorption efficiencies (η_λ) for all the tetramers. The results are obtained at TD-CPCM-HSE06/6-311G(d,p) level.

Compounds	E_g	λ_{max}(nm)	% contribution of H→L transition	f_{osc}	η_λ
P1	1.73	716	99%	2.40	0.996
P2	1.63	760	97%	3.24	0.999
P3	1.72	719	95%	4.99	0.999
P4	1.69	734	97%	4.30	0.999
P5	1.62	762	97%	4.03	0.999

Simulated absorption spectra of $(\mathbf{P1})_4$-$(\mathbf{P5})_4$ are shown in Figure 5.3. E_g^1s, λ_{max}s, f_{osc}s and percentage contributions of H→ L transitions are summarized in Table 5.5. λ_{max} values of **P2** - **P5** tetramers are 760, 719, 734 and 762 nm, respectively, inferring that the maximum absorption peaks for these π-bridged systems are red-shifted in comparison to that of **P1** and this is beneficial for improving J_{sc}. Incorporation of π bridges results in extension of π-conjugation length leading to bathochromic shifts. In addition, f_{osc} values of **P2-P5** are also larger than that of **P1** due to increase in conjugation lengths.[213] It is also observed that the newly designed tetramers exhibit better η_λ values compared to that of **P1**. Table 5.5 also shows that the $S_0 \rightarrow S_1$ transitions are dominated by HOMO→LUMO excitations in all the cases and the contributions of H→ L excitations are 99%, 97%, 95%, 97% and 97% for **P1-P5**, respectively.

5.3.4 Structures and properties of the D/A blends, charge transfer states and exciton binding energies

As mentioned in the Methodology section, structures of composite systems **P1-P5/PCBM** are obtained at CPCM-M062X/6-311G(d,p) level. All the optimized structures are shown in Figure C4 (see Appendix C). As observed in these two figures, structures of π-bridged donor/**PCBM** composites are very different than the structure of **P1/PCBM**. The optimized vertical distances between the donor

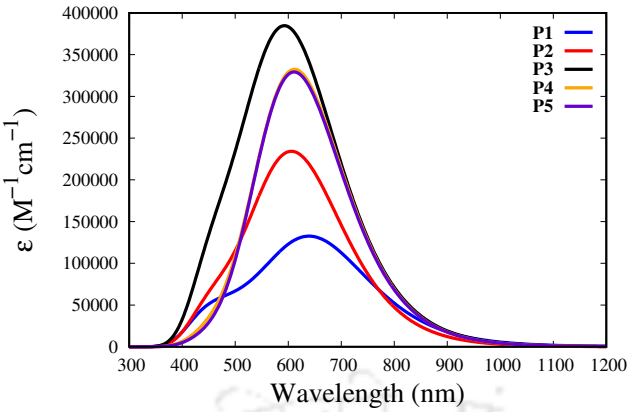

FIGURE 5.4: Simulated absorption spectra of **P1-P5/PCBM** composite systems at the TD-CPCM-CAMB3LYP/6-311G(d,p) level. Half-width at half-maximum height is 2500 cm^{-1}.

oligomers and **PCBM** are 3.20 Å, 3.40 Å, 3.50 Å, 3.52 Å and 3.18 Å for **P1-P5/PCBM**, respectively.

Simulated absorption spectra of the five blend structures are shown in Figure 5.4. Each spectrum shows only one peak with a very large f_{osc} and the f_{osc} values of these peaks for **P2-P5/PCBM** blends are much larger than that of **P1/PCBM**. λ_{max} values of **P1-P5/PCBM** composite systems are 656, 618, 629, 616 and 618 nm, respectively. This shows that while the λ_{max} values of the newly designed composites are close to each other, those are blue-shifted with respect to that of **P1/PCBM**. Excitation energies, corresponding oscillator strengths, l^{CT} and types of excited-states of the composite systems **P1/PCBM** and **P2-P5/PCBM** are tabulated in Table 5.6. The table shows that all the above mentioned peaks in the absorption spectra correspond to $S_0 \rightarrow S_1$ transitions. It is notable that the oscillator strengths of first excitations are greatly enhanced upon incorporation of π bridges. Excited states can be assigned either as locally-excited (LE) or ICT states. In our case, CDD plots are used to assign the character of the states. As an example, CDD plots for three different excited states of **P1/PCBM** composite are shown in Figure 5.5. This figure shows that the electrons and holes are localized either on **P1** or on **PCBM**, for S_1 and S_8 states, respectively and these are assigned as LE states. But in the case of S_5, holes and electrons are

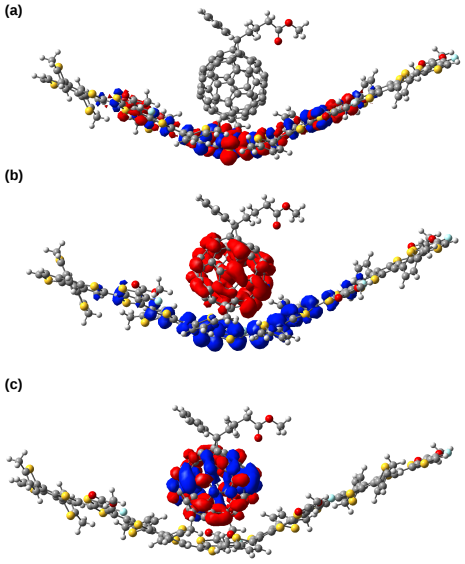

FIGURE 5.5: Charge density difference plots for S_1(a), S_5(b), and S_8(c) excited states of the **P1/PCBM** composite. Blue (red) stands for depletion (accumulation) of negative charges. While S_1 and S_8 are LE states, S_5 is a CT state. These results are obtained at TD-CPCM-CAMB3LYP/6-311G(d,p) level of theory.

on the donor and acceptor parts, respectively and this state at 530 nm is identified as the first ICT state in case of **P1/PCBM** composite. The f_{osc} for $S_0 \rightarrow S_5$ is quite small. Similar to the results of **P1/PCBM**, first excited states in the other four composites are also LE states. As seen in the Figure 5.6, S_6 state for **P2/PCBM**, S_6 state for **P3/PCBM**, S_9 state for **P4/PCBM** and S_{11} for **P5/PCBM** are the first ICT states. These ICT states appear at 526 nm, 540 nm, 498 nm, 475 nm, respectively, for **P2-P5/PCBM**. As shown in the Table 5.6, l^{CT} values for the above charge-transfer states of **P1-P5/PCBM** are 3.47 Å, 4.36 Å, 8.23 Å, 5.43 Å and 3.22 Å, respectively. Above l^{CT} values are relatively larger than the values of various low-lying LE states inferring that electrons and holes are clearly separated in the excited states, and that there are greater extents of charge transfers. In particular, l^{CT} for the first ICT state of thienothiophene based composite is very large. It is to be noted from the table that there are other excited states for which l^{CT} values are still larger but those are still LE states.

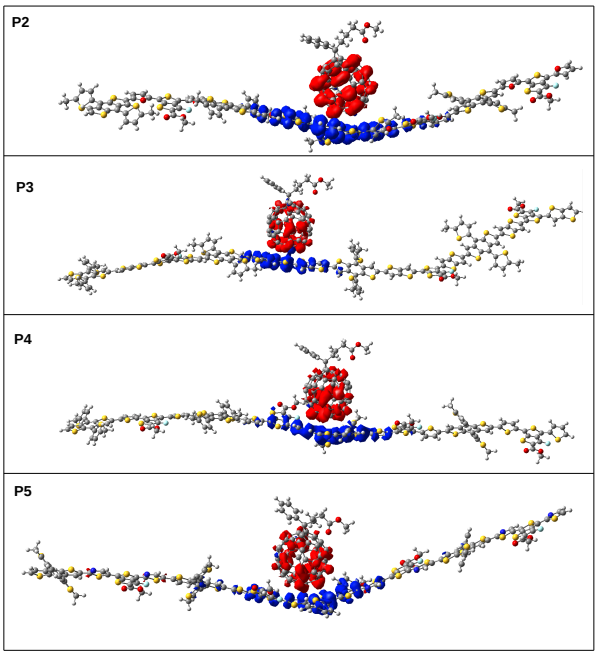

FIGURE 5.6: Charge density difference plots for the S_6, S_6, S_9 and S_{11} of the **P2-P5/PCBM** interfacial systems. The mentioned states are the first ICT states.

Hence, l^{CT} values alone cannot correctly identify an ICT state. Rather a combinations of CDD and l^{CT} values provide a correct description of type of excited states. In addition to CDD plots, transition density matrix (TDM) analysis is also effective in understanding the charge transfer and characterizing the excited states. Diagonal and off-diagonal elements of the TDM matrix reveal local and charge-transfer characters, respectively. As shown in the Figure 5.7, the S_1 and S_8 states involve electron-hole correlations within local sites, i.e. donor and acceptor parts, respectively, only. On the other hand, the results for S_5 state shows that there is electron-hole coherence between the donor **P1** and **PCBM**. Similar plots for two locally excited and the first charge transfer states of other composites are shown in Figures C5 and C6 (see Appendix C).

E_{b} is the energy to be overcome for the dissociation of an exciton to an electron and a hole at the interface. IP, EA and $E^{1}_{\mathrm{g,Blend}}$ values are tabulated in Table C1. Smaller the E_{b} value, better is the possibility of charge separation. E_{b} values for $(\mathbf{P1})_4$-$(\mathbf{P5})_4$ are shown in Table 5.7. Our calculated E_{b}s vary between

TABLE 5.6: Excitation energies ($E_{g,Blend}$), oscillator strengths (f_{osc}), charge transfer lengths (l^{CT}) and types of excited states of the **P1-P5/PCBM** blend systems. $E_{g,Blend}$s are in eV. The values inside the parentheses in the third column are the wavelengths in nm corresponding to the $E_{g,Blend}$s in eV. These results are obtained at TD-CPCM-CAMB3LYP/6-311G(d,p) level.

Oligomer/**PCBM**	States	$E_{g,Blend}$(eV)	f_{osc}	l^{CT}(Å)	Type of excited state
P1	S_1	1.88(656)	2.6979	2.422	LE
	S_2	2.16(572)	0.2603	3.462	LE
	S_3	2.26(547)	0.0031	2.026	LE
	S_4	2.29(539)	0.0064	2.439	LE
	S_5	2.33(530)	0.0785	3.474	ICT
	S_6	2.34(527)	0.1084	3.100	ICT
	S_7	2.36(524)	0.5404	2.774	LE
	S_8	2.42(511)	0.0002	0.988	LE
	S_9	2.43(509)	0.0010	1.262	LE
	S_{10}	2.48(498)	0.0085	3.083	ICT
P2	S_1	2.00(618)	4.696	3.223	LE
	S_2	2.10(588)	0.085	4.147	LE
	S_3	2.21(560)	0.456	4.056	LE
	S_4	2.17(545)	0.001	1.312	LE
	S_5	2.31(536)	0.002	1.921	LE
	S_6	2.35(526)	0.012	4.366	ICT
	S_7	2.37(522)	0.010	4.267	ICT
	S_8	2.41(514)	0.000	0.786	LE
	S_9	2.42(510)	0.000	0.829	LE
	S_{10}	2.45(505)	0.804	15.065	LE
P3	S_1	1.96(629)	4.748	9.809	LE
	S_2	2.11(586)	1.621	15.277	LE
	S_3	2.18(567)	2.344	13.910	LE
	S_4	2.24(553)	0.007	1.355	LE
	S_5	2.27(544)	0.000	1.492	LE
	S_6	2.29(540)	0.012	8.231	ICT
	S_7	2.36(524)	0.151	10.237	ICT
	S_8	2.37(522)	0.630	19.212	LE
	S_9	2.41(513)	0.000	3.961	LE
	S_{10}	2.42(511)	0.006	3.845	LE
P4	S_1	2.01(616)	7.233	3.389	LE
	S_2	2.07(597)	0.157	7.214	LE
	S_3	2.26(546)	0.046	4.981	LE
	S_4	2.27(543)	0.003	0.990	LE
	S_5	2.31(534)	0.001	1.084	LE
	S_6	2.40(515)	0.001	1.097	LE
	S_7	2.41(512)	0.001	0.568	LE
	S_8	2.43(509)	0.738	16.631	LE
	S_9	2.48(498)	0.001	5.433	ICT
	S_{10}	2.50(495)	0.001	5.259	ICT
P5	S_1	2.00(618)	6.820	3.491	LE
	S_2	2.09(590)	0.255	4.661	LE
	S_3	2.21(559)	0.419	5.067	LE
	S_4	2.27(545)	0.002	0.945	LE
	S_5	2.31(536)	0.001	1.358	LE
	S_6	2.40(514)	0.519	13.966	LE
	S_7	2.41(513)	0.008	0.805	LE
	S_8	2.42(512)	0.001	0.651	LE
	S_9	2.55(484)	0.001	1.061	LE
	S_{10}	2.58(478)	0.001	2.440	LE

0.08-0.41. While **P2** possess the smallest E_b largest E_b occurs for **P5**. Hence, dissociation of exciton to free charge carriers is difficult in **P5**.

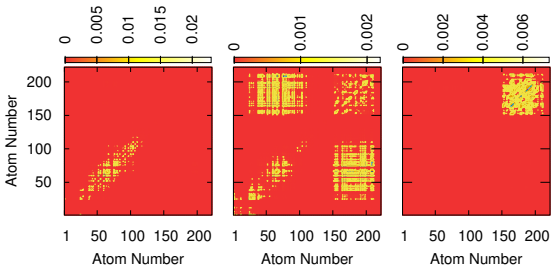

FIGURE 5.7: Two-dimensional site representation of the transition density matrix (TDM) for S_1, S_5 and S_8 excited states (from left to right) of the **P1/PCBM** composite system. Both X and Y-axes represent the atom numbers. Atom numbers 1-148 are for the donor **P1** and from 148 onwards are for the acceptor **PCBM**. Hydrogen atoms are ignored here. These results are obtained at TD-CPCM-CAMB3LYP/6-311G(d,p) level of theory.

5.3.5 Rates of charge transfer and charge recombination processes

Rates of charge recombination and charge transfer are calculated using the Marcus rate equation shown in the Eq. 2.41. An efficient OSC device should have large k_{CT} value to facilitate faster charge transfer and small k_{CR} so that there is smaller chance of electron-hole recombination. Eq. 2.41 shows that as the magnitudes of ΔG and λ approach each other, rate increases and the maximum is reached when ΔG = -λ. Additionally, rate increases on decreasing $|\Delta G_{CT}|$ when ΔG_{CT} + $\lambda < 0$. Below we discuss the variation of each of the parameters used in the Eq. 2.41 to evaluate the rates with respect to structures of the composites. Values of all the parameters are tabulated in the Table 5.7. The values of $|\Delta G_{CR}|$ follow the sequence: **P2/PCBM** > **P3/PCBM** ∼ **P4/PCBM** > **P1/PCBM** > **P5/PCBM**. A comparatively larger IP value of **P5** results in a comparatively larger $|\Delta G_{CR}|$ which results in significantly smaller k_{CR} value as seen below. As shown in Table 5.7, ΔG_{CT} values of **P1- P5/PCBM** are -0.22, -0.11, -0.20, -0.13 and -0.09 eV, respectively. All the ΔG_{CT} values are negative, implying that the electron transfer is a thermodynamically favorable process in each system. Compared to the calculated value of **P1**, the designed oligomers exhibit smaller ΔG_{CT}s. A very small value of -0.09 eV for **P5** arises because of larger $|\Delta G_{CR}|$, and a comparatively larger E_b. As we show later, these values have large influence

TABLE 5.7: Calculated parameters for the Eq. 2.41. Differences in dipole moments between the ground and the excited states ($\Delta\mu$) and transition dipole moments (μ_{trans}) are in atomic units. Exciton binding energies (E_b), charge transfer integral (V_{DA}), changes in Gibbs free energy during charge transfer-/charge recombination ($\Delta G_{CT/CR}$) and reorganization energies (λs) are in eV. Charge transfer (k_{CT}) and charge recombination rates (k_{CR}) are in s^{-1}.

Blends	$\mid \Delta\mu \mid$	μ_{trans}	V_{DA}	λ	E_b	$\Delta G_{CT/CR}$	k_{CT}	k_{CR}
P1/PCBM	0.03	-0.53	-1.15	0.47	0.28	-0.22/-1.79	8.94×10^{15}	7.32×10^{0}
P2/PCBM	0.71	0.22	0.63	0.43	0.07	-0.11/-1.59	9.75×10^{14}	5.63×10^{2}
P3/PCBM	0.25	0.45	1.11	0.47	0.19	-0.20/-1.71	6.60×10^{15}	2.93×10^{2}
P4/PCBM	3.80	0.02	0.02	0.46	0.15	-0.13/-1.71	7.54×10^{11}	1.79×10^{-2}
P5/PCBM	1.48	0.09	0.17	0.43	0.41	-0.09/-1.96	5.06×10^{13}	5.32×10^{-9}

on the charge transfer and charge recombination rates. The calculated λ_{int} values of $(\mathbf{P1})_4$ - $(\mathbf{P5})_4$**/PCBM** composite systems are in the range 0.42 - 0.46 eV and are in the following sequence: **P1**(0.47) $\sim$ **P3**(0.47) $>$ **P4**(0.46) $>$ **P2**(0.43) $\sim$ **P5**(0.43). For all the systems, λ values are closer to corresponding ΔG_{CT} values than ΔG_{CR} inferring good charge transfer properties. In case of **P5**, λ and ΔG_{CT} values are farthest from each other.

It should be reiterated that the first intermolecular charge transfer states for **P1-P5** composites are S_5, S_6, S_6, S_9 and S_{11}, respectively and these states are considered for V_{DA} calculations. V_{DA} values of these five interfaces **P1-P5/PCBM** are -1.15, 0.63, 1.11, 0.02 and 0.17 eV, respectively. Newly designed oligomers **P2-P5** have smaller absolute V_{DA} values compared to that of **P1** which may negatively affect the rate as rate is directly related to the square of V_{DA}, particularly when λ and ΔG_{CT} values are close to each other. Here, **P1** and **P3** tetramer blends showing larger $|V_{DA}|$ values have larger k_{CT}s. The calculated k_{CT} values are in the following order: **P1** $>$ **P3** $>$ **P2** $>$ **P5** $>$ **P4**. As observed in Table 5.7, **P1** has the largest charge transfer rate among all. In case of **P4**, although the ΔG_{CT} value is closer to λ, a very small value of V_{DA} results in a smaller k_{CT}. It is also observed from Table 5.7 that k_{CR}s of **P4** and **P5** tetramers are smaller compared to the parent **P1** and that **P5** has the slowest recombination rate (5.32×10^{-9} s^{-1}) among the designed **P2-P4** systems. The calculated k_{CR} values for **P1-P5/PCBM** are in the following the order: **P2** $>$ **P3** $>$ **P1** $>$ **P4** $>$

P5. According to the above results, in case of BDTT-π-TT-F based oligomers, thiophene and thiazole π bridge units are more suitable for active layer engineering than the other considered π bridges. We note here that ΔG values are calculated using the IP and EA values, and values of these parameters are density functional dependent. In addition, calculation of EA values, as well known, is very much dependent on the basis sets. Ideally, basis set involving diffuse functions are to be used for anion calculations which are not used in our studies because of large sizes of our systems. All these may be the reason for such large $|\Delta G_{CR}|$ values resulting in very small rates. In the end, we would like to add that morphological features of thin films greatly affect the device performance, and these features which cover various length scales need to be taken into account while modeling the devices to predict their performances. In addition, the morphology is usually dependent on the processing methods and conditions. Prediction of solid state structures by carrying out DFT studies is a difficult task nonetheless and our computational design strategy does not take this into account. Hence, the results presented here serve as a guide for the molecular designing only.

5.4 Conclusions

In summary, detailed quantum chemical studies are carried out for four newly designed oligomers which differ from the experimentally studied polymer by having four different π bridges between the benzodithiophene donor and the thienothiophene acceptor parts. Furan, thienothiophene, thiophene, and thiazole are used as the four π bridges. Structural, optoelectronic, and charge transfer properties of the **P1**-**P5** oligomers are studied. Introduction of the π bridge units results in red-shifting of the absorption wavelengths. Among the simulated composites, thiophene and thiazole based composites are found to have smaller charge recombination rates than that of **P1**. Hence, better PCE values are expected for devices based on thiophene and thiazole π bridges in BDTT-π-TT composites.

Chapter 6

Random donor and non-fullerene acceptor based active layer: effects of insertion of various π linkers

In this chapter, structural, optoelectronic, and charge transfer properties of random benzodithiophene-thienothiophene donor and non-fullerene acceptor based polymers are investigated. A part of the content of this chapter is is published in *J. Phys. Chem. A*, **2021**, 125, 9852.

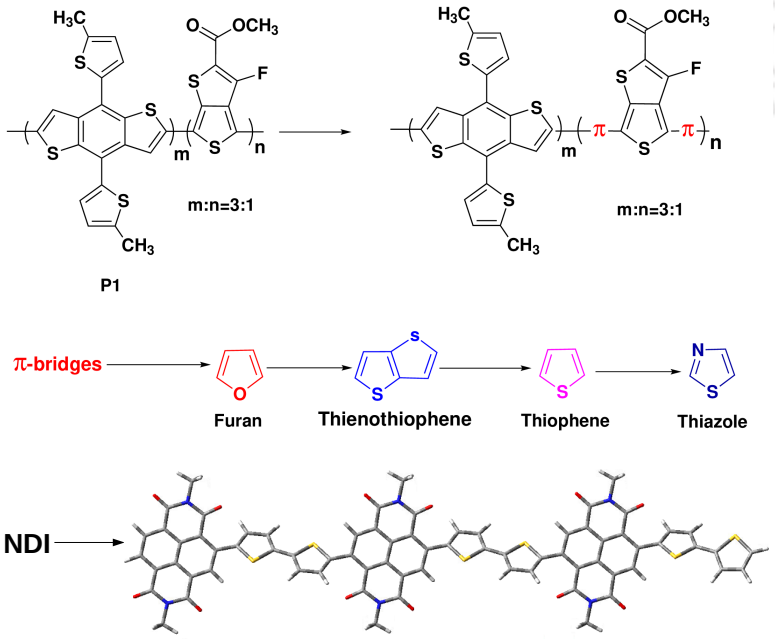

Figure: Structures of π-bridge-based random donor-acceptor oligomers and acceptor **NDI**.

6.1 Introduction

In the previous chapter, we assessed the effects of different π bridges on the properties of donors, and eventually, on the charge transfer properties of donor/**PCBM** blends. In this chapter, we have taken a step forward, and studied the effect of π bridges on random donors. This is followed by studies of charge transfer in blends of these random oligomers with a non-fullerene acceptor. The idea originated from a work by Kim et al.[202] who reported that random polymers blended with non-fullerene acceptors showed better PCEs than the alternating polymer/**PCBM** blends. Below, we provide a brief overview of the current status of random polymers and their usage in OSCs.

In recent times, random polymers have provided another route for molecular design. Common D-A alternating copolymers have a fixed 1:1 ratio of donors and acceptors. On the other hand, random polymers, either binary or terpolymers, with different composition ratios have recently been shown to produce better PCE values in comparison to corresponding alternating copolymers.[214–227] Ling and coworkers[226] synthesized random copolymers with varying molar ratios of donor BDTT and acceptor thieno[3,4-c]pyrrole-4,6-dione. A higher PCE value of 8.20% was achieved with 5:4 ratio of D/A, compared to other ratios of donor and acceptor. Kim et al.[221] developed alternating and a series of random copolymers with different donor-acceptor compositions. The device based on one of the random copolymer with a D:A ratio of 2:1 produced a PCE value higher than the alternating polymer based device. Recently, Xiao et al.[214] developed a series of random ternary copolymers by combining an ester-substituted thiazole unit as the third component with the D-A based PM6 copolymer. One of the random terpolymer based devices was found to have a PCE value of 16.28%, higher than that of only PM6 based device. A terpolymer designed by inserting a fluorine and ester substituted thiophene unit into the PM6 polymer showed a PCE of 16.4%. A higher PCE value of 14.08% was achieved in the device from random terpolymers based on BDTT, naphtho[2,3-c]thiophene-4,9-dione and BDD.[225]

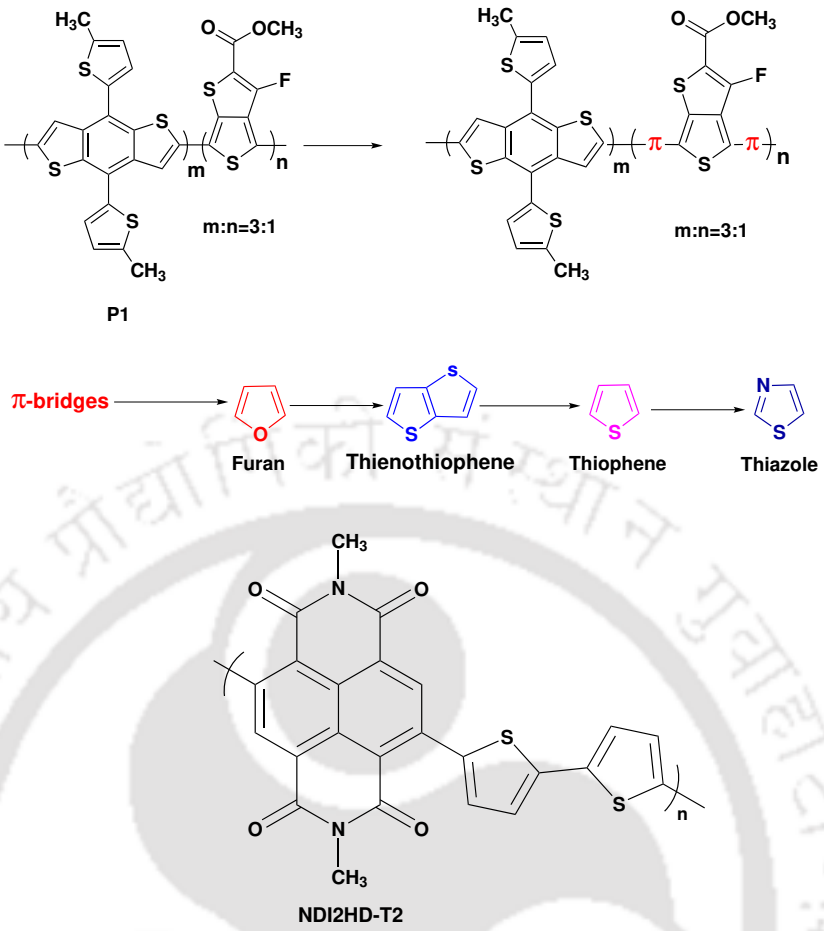

FIGURE 6.1: Structures of **P1-TzP1** repeating units. **FuP1-TzP1** are obtained by incorporation of four different π-bridges between donor and acceptor units. The four different π-bridge units are also shown. Structure of non-fullerene acceptor **NDI2HD-T2** is also shown.

Further improvements to the backbone structure to absorb more photons can be achieved by inserting π bridges between the donor and acceptor units. Conjugated π bridge units modify the interaction between the donor and acceptor units, usually making the structure more planar and this results in elongated conjugation length along the donor backbone due to improved overlap of π-orbitals. As a consequence, optical, charge transfer and photovoltaic properties are also affected. Typically, small conjugated aromatic rings such as furan, pyrrole, thiophene, thienothiophene, selenophene, thiazole or benzodithiazole are used as π bridges. Many experimental and computational studies have shown that added π bridges have resulted in increased PCE values.[92, 114, 115, 192, 208, 228–236]. We

have been interested in understanding the effects of modifications of donor copolymer, in particular the BDT based units, on the photo-physical properties.[92, 148] In the present work, we focus on the effect of π bridges in the random binary polymer donors. Our aim is manifold: to examine the effect of insertion of strong and weak electron donor π bridges on the (a) binding energies of polymer donors with non-fullerene acceptor, (b) optoelectronic properties, (c) exciton binding energies and (d) charge transfer and charge recombination processes. Recently, Kim et al.[202] synthesized a series of alternating and random polymer based on BDTT and the electron-deficient unit, fluorinated thieno[3,4-b]thiophene (TT-F). It was found that polymer composition had a large effect on the photovoltaic properties and the highest PCE was observed for a random polymer with complementary light absorption property with the polymer acceptor, poly[N,N′-bis(2-hexyldecyl)-naphthalene-1,4,5,8-bis(dicarboximide)-2,6-diyl]-alt-5,5'-(2,2'-bithiophene) (**NDI2HD-T2**). Although the highest PCE was obtained for the all-polymer OSC based on the donor with 5:1 ratio of D/A, the PCE value of the OSC with 3:1 ratio of D/A was very close (6.81 vs 6.53). Considering that a studying an oligomer with a D/A ratio of 5:1 computationally is too expensive, we chose the random copolymer with a 3:1 D/A ratio to study the effect of incorporation of π bridges. The above system is denoted as **P1**. Starting with **P1**, π bridges furan, thienothiophene, thiophene, and thiazole units are incorporated between the D and A units in the conjugated backbone. These newly designed oligomers are denoted as **FuP1**, **TtP1**, **ThP1** and **TzP1**. In addition, an extra π bridge unit is placed at each terminal. Schematic structures of the four resultant π-bridged systems are shown in Figure 6.1. Details of computational methods are shown in the next section. This is followed by the Results & Discussion. Finally, we provide conclusions of our study in the last section.

6.2 Computational Methodologies

All the calculations for **P1**-**TzP1** oligomers, acceptor **NDI2HD-T2** and the donor/**NDI2HD-T2** blends are carried out at the DFT level. Choosing proper

TABLE 6.1: Energies of the E_{HOMO} and E_{LUMO} of **P1** using the B3LYP, PBE0, HSE06 and M06 functionals, and 6-311G(d,p) basis set. LUMO energies are obtained by adding the first excitation energy (E_g^1) to the HOMO energy. All the energies are in eV.

P1	B3LYP	PBE0	HSE06	M06	Exp.[202]
E_{HOMO}	-5.03	-5.19	-4.83	-5.25	-5.34
E_{LUMO}	-2.96	-3.12	-2.77	-3.19	-3.67

DFT functionals to carry out ground and excited state calculations is very important. In this scenario, test calculations are carried out with different functionals and basis sets to reproduce the experimental HOMO energy and E_g^1 of **P1**, the parent system. For a random dimer, various arrangements of donor and acceptor units are possible and hence, it is important to find the preferred conformation. To find the most stable structure of **P1**, the following five different possibilities for the random arrangement of donor and acceptor units are considered: (i) D-D-D-A-A-D-D-D, (ii) D-D-A-D-D-D-A-D, (iii) D-A-D-D-D-D-A-D, (iv) D-A-D-A-D-D-D-D, and (v) A-D-D-D-D-D-D-A. These random arrangements of the D-A systems are optimized at M06[237]/6-311G(d,p) level. The fifth arrangement provides the most stable geometry and better planarity than the other models. Therefore, this arrangement, A-D-D-D-D-D-D-A, for **P1** dimer is chosen for further studies. Further, three other DFT functionals, B3LYP, PBE0, and HSE06 with 6-311G(d,p) basis set, are also used to optimize the geometries of dimer **P1** and compare the resultant energy of HOMO with the experimental result. As reported in Table 6.1, the energy of HOMO of **P1** dimer using the M06 functional matches quite well with the experimental result.[202] Hence, all the remaining (**FuP1**)$_2$-(**TzP1**)$_2$ calculations are also carried out at the M06/6-311G (d,p) level of theory. From now onward, the dimer (**P1**)$_2$ will be denoted as **P1** only, and so are the other dimers.

The absorption spectrum of **P1** is calculated at TD-DFT level with various functionals such as HSE06, PBE0, B3LYP and M06 using the 6-311G(d,p) basis set. All absorption spectra calculations are performed using CPCM in the chloroform solvent.[204, 238] Table 6.2 shows that the calculated λ_{max} of **P1** at

TABLE 6.2: Calculated first excitation energies (E_g^1 in eV) and corresponding absorption wavelengths (λ_{max} in nm) of **P1** in chloroform solvent using four different hybrid functionals with the 6-311G(d,p) basis set.

P1	E_g^1	λ_{max}	Exp.[202]
HSE06	2.07	600	615
PBE0	2.27	546	
B3LYP	2.15	575	
M06	2.27	546	

HSE06/6-311G(d,p) level agrees well with the experimental value.[202] Thus, the HSE06/6-311G (d,p) level is used for excited state calculations of all newly designed oligomers. Energies of LUMOs are computed by adding E_g^1 values to the HOMO energies. Literature shows that this method of computing LUMO values works better compared to taking LUMO energies from the ground state calculations.[124, 125, 148, 239, 240] EAs, IPs of dimers are also calculated at M06/6-311G(d,p) level based on neutral and anion/cation optimized geometries. As mentioned in the Introduction, **NDI2HD-T2** (denoted as **NDI** from now onward) is used as the electron acceptor. The structure of **NDI** is optimized at HSE06/6-311G(d,p) level. It was found that trimer of **NDI** produces a HOMO/LUMO levels comparable to the experimental energies and hence, we have considered trimer of **NDI** in all the studies. All these electronic structure calculations are performed using the Gaussian 16 software package.[241]

For the donor/acceptor blend structures, optimizations were carried out using the PBE functional and the def2-SV(P) basis set. Considering the sizes of systems, resolution of identity (RI) approximation was used in these optimizations which also included the Grimme's D3 dispersion correction scheme as implemented in the TURBOMOLE V7.1 software.[147] Following geometries optimizations, single point calculations are carried out at the M06/6-311G(d,P) level using the Gaussian 16 software package. Following the above, vertical IPs and EAs are also calculated at M06/6-311G(d,P) level, in a fashion similar to the donor IP and EA calculations. Excited state studies for these blends are carried out using the long-range separated CAM-B3LYP functional and 6-311G(d,p) basis set in chloroform solvent. For

TABLE 6.3: Selected dihedral angles (ϕ in degree) of the optimized ground-state structures of **P1-P5**. ϕ_1, ϕ_2, ϕ_3 and ϕ_4 are seen in Figure 6.2

Compounds	ϕ_1	ϕ_2	ϕ_3	ϕ_4
P1	20.3	-	-	-
FuP1	-	5.6	4.4	21.0
TtP1	-	17.4	25.1	33.0
ThP1	-	10.8	12.6	33.4
TzP1	-	0.3	10.8	0.6

analyzing the excited states and their properties, the Multiwfn software is used.

6.3 Results and discussion

6.3.1 Ground state structures and properties

Ground state geometries of donor oligomers significantly influence the optoelectronic properties.[114, 139, 182, 242, 243] Thus it is important to compare the molecular structures of π-bridged donors, with each other as well as with the parent system. Structures of optimized ground state geometries of **P1** to **TzP1** are shown in Figure 6.2. In the same figures, selected dihedral angles (ϕs) are also marked. Values of these dihedral angles are tabulated in the Table 6.3. As shown in the table, the value of ϕ_1 for the **P1** system is $\sim$21°, implying that the molecular skeleton of **P1** does not have good planarity. Having a planar geometry helps in absorbing more photons and in better π-π stacking. Insertion of π bridges results in three new dihedral angles; between the BDTT and π bridge units, between the π bridge and TT-F, and between TT-F and terminal π bridge units, in contrast to having only one between the BDTT and TT-F units in the case of **P1**. Comparing **FuP1** with **P1**, it is observed that the insertion of the furan units between donor and acceptor results in smaller angles for ϕ_2 and ϕ_3. But the dihedral angle at the terminus remains still large at $\sim$21°. In **TtP1** with thienothiophene as the bridge units, it was found that the ϕ_2, ϕ_3 and ϕ_4 values are 17.4°, 25.1° and 33.0°, respectively. In the case of **ThP1**, dihedral angle values of ϕ_2 and ϕ_3 are

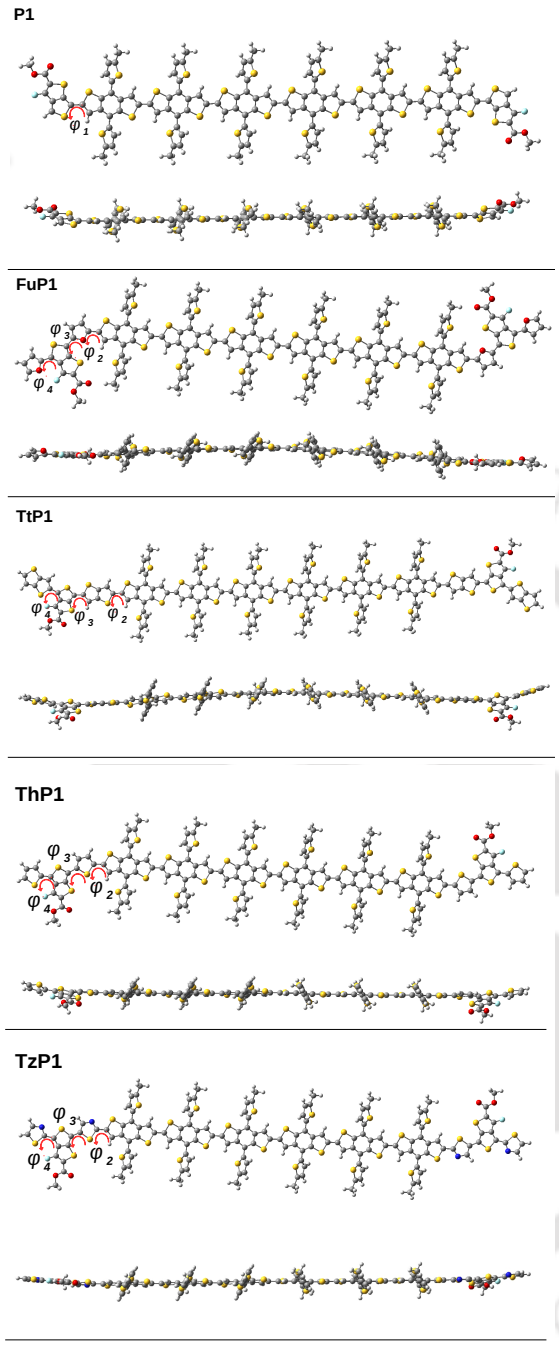

FIGURE 6.2: Optimized ground state geometries for **P1**-**TzP1** calculated at M06/6-311G(d,p) level.

smaller than those in **TtP1** but are still large at $\sim 10°$. On the other hand, in **TzP1** which contains the π-bridge thiazole units, the dihedral angles values ϕ_2 and ϕ_4 are almost zero. Our results for ϕ_2 and ϕ_4 showing increased rigidity and planarity of the backbone after insertion of thiazole π bridge are in accordance

with the reported results.[233, 244] Thiazole π bridge helps in through space non-covalent S....N interactions leading to conformational locks in the molecule. The corresponding N-S distances in our case are 3.04 Å and 2.91 Å, respectively, well within the van der Waals radii. On the other hand, the value of ϕ_3 between thiazole and TT-F unit is 10.8°. To check our results, relaxed torsional scans along the three dihedral angles were carried out and the results are shown in the Fig. D1 (see Appendix D). As shown, both ϕ_2 and ϕ_4 torsions show minima at zero degrees, but the minimum of the potential along ϕ_3 is obtained at ∼15°. The non-planarity at ϕ_3 is due to the steric interactions between the hydrogen atom of thiazole and the sulphur atom of TT-F.

6.3.2 Frontier molecular orbitals, open circuit voltages and energy losses

It is well known that processes such as stimulation, separation, and transfer of excitons are closely related to the HOMO and LUMO energy levels. Herein, we have analyzed the HOMO/LUMO levels of **FuP1** to **TzP1** oligomers when the π bridge units are inserted into the backbone. While furan, thienothiophene and thiophene are comparatively strong electron donors, thiazole is a weak electron-donor unit. In general, HOMO and LUMO energies increase in case of strong electron donor π bridges and for electron deficient bridges, values of these levels get lowered. Hou et al.[245] recently found that changing the π linker from furan to thiophene resulted in uplifted HOMO and downshifted LUMO levels, and eventually device prepared with thiophene based polymer showed higher performance than furan based polymers. This is similar to the results obtained by Wang et al.[206] whose cyclic voltametry studies showed the HOMO energies to increase while going from furan to thiophene and then to thienothiophene bridges. A recent study on a series of donor-acceptor-donor based π-conjugated small molecule model compounds reported that HOMO energies are dependent on the type of donor π unit.[235] With the same acceptor, the energies for HOMOs of π-bridged systems follow the order: furan > thiophene > thiazole. Zhou et al.[192, 231] have

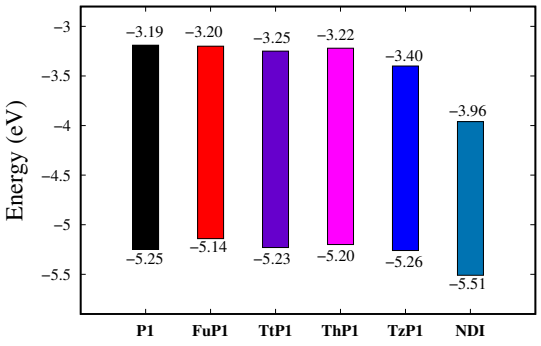

FIGURE 6.3: Calculated HOMO and LUMO energy levels of **P1-TzP1** and **NDI** at the M06/6-311G(d,p) level.

shown that a donor copolymer with thienothiophene as a π spacer shows higher V_{oc} and PCE than thiophene π bridge based device. This is attributed to downshifted HOMO energy, and better π-π stacking and higher crystallinity in case of thienothiophene bridged system which had a linear backbone conformation. Du et al.[208] synthesized thiophene and thienothiophene π bridge based polymers and the device prepared from thienothiophene bridged system produced a much higher PCE value, although there were minor differences in the HOMO and LUMO energies between the two polymers. Janssen and coworkers[236] synthesized polymers with donors BDTT/IDT and acceptor benzothiadiazole (BT) units linked via thiazole and thiophene linkers. Drastically downshifted frontier orbital levels, better planarity and smaller energy losses in case of thiazole π-bridged systems produced higher V_{oc}. From the above discussion, it can be concluded that the energies of HOMOs and LUMOs in π-bridged system vary depending on the types of donor and acceptor components of the molecule. In our case, calculated HOMO and LUMO energies of **P1-TzP1** are tabulated in Table 6.4 and are shown in Figure 6.3. The HOMO energies are in the following order: **FuP1** > **ThP1** > **TtP1** > **P1** > **TzP1**. **FuP1** with furan π bridge has the highest HOMO value which contradicts the results of Hou et al.[245] and Wang et al.[206], but matches with the results for model D-A-D compounds by Chochos et al.[235] **TzP1** having thiazole unit as the π bridge has the deepest HOMO value among all which matches with the reported results.[209–212, 236] Based on the above results, the donating strengths of the π bridge units are the following order: furan > thiophene > thienothiophene >

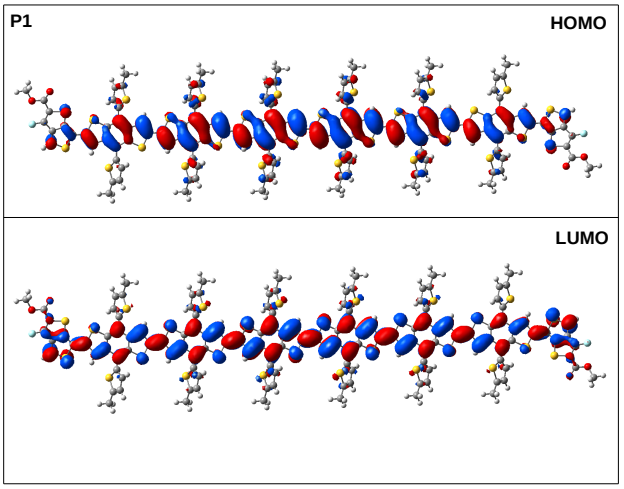

FIGURE 6.4: HOMO and LUMO of **P1** computed at the M06/6-311G(d,p) level (isovalue of 0.01 a.u.).

thiazole. The LUMO energy values are in the following order: **FuP1** > **ThP1** > **TtP1** > **TzP1** and this is again in accordance with the reported results.[235] Our results reveal that the π bridge units can adjust both the HOMO/LUMO levels. The calculated HOMO and LUMO levels of **NDI** are also shown in Figure 6.3 and it is clear that HOMO and LUMO energies of all the oligomers are suitably positioned with respect to the energy levels of the NF acceptor. The HOMO and LUMO for **P1** are shown in Figure 6.4. As shown, the HOMO and LUMO are distributed over the BDTT and TT-F units. For **FuP1**-**TtP1** and **ThP1**-**TzP1**, the distributions of frontier molecular orbitals are shown in Figures D2 and D3, respectively (see Appendix D). While the HOMO and LUMO are spread over the whole system for **FuP1**, there are negligible densities over the terminal acceptor and π bridge units for HOMOs of **TtP1**-**TzP1**. On the other hand, LUMOs are distributed over the entire molecule.

The calculated V_{oc} values of **P1** to **TzP1** are displayed in Table 6.4. As the table shows, the calculated value for **P1** is a little larger than the experimental result. Nonetheless, keeping in mind the DFT level of computations, we think that the order of V_{oc} values among different systems will remain the same. The obtained V_{oc} values are in the following order: **TzP1** (1.00 V) > **P1** (0.99 V) > **TtP1** (0.97 V) > **ThP1** (0.94 V) > **FuP1** (0.88 V). The thiazole π-bridged

TABLE 6.4: Energies of HOMO (E_{HOMO}) and LUMO (E_{LUMO}) of **P1-TzP1**, and acceptor **NDI2HD-T2**. Open-circuit voltages (V_{oc} in volt) and energy losses (E_{loss}) of all **P1-TzP1**. All the energies are in eV. Experimental V_{oc} for **P1** is 0.87 V.

Compounds	E_{HOMO}	E_{LUMO}	V_{oc}(V)	E_{loss}
P1	-5.25	-3.19	0.99	1.08
FuP1	-5.14	-3.20	0.88	1.07
TtP1	-5.23	-3.25	0.97	1.01
ThP1	-5.20	-3.22	0.94	1.04
TzP1	-5.26	-3.40	1.00	0.86
NDI2HD-T2	-5.51	-3.96		

dimer with almost a planar structure and the smallest HOMO energy produces the highest V_{oc}. **P1** having the second smallest HOMO value has the next highest V_{oc}.

One way to increase the PCE is to minimize the E_{loss}. For OPV cells the E_{loss} values are usually between 0.7 -1.1 eV.[160, 162, 164, 246] The calculated E_{loss} values are also tabulated in Table 6.4. It is observed that π-bridged oligomers have slightly smaller E_{loss} values than the value for **P1**. In addition, **TzP1** with the π bridge thiazole units has the smallest E_{loss} value among all systems because of its lowest E_{g}^{1} and highest V_{oc} value.

6.3.3 Absorption Properties

The simulated absorption spectra for **P1-TzP1** are shown in Figure 6.5. E_{g}^{1}s, λ_{max}s, f_{osc}s, percentage contributions of HOMO→LUMO transitions for the first excitations (C_{HL}), and η_{λ} are summarized in Table 6.5. All the absorption spectra are in the range 300-900 nm. Two absorption bands appear for all the systems except **TzP1** for which the high-energy band is almost merged with the low-energy band. Both the bands get red-shifted while going from **P1** to **TzP1**. The optical band gaps are 2.07 eV, 1.95 eV, 1.98 eV, 1.98 eV and 1.85 eV, for **P1-TzP1**, respectively. In comparison to **P1**, π bridge based oligomers **FuP1-TzP1** exhibit red-shifted E_{g}^{1}s. It is also observed that heights of low energy peaks for π bridge

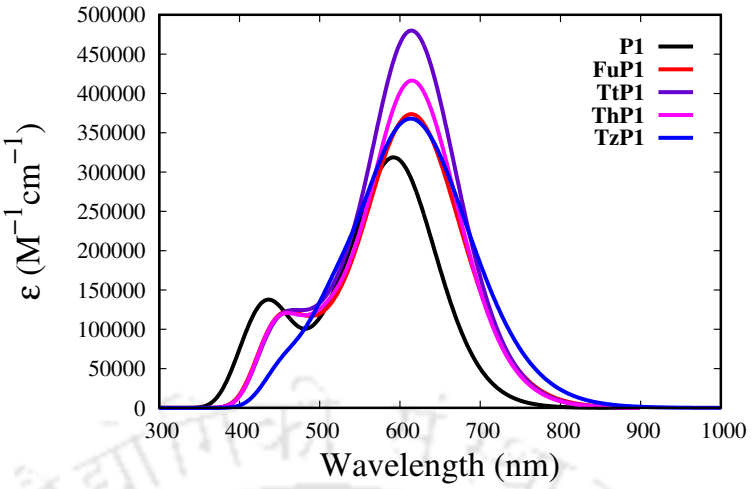

FIGURE 6.5: Simulated absorption spectra of **P1**-**TzP1** computed at the TD-PCM-HSE06/6-311G(d, p) level in the chloroform solvent. Half-width at half-maximum is 1500 cm^{-1}.

systems are higher than **P1**, and the integrated spectral areas of newly designed copolymers are broader than that of the parent molecule. Broader absorption spectra will facilitate more photon absorption and have a positive influence on the J_{sc} values. Hence, these π bridge based oligomers may significantly improve the J_{sc}. The $S_0 \rightarrow S_1$ transitions are dominated by the HOMO $\rightarrow$LUMO excitations for all the systems. The percentage contributions of HOMO $\rightarrow$LUMO transitions are 99%, 98%, 95%, 94%, and 99% for **P1**-**TzP1**, respectively. The calculated f_{osc} values are also tabulated in Table 6.5. It is observed that while **TtP1** has the highest f_{osc}, **TzP1** has the lowest value for $S_0 \rightarrow S_1$ transition. Smaller extinction coefficients for thiazole based systems are also reported in literature.[210] A set of

TABLE 6.5: First excitation energies (E_g^1 in eV), corresponding wavelengths (λ_{max} in nm), oscillator strengths (f_{osc}), contributions of HOMO to LUMO excitations for $S_0 \rightarrow S_1(C_{HL})$, light absorption efficiencies (η_λ) for **P1**-**TzP1**. The results are obtained at TD-PCM-HSE06/6-311G(d,p) level.

Compounds	E_g^1	λ_{max}	f_{osc}	C_{HL}	η_λ
P1	2.07	600	4.03	99%	0.999
FuP1	1.95	636	3.41	98%	0.999
TtP1	1.98	625	5.12	95%	0.999
ThP1	1.98	626	4.53	94%	0.999
TzP1	1.85	668	1.76	99%	0.983

transitions take part to form the high-energy bands in all the cases. For example, in the case of **P1**, the high-energy band arises due to $S_0 \rightarrow S_{16}$, S_{21}, S_{25} and S_{29} transitions. These transitions correspond to HOMO-2→LUMO+2, HOMO-1→LUMO+3, HOMO-7→LUMO, HOMO-4→LUMO+2 and HOMO-8→LUMO excitations. Similar observations are made in all the other cases too, but the heights of the high-energy bands of **FuP1-ThP1** are smaller than that of **P1**. η_λ values are calculated considering the $S_0 \rightarrow S_1$ transitions only. As shown in Table 6.5, **TzP1** has smaller η_λ value, in accordance with the f_{osc} values.

6.3.4 Properties of the P1-P5/NDI blend systems

The optimized structures of **P1-TzP1/NDI** complexes are shown in Figure D4 (see Appendix D). Literature shows that face-to-face π-stacking helps the most in increasing the electronic coupling and contributes largely to the charge transfer in the D/A system.[152, 247–250] Hence, we have considered face-to-face π-stacking geometries in our cases. Starting with an initial vertical distance of ∼3.5 Å, optimizations were carried out at PBE/def2-SV(P) level as mentioned already. The optimized geometries of the **P1/NDI** and **FuP1-TzP1/NDI** are quite similar and the optimized vertical distances between donors and acceptor are 3.5-4.0 Å. We have calculated the binding energies (ΔE_{BE}) of the blends as $\Delta E_{BE} = E_{blend}$ - (E_P+E_A), where E_{blend} is the energy of the dimer/non-fullerene blend, and E_P and E_A are the energies of the polymer and **NDI**, respectively. The ΔE_{BE} values of **P1-TzP1/NDI** are 1.76 eV, 1.55 eV, 1.72 eV, 1.55 eV, and 1.75 eV, respectively. It is observed that the **TzP1/NDI** complex has the highest ΔE_{BE} value amongst the newly designed systems indicating stronger interaction between the donor oligomer and the acceptor.

The HOMO and LUMO of **P1/NDI** are shown in the Figure 6.6. While the HOMO is distributed over the **P1** unit, the LUMO is delocalized over the **NDI**. For the blend systems **FuP1/NDI-TzP1/NDI**, the distributions of HOMOs and LUMOs are shown in Figure D5 (see Appendix D). Features similar to **P1/NDI** orbitals are also observed for these systems. These orbital plots suggest that the

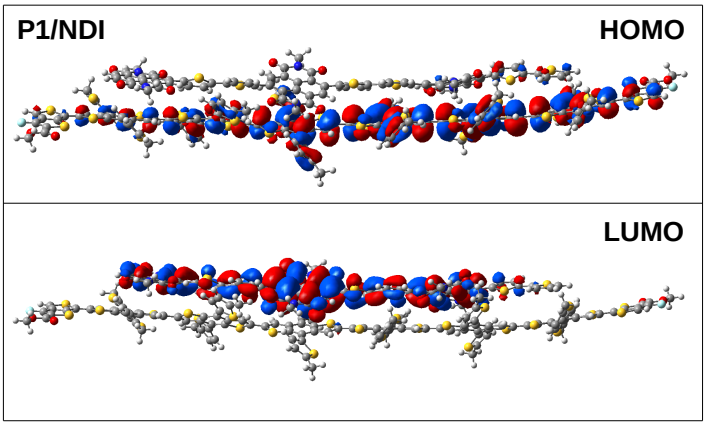

FIGURE 6.6: Plots of HOMOs and LUMOs for **P1**/**NDI** system computed at M06/6-311G(d,p) level.

changes in the π-π bonding pattern between dimers and **NDI** do not significantly impact the electronic structures. In addition, HOMO and LUMO density distributions also suggest that electronic excited states arising out of HOMO→LUMO excitations will be of charge transfer type.

The simulated absorption spectra for **P1**-**TzP1**/**NDI** are shown in Figure 6.7. The absorption spectral areas are in the range of 400-800 nm for all the blend

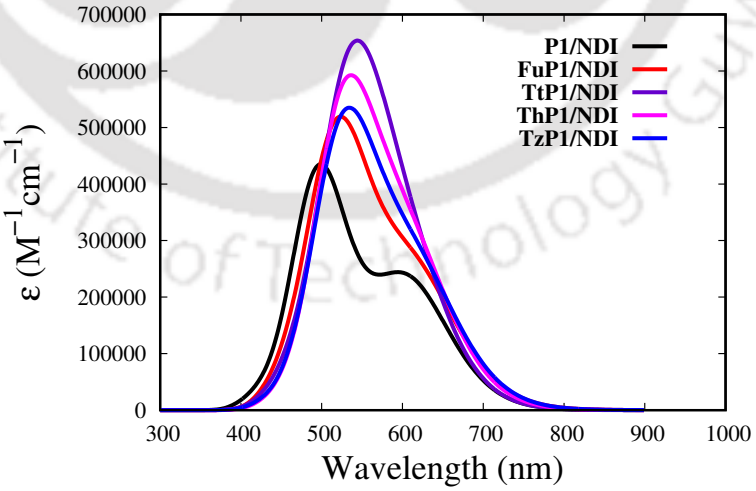

FIGURE 6.7: Simulated absorption spectra of **P1**-**TzP1**/**NDI** interfacial systems at the TD-PCM-CAMB3LYP/6-311G(d,p) level. Half-width at half-maximum is 1500 cm^{-1}.

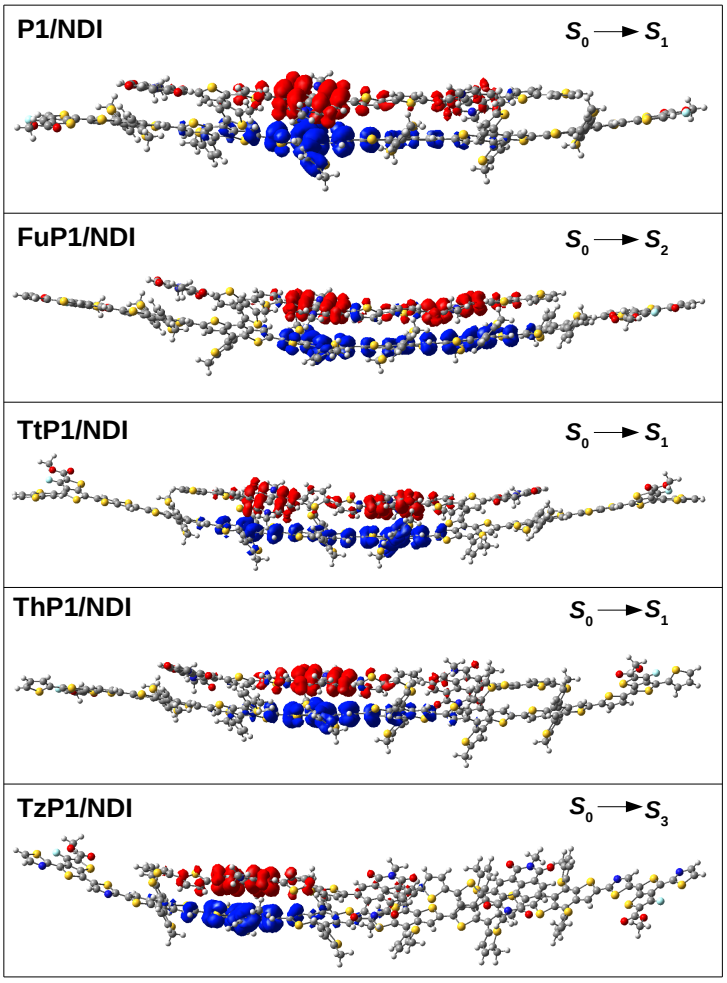

FIGURE 6.8: CDD plots for the S_1, S_2, S_1, S_1 and S_3 of the **P1-TzP1/NDI** interfacial systems. The mentioned states are the first ICT states.

systems. Each spectrum shows a high-energy band with a large f_{osc}, in addition to showing a low-energy band comprising of excitations with comparatively smaller f_{osc}s. It is to be noted that while for **P1** there is clear appearance of the low-energy band, the bands in this region for **FuP1-TzP1** appear as shoulders. The calculated λ_{max} values of **P1-TzP1/NDI** systems are 500 nm, 527 nm, 540 nm, 532, and 533 nm, respectively. This shows that the λ_{max} values of newly designed blends are close to each other, and these are red-shifted with respect to that of the parent blend system. Further, absorption peaks of **FuP1-TzP1/NDI** blend systems are higher than the **P1/NDI** indicating enhanced absorption capabilities.

TABLE 6.6: State numbers of first ICT states, first ICT excitation energies ($E^{\mathrm{ICT}}_{\mathrm{g,blend}}$) of the blends, corresponding f_{osc} and l^{CT} of all **P1-TzP1/NDI** systems.

Compounds	States	$E^{\mathrm{ICT}}_{\mathrm{g,blend}}$(eV)	f_{osc}	l^{CT}(Å)
P1/NDI	S_1	2.00	0.13	7.52
FuP1/NDI	S_2	2.02	0.70	7.45
TtP1/NDI	S_1	2.02	0.24	9.85
ThP1/NDI	S_1	1.95	0.17	7.10
TzP1/NDI	S_3	2.06	0.08	7.89

Following diffusion of the exciton along the polymer towards the heterojunction, exciton should be dissociated via charge transfer to form an ICT state. The ICT state can either get separated into free charges or recombine to form the donor ground state. Hence, the ICT states play very prominent roles in the overall process. As shown later, we calculate k_{CT} and k_{CR} to understand the effects of different π bridges on these observables. For this, as a first step, excited states at the interface were analyzed and ICT states were determined. In our study, we have considered only the first ICT state for each blend system. CDD plots were computed to determine the character of the states. The CDD plots for the first ICT states are shown in the Figure 6.8. As shown in the figure, S_1, S_2, S_1, S_1, and S_3 states are the first ICT states for **P1-TzP1/NDI** blend systems with the electrons and holes being localized on the donor and acceptor units, respectively. Excitation energies of the first ICT states ($E^{\mathrm{ICT}}_{\mathrm{g,blend}}$), corresponding f_{osc}s, and l^{CT} are listed in Table 6.6. The energies of the first ICT states are 2.00 eV, 2.02 eV, 2.02 eV, 1.95 eV, and 2.06 eV for **P1**, **FuP1**, **TtP1**, **ThP1** and **TzP1/NDI**, respectively. It is observed that f_{osc} values for the first ICT states of **FuP1-ThP1/NDI** are larger than the f_{osc} for **P1/NDI**. But in the case of **TzP1/NDI**, the value is the smallest. l^{CT} values for the first ICT of the five blend systems are 7.52 Å, 7.45 Å, 9.85 Å, 7.10 Å, 7.89 Å, respectively. A larger l^{CT} value indicates easier separability of the exciton to a hole and an electron. **TtP1/NDI** complex has the highest l^{CT} value among all showing that charge separation is easy in this case.

IPs, EAs, fundamental band gaps, $E^{1}_{\mathrm{g,Blend}}$ and E_{b} of **P1-TzP1/NDI** are

TABLE 6.7: Calculated ionization potential energies (IP in eV) and electron affinities (EA in eV), lowest excitation energies ($E^1_{g,Blend}$ in eV) of the blends, and exciton binding energies (E_b in eV) of all **P1-TzP1/NDI** systems.

Compounds	IP	EA	$E^1_{g,Blend}$	E_b
P1/NDI	5.65	2.96	2.00	0.69
FuP1/NDI	5.51	2.90	1.97	0.64
TtP1/NDI	5.55	2.96	2.02	0.57
ThP1/NDI	5.53	2.94	1.95	0.64
TzP1/NDI	5.64	2.97	1.98	0.69

tabulated in Table 6.7. Fundamental band gaps of newly designed complexes are smaller compared to the value for **P1/NDI**. The calculated $E^1_{g,Blend}$ values are 2.00 eV, 1.97 eV, 2.02 eV, 1.95 eV and 1.98 eV, respectively. This shows that **FuP1**, **ThP1**, and **TzP1** based blends have smaller optical gaps than of **P1**. The computed E_b values of **P1-TzP1/NDI** complexes are 0.69 eV, 0.64 eV, 0.57 eV, 0.64 eV, and 0.69 eV, respectively, which are not too far from typical experimental values.[105] It is observed that **FuP1-ThP1/NDI** complexes have smaller E_b values than the parent system. Due to its highest $E^1_{g,Blend}$ value, **TtP1/NDI** has the smallest E_b.

6.3.5 Intermolecular charge transfer and charge recombination rates

The computed λ values of **P1-TzP1/NDI**, as shown in the Table 6.8, are in 0.41-0.43 eV range. The newly designed systems have slightly smaller λ values than the parent molecule which is beneficial for device. As shown in Table 6.8, the $\Delta\mu$ values for **P1-TzP1/NDI** are 3.25 a.u., 3.63 a.u., 2.63 a.u., 3.42 a.u., and 4.68 a.u., respectively. Larger value of $\Delta\mu$ induces larger degree of polarizability and facilitates exciton dissociation. $\Delta\mu$ values of **FuP1/NDI**, **ThP1/NDI**, and **TzP1/NDI** blends are larger than that of **P1/NDI**. In particular, the $\Delta\mu$ value is greatly enhanced by inserting thiazole π bridge and **TzP1-NDI** has the highest $\Delta\mu$ which results in a better charge separation (a large l^{CT}value shown before).

TABLE 6.8: Differences in dipole moments between the ground and the excited states ($\Delta\mu$) and transition dipole moments (μ_{trans}) are in atomic units. Charge transfer integrals (V_{DA}), changes in Gibbs free energies during charge transfer-/charge recombination ($\Delta G_{CT/CR}$) and reorganization energies (λ) are in eV. Charge transfer (k_{CT}) and charge recombination rates (k_{CR}) are in s^{-1}.

Composite systems	$\Delta\mu$	$\lvert\mu_{trans}\rvert$	$\lvert V_{DA}\rvert$	λ	$\Delta G_{CT/CR}$	k_{CT}	k_{CR}
P1/NDI	3.25	1.42	0.66	0.43	-0.86/-1.90	1.69×10^{14}	6.32×10^{-6}
FuP1/NDI	3.63	3.75	0.91	0.41	-0.84/-1.76	2.69×10^{14}	3.49×10^{-3}
TtP1/NDI	2.63	2.07	0.17	0.42	-0.91/-1.64	2.87×10^{12}	7.78×10^{-1}
ThP1/NDI	3.42	1.78	0.14	0.42	-0.81/-1.81	1.50×10^{13}	1.80×10^{-5}
TzP1/NDI	4.68	1.19	0.47	0.41	-0.64/-1.90	1.65×10^{15}	7.40×10^{-8}

The calculated μ_{trans} and V_{DA} are also listed in Table 6.8. The $|V_{DA}|$ values for **P1**-**TzP1**/**NDI** are 0.66 eV, 0.91 eV, 0.17 eV, 0.14 eV, and 0.47 eV, respectively. It is observed that **FuP1**/**NDI** has the highest V_{DA}value among all the blends and this results in a high k_{CT} value. Thiophene and thienothiophene π-bridged blends have very small V_{DA} values compared to the others, producing k_{CT}s which are one/two orders of magnitude smaller than the other blends.

As shown in Table 6.8, all the ΔG_{CR} and ΔG_{CT} values are negative, indicating that the charge recombination and transfer processes are thermodynamically feasible in all the systems. The computed $|\Delta G_{CR}|$ values of **P1**-**TzP1**/**NDI** complexes are 1.90 eV, 1.76 eV, 1.64 eV, 1.81 eV, and 1.90 eV, respectively, showing that **FuP1**-**ThP1**/**NDI** complexes have smaller $|\Delta G_{CR}|$ values than the parent system. The values of $|\Delta G_{CT}|$ follow the order: **TzP1**/**NDI** < **ThP1**/**NDI** < **FuP1**/**NDI** < **P1**/**NDI** < **TtP1**/**NDI**. ΔG_{CR} is directly proportional to the IP value. Accordingly, **TzP1**/**NDI** blend with the smallest ΔG_{CR} value among **FuP1**-**TzP1**/**NDI**, and a smaller V_{DA} than **P1**/**NDI** has the smallest k_{CR} value. The calculated k_{CT} values are in the following sequence: **TzP1**/**NDI** > **FuP1**/**NDI** > **P1**/**NDI** > **ThP1**/**NDI** > **TtP1**/**NDI**. **TzP1**/**NDI** has the smallest value of $|\Delta G_{CT}|$. In addition, this $|\Delta G_{CT}|$ value is the closest to the corresponding λ value, and hence, **TzP1**/**NDI** has the highest value of k_{CT} among these blends. The above results show that **TzP1** can be considered to be a very promising candidate for obtaining a high PCE value because of high V_{oc}, large k_{CT}, and small k_{CR} values when blended with **NDI** acceptor.

6.3.6 Conclusions

In summary, we have studied effects of insertion of various π bridges such as furan, thienothiophene, thiophene, and thiazole units on the structural, optoelectronic and charge transfer properties of random BDTT-TTF oligomer/**NDI2HD-T2** blends. Thiazole π spacer-based **TzP1** oligomer has the deepest HOMO/LUMO levels among all the systems, and this results in the highest V_{oc}. All the newly designed oligomers have red-shifted absorption-peaks compared to the spectra of parent molecule. In addition, **FuP1**-**TzP1** oligomers have comparatively smaller E_{loss} values compared to the **P1** and **TzP1** has the lowest value.

Computed exciton binding energies show that π linker based systems have lower E_b values than the parent blend system. Furan and thiazole π bridge based molecules have relatively higher k_{CT} values compared to the parent blend. Calculations of rates of charge recombination showed that π bridge thiazole based complex has the lowest k_{CR} value among all the systems.

Chapter 7

Summary and conclusions

Over the past two decades, the field of organic photovolatics has grown rapidly to develop newer materials for improving efficiencies of the solar cells. Bulk heterojunction architecture based OSCs are promoted rapidly in recent times due to various advantages such as wide-area of materials selection, simple preparation procedure, light-weightness, low-cost, transparency and mechanical flexibility. In recent times, PCEs of 15-18% have been achieved. There are various ways to tune the optoelectronic and charge transport properties such as donor and acceptor material selection, side chain effects, halogenation and π-spacer are usually adopted. Computational studies, at this juncture, have been of great help to design molecules and understand the structure-property relationships at molecular level. In this thesis, structural, optoelectronic, charge transport and charge transfer properties of BDT based conjugated oligomers and small molecules are explored using DFT and TDDFT methods. BDT is a widely used donor system, and various structural modifications of this unit has provided a better understanding of the structure-property relationships. As acceptors, both fullerene and non-fullerene acceptors are used in our studies. Our studies figure out many essential relationships that will help to design the active layers with more probabilities of obtaining better efficiencies.

In *chapter 3*, structural, optoelectronic, and charge transport properties of twelve BDT-TAZ based conjugated oligomers are studied. It is observed that the substitutions by fluorine atoms lower the HOMO and LUMO energies, and this results in better V_{oc} values. In addition, hole and electron mobilities are increased after fluorine substitutions. Therefore, these fluorine substituted oligomers are better suited for active layer designing of OSCs.

In *chapter 4*, structural, optoelectronic, and charge transfer properties of halogenated small molecules based on BDT and their blends with **PCBM** are studied. Halogenation improves the V_{oc} values compared to the parent systems. In addition, E_{loss} values are found to be smaller in halogenated SMs. It is also observed that while k_{CT} values are larger in halogenated SMs/**PCBM** interfaces, the k_{CR} values are smaller than in the parent systems. Therefore, halogenation of these SMs is beneficial for OSC fabrication.

In *chapter 5*, effects of various π bridge units on structural, optoelectronic and charge transfer properties of BDTT-TT-F based oligomers and their blends with **PCBM** are studied in detail. The π bridge based oligomers produce broader absorption spectra compared to the parent molecule. It is observed that thiazole π bridge based system has the deepest HOMO level, and the highest V_{oc} value among all. In addition, it is also observed that k_{CR} values are smaller in thiophene and thiazole π-bridged based systems. These results indicate that thiophene and thiazole π bridges are expected to improve device performance.

In *chapter 6*, we have considered the random oligomers based on BDTT and their blend structures with a non-fullerene acceptor. In particular, effects of incorporation of π bridges on structural, optoelectronic and, charge transfer properties of these random oligomers are explored. A 3:1 ratio of BDTT and TT-F units is considered. Again furan, thienothiophene, thiophene, and thiazole units are inserted between the BDTT and TT-F units. It is observed that thiazole π bridge based random oligomer has the highest V_{oc}. In this case too, k_{CT} value is the largest and k_{CR} is the smallest in the thiazole/**NDI** based system. Therefore, thiazole π linker based random oligomer will be the most suitable for device applications.

Our findings in the thesis, based on DFT and TDDFT studies, has provided valuable insights into the impact of insertion of different π bridges and halogen substitutions on the optoelectronic properties of conjugated polymers. π bridges such as furan, thiophene, thienothiophene and thiazole show different behavior with regard to charge transfer and recombination at the interface. Similarly, type of halogen substitution has been shown to affect the rates of charge transfer.

Computational investigation of oligomeric materials is a guiding tool to discover of newer materials. With the results in this thesis, and the protocol provided, more BHJ systems can be studied to obtain optimal design of donor materials for high power conversion efficiency.

Finally, it is worth mentioning that all the studies in the thesis have been performed at DFT/TDDFT level. Keeping in mind that finding a proper functional to describe the ground and excited state properties is a cumbersome task, we would like to explore the applicability of wave function based methods such as CC2 for these types of oligomers. Although the computational cost of using wave function based methods is very high, smaller oligomers can be studied. Understanding the effect of relative orientations of the donor and acceptors on the properties is also necessary to provide a reliable guideline for future studies, and these studies can also be carried out at ab initio wave function level. In addition, we would also like to take studies further to include polymeric materials. The thesis reports the results of small molecules or oligomers coupled with either a fullerene or a non-fullerene acceptor. However, in typical BHJ devices, the polymers are large. Therefore, in future studies, it would be worth exploring the polymer/acceptor junctions using molecular dynamics simulation studies to have a thorough understanding of the working of the solar cell.

Bibliography

[1] S. C. Price, A. C. Stuart, L. Yang, H. Zhou and W. You, *J. Am. Chem. Soc.*, 2011, **133**, 4625–4631.

[2] W. Li, L. Yan, H. Zhou and W. You, *Chem. Mater.*, 2015, **27**, 6470–6476.

[3] M. A. Green, K. Emery, Y. Hishikawa and W. Warta, *Progr. Photovolt.: Res. Appl.*, 2010, **18**, 144–150.

[4] C. W. Tang, *Appl. Phys. Lett.*, 1986, **48**, 183–185.

[5] G. Yu, J. Gao, J. C. Hummelen, F. Wudl and A. J. Heeger, *Science*, 1995, **270**, 1789–1791.

[6] G. Yu and A. J. Heeger, *J. Appl. Phys.*, 1995, **78**, 4510–4515.

[7] Y. Cui, H. Yao, J. Zhang, K. Xian, T. Zhang, L. Hong, Y. Wang, Y. Xu, K. Ma, C. An, C. He, Z. Wei, F. Gao and J. Hou, *Adv. Mater.*, 2020, **32**, 1908205.

[8] D. Li, L. Zhu, X. Liu, W. Xiao, J. Yang, R. Ma, L. Ding, F. Liu, C. Duan, M. Fahlman and Q. Bao, *Adv. Mater.*, 2020, **32**, 2002344.

[9] H. Yao, Y. Cui, D. Qian, C. S. Ponseca Jr, A. Honarfar, Y. Xu, J. Xin, Z. Chen, L. Hong, B. Gao *et al.*, *J. Am. Chem. Soc.*, 2019, **141**, 7743–7750.

[10] Y. Cui, H. Yao, L. Hong, T. Zhang, Y. Xu, K. Xian, B. Gao, J. Qin, J. Zhang, Z. Wei and J. Hou, *Adv. Mater.*, 2019, **31**, 1808356.

[11] M. Scharber, D. Mühlbacher, M. Koppe, P. Denk, C. Waldauf, A. Heeger and C. Brabec, *Adv. Mater.*, 2006, **18**, 789–794.

[12] N. Bérubé, V. Gosselin, J. Gaudreau and M. Cote, *J. Phys. Chem. C*, 2013, **117**, 7964–7972.

[13] B. Qi and J. Wang, *Phys. Chem. Chem. Phys.*, 2013, **15**, 8972–8982.

[14] H. Yao, L. Ye, H. Zhang, S. Li, S. Zhang and J. Hou, *Chem. Rev.*, 2016, **116**, 7397–7457.

[15] J.-S. Wu, S.-W. Cheng, Y.-J. Cheng and C.-S. Hsu, *Chem. soc. Rev.*, 2015, **44**, 1113–1154.

[16] L. Dou, Y. Liu, Z. Hong, G. Li and Y. Yang, *Chem. Rev.*, 2015, **115**, 12633–12665.

[17] H. Chen, *Sci. China. Chem.*, 2019, 403–404.

[18] J. Yuan, Y. Zhang, L. Zhou, G. Zhang, H.-L. Yip, T.-K. Lau, X. Lu, C. Zhu, H. Peng, P. A. Johnson, M. Leclerc, Y. Cao, J. Ulanski, Y. Li and Y. Zou, *Joule*, 2019, **3**, 1140 – 1151.

[19] C. Lee, S. Lee, G.-U. Kim, W. Lee and B. J. Kim, *Chem. Rev.*, 2019, **119**, 8028–8086.

[20] X. Xu, K. Feng, Y. W. Lee, H. Y. Woo, G. Zhang and Q. Peng, *Adv. Funct. Mater.*, 2020, **30**, 1907570.

[21] J.-W. Ha, H. S. Kim, C. E. Song, H. J. Park and D.-H. Hwang, *J. Mater. Chem. C*, 2020, **8**, 12265–12271.

[22] X. Shengqiang, Z. Qianqian and Y. Wei, *Adv. Mater.*, 2017, **29**, 1601391–1601399.

[23] D. Liu, W. Zhao, S. Zhang, L. Ye, Z. Zheng, Y. Cui, Y. Chen and J. Hou, *Macromolecules*, 2015, **48**, 5172–5178.

[24] D. Qian, L. Ye, M. Zhang, Y. Liang, L. Li, Y. Huang, X. Guo, S. Zhang, Z. Tan and J. Hou, *Macromolecules*, 2012, **45**, 9611–9617.

[25] Y. Wu, Z. Li, W. Ma, Y. Huang, L. Huo, X. Guo, M. Zhang, H. Ade and J. Hou, *Adv. Mater.*, 2013, **25**, 3449–3455.

[26] X. Zhou, W. Tang, P. Bi, Z. Liu, W. Lu, X. Wang, X. Hao, W.-K. Wong and X. Zhu, *J. Mater. Chem. C*, 2019, **7**, 380–386.

[27] T. Wang, R. Sun, S. Xu, J. Guo, W. Wang, J. Guo, X. Jiao, J. Wang, S. Jia, X. Zhu *et al.*, *J. Mater. Chem. A*, 2019, **7**, 14070–14078.

[28] H. Huang, L. Yang, A. Facchetti and T. J. Marks, *Chem. Rev.*, 2017, **117**, 10291–10318.

[29] X. Guo, A. Facchetti and T. J. Marks, *Chem. Rev.*, 2014, **114**, 8943–9021.

[30] Z. Yi, S. Wang and Y. Liu, *Adv. Mater.*, 2015, **27**, 3589–3606.

[31] B. H. Smith, Q. Zhang, M. A. Kelly, J. H. Litofsky, D. Kumar, A. Hexemer, W. You and E. D. Gomez, *ACS Macro Lett.*, 2017, **6**, 1162–1167.

[32] Q. Zhang, L. Yan, X. Jiao, Z. Peng, S. Liu, J. J. Rech, E. Klump, H. Ade, F. So and W. You, *Chem. Mater.*, 2017, **29**, 5990–6002.

[33] P. Huang, J. Du, S. S. Gunathilake, E. A. Rainbolt, J. W. Murphy, K. T. Black, D. Barrera, J. W. Hsu, B. E. Gnade, M. C. Stefan *et al.*, *J. Mater. Chem. A*, 2015, **3**, 6980–6989.

[34] B. Kan, Q. Zhang, F. Liu, X. Wan, Y. Wang, W. Ni, X. Yang, M. Zhang, H. Zhang, T. P. Russell *et al.*, *Chem. Mater.*, 2015, **27**, 8414–8423.

[35] D. Patra, W. Budiawan, T.-Y. Huang, K.-H. Wei, P.-C. Wang, K.-C. Ho, M. Al-Hashimi and C.-W. Chu, *ACS Appl. Energy Mater.*, 2018, **1**, 3684–3692.

[36] G. P. Kini, S. J. Jeon and D. K. Moon, *Adv. Mater.*, 2020, **32**, 1906175.

[37] Y.-Q. Guo, Y. Wang, L.-C. Song, F. Liu, X. Wan, H. Zhang and Y. Chen, *Chem. Mater.*, 2017, **29**, 3694–3703.

[38] N. D. Eastham, A. S. Dudnik, B. Harutyunyan, T. J. Aldrich, M. J. Leonardi, E. F. Manley, M. R. Butler, T. Harschneck, M. A. Ratner, L. X. Chen *et al.*, *ACS Energy Lett.*, 2017, **2**, 1690–1697.

[39] Z. Maojie, G. Xia, Z. Shaoqing and H. Jianhui, *Adv. Mater.*, 2014, **26**, 1118–1123.

[40] Q. Fan, T. Liu, W. Gao, Y. Xiao, J. Wu, W. Su, X. Guo, X. Lu, C. Yang, H. Yan *et al.*, *J. Mater. Chem. A*, 2019, **7**, 15404–15410.

[41] S. Furukawa and T. Yasuda, *J. Mater. Chem. A*, 2019, **7**, 14806–14815.

[42] H. Meng, Y. Li, B. Pang, Y. Li, Y. Xiang, L. Guo, X. Li, C. Zhan and J. Huang, *ACS Appl. Mater. & Interfaces*, 2019, **12**, 2733–2742.

[43] H. Yao, J. Wang, Y. Xu, S. Zhang and J. Hou, *Acc. Chem. Res.*, 2020, **53**, 822–832.

[44] Z. Ji, X. Xu, G. Zhang, Y. Li and Q. Peng, *Nano Energy*, 2017, **40**, 214–223.

[45] S. A. and O. N. S., *Modern Quantum Chemistry: Introduction to advanced electronic structure theory*, Dover edition, 1996.

[46] C. Møller and M. S. Plesset, *Phys. Rev.*, 1934, **46**, 618–622.

[47] J. Schirmer, *Phys. Rev. A*, 1982, **26**, 2395–2416.

[48] A. B. Trofimov and J. Schirmer, *J. Phys. B: At., Mol. Opt. Phys.*, 1995, **28**, 2299–2324.

[49] O. Christiansen, H. Koch and P. Jørgensen, *Chem. Phys. Lett.*, 1995, **243**, 409–418.

[50] B. O. Roos, P. R. Taylor and P. E. Sigbahn, *Chem. Phys.*, 1980, **48**, 157–173.

[51] K. Andersson, P. A. Malmqvist, B. O. Roos, A. J. Sadlej and K. Wolinski, *J. Phys. Chem.*, 1990, **94**, 5483–5488.

[52] P. Hohenberg and W. Kohn, *Phys. Rev. E*, 1964, **136**, B864.

[53] P. J. Stephens, F. J. Devlin, C. F. Chabalowski and M. J. Frisch, *J. Chem. Phys.*, 1994, **98**, 11623–11627.

[54] A. D. Becke, *Phys. Rev. A*, 1988, **38**, 3098.

[55] C. Lee, W. Yang and R. G. Parr, *Phys. Rev. B*, 1988, **37**, 785–789.

[56] J. P. Perdew, M. Ernzerhof and K. Burke, *J. Chem. Phys.*, 1996, **105**, 9982–9985.

[57] A. V. Krukau, O. A. Vydrov, A. F. Izmaylov and G. E. Scuseria, *J. Chem. Phys.*, 2006, **125**, 224106.

[58] A. J. COHEN and N. C. HANDY, *Mol. Phys.*, 2001, **99**, 607–615.

[59] J.-D. Chai and M. Head-Gordon, *Phys. Chem. Chem. Phys.*, 2008, **10**, 6615–6620.

[60] J.-D. Chai and M. Head-Gordon, *J. Chem. Phys.*, 2008, **128**, 084106.

[61] O. A. Vydrov and G. E. Scuseria, *J. Chem. Phys.*, 2006, **125**, 234109.

[62] H. Iikura, T. Tsuneda, T. Yanai and K. Hirao, *J. Chem. Phys.*, 2001, **115**, 3540–3544.

[63] T. Yanai, D. P. Tew and N. C. Handy, *Chem. Phys. Lett.*, 2004, **393**, 51–57.

[64] S. Grimme, J. Antony, S. Ehrlich and H. Krieg, *J. Chem. Phys.*, 2010, **132**, 154104.

[65] H. Schröder, J. Hühnert and T. Schwabe, *J. Chem. Phys.*, 2017, **146**, 044115.

[66] S. Grimme, *J. Comput. Chem.*, 2004, **25**, 1463–1473.

[67] S. Grimme, *J. Comput. Chem.*, 2006, **27**, 1787–1799.

[68] S. Grimme, S. Ehrlich and L. Goerigk, *J. Comput. Chem.*, 2011, **32**, 1456–1465.

[69] U. Salzner, *Comput. Mol. Sci.*, 2014, **4**, 601–622.

[70] K. Burke, J. Werschnik and E. Gross, *J. Chem. Phys.*, 2005, **123**, 062206.

[71] E. Runge and E. K. Gross, *Phys. Rev. Lett.*, 1984, **52**, 997.

[72] R. van Leeuwen, *Phys. Rev. Lett.*, 1999, **82**, 3863–3866.

[73] C. A. Ullrich, *Time-Dependent Density-Functional Theory: Concepts and Applications*, OUP Oxford, 2011.

[74] R. A. Marcus, *J. Chem. Phys.*, 1956, **24**, 966–978.

[75] V. May and O. Kühn, *Charge and Energy Transfer Dynamics in Molecular Systems*, Wiley-VCH Verlag GmbH & Co. KGaA, 2011.

[76] K. F. Freed and J. Jortner, *J. Chem. Phys.*, 1970, **52**, 6272–6291.

[77] J. Jortner, *J. Chem. Phys.*, 1976, **64**, 4860–4867.

[78] N. R. Kestner, J. Logan and J. Jortner, *J. Phys. Chem.*, 1974, **78**, 2148–2166.

[79] J. Ulstrup and J. Jortner, *J. Chem. Phys.*, 1975, **63**, 4358–4368.

[80] S. F. Nelsen, S. C. Blackstock and Y. Kim, *J. Am. Chem. Soc.*, 1987, **109**, 677–682.

[81] J.-L. Brédas, D. Beljonne, V. Coropceanu and J. Cornil, *Chem. Rev.*, 2004, **104**, 4971–5004.

[82] V. Rühle, A. Lukyanov, F. May, M. Schrader, T. Vehoff, J. Kirkpatrick, B. Baumeier and D. Andrienko, *J. Chem. Theory Comput.*, 2011, **7**, 3335–3345.

[83] R. A. Marcus, *Rev. Mod. Phys.*, 1993, **65**, 599–610.

[84] T. Liu and A. Troisi, *J. Phys. Chem. C*, 2011, **115**, 2406–2415.

[85] T. Xu, W. Wang and S. Yin, *J. Phys. Chem. A*, 2018, **122**, 8957–8964.

[86] D. P. McMahon and A. Troisi, *J. Phys. Chem. Lett.*, 2010, **1**, 941–946.

[87] S. E. Koh, C. Risko, D. A. da Silva Filho, O. Kwon, A. Facchetti, J.-L. Brédas, T. J. Marks and M. A. Ratner, *Adv. Funct. Mater.*, 2008, **18**, 332–340.

[88] J. E. Norton and J.-L. Brédas, *J. Am. Chem. Soc.*, 2008, **130**, 12377–12384.

[89] S.-B. Li, Y.-A. Duan, Y. Geng, H.-B. Li, J.-Z. Zhang, H.-L. Xu, M. Zhang and Z.-M. Su, *Phys. Chem. Chem. Phys.*, 2014, **16**, 25799–25808.

[90] C. Leng, H. Qin, Y. Si and Y. Zhao, *J. Phys. Chem. C*, 2014, **118**, 1843–1855.

[91] S. Biswas, A. Pramanik, S. Pal and P. Sarkar, *J. Phys. Chem. C*, 2017, **121**, 2574–2587.

[92] M. Shavez and A. N. Panda, *Chem. Phys. Lett.*, 2020, **756**, 137810.

[93] Y. Li, T. Pullerits, M. Zhao and M. Sun, *J. Phys. Chem. C*, 2011, **115**, 21865–21873.

[94] R. J. Cave and M. D. Newton, *J. Chem. Phys.*, 1997, **106**, 9213–9226.

[95] R. J. Cave and M. D. Newton, *Chem. Phys. Lett.*, 1996, **249**, 15–19.

[96] R. S. Mulliken, *J. Am. Chem. Soc.*, 1950, **72**, 4493–4503.

[97] R. S. Mulliken, *J. Am. Chem. Soc.*, 1952, **74**, 811–824.

[98] N. S. Hush, *Electrochim. Acta*, 1968, **13**, 1005–1023.

[99] C. Creutz, M. D. Newton and N. Sutin, *J. Photochem. Photobiol., A*, 1994, **82**, 47–59.

[100] J. E. Subotnik, S. Yeganeh, R. J. Cave and M. A. Ratner, *J. Chem. Phys.*, 2008, **129**, 244101.

[101] D. Rehm and A. Weller, *Isr. J. Chem.*, 1970, **8**, 259–271.

[102] G. J. Kavarnos and N. J. Turro, *Chem. Rev.*, 1986, **86**, 401–449.

[103] Y. Yi, V. Coropceanu and J.-L. Brédas, *J. Am. Chem. Soc.*, 2009, **131**, 15777–15783.

[104] J.-L. Brédas, *Mater. Horiz.*, 2014, **1**, 17–19.

[105] T. M. Clarke and J. R. Durrant, *Chem. Rev.*, 2010, **110**, 6736–6767.

[106] X. Liu, W. Shen, R. He, Y. Luo and M. Li, *J. Phys. Chem. C*, 2014, **118**, 17266–17278.

[107] S. Biswas, A. Pramanik and P. Sarkar, *J. Phys. Chem. C*, 2018, **122**, 14296–14303.

[108] S. Qu, H. Wang, D. Mo, P. Chao, Z. Yang, L. Li, L. Tian, W. Chen and F. He, *Macromolecules*, 2017, **50**, 4962–4971.

[109] Q.-Q. Zhao, Zhi-Wenand Pan, S.-X. Wu, Y. Wu, M. Zhang, L. Zhao, T. Gao, Y. Geng and Z.-M. Su, *Theor. Chem. Acc.*, 2018, **137**, 51.

[110] M. L. Keshtov, S. A. Kuklin, A. R. Khokhlov, I. O. Konstantinov, N. V. Nekrasova, Z.-y. Xie, S. Biswas and G. D. Sharma, *New J. Chem.*, 2018, **42**, 1626–1633.

[111] G. Zhang, K. Zhang, Q. Yin, X.-F. Jiang, Z. Wang, J. Xin, W. Ma, H. Yan, F. Huang and Y. Cao, *J. Am. Chem. Soc.*, 2017, **139**, 2387–2395.

[112] Z. Du, X. Bao, Y. Li, D. Liu, J. Wang, C. Yang, R. Wimmer, L. W. Städe, R. Yang and D. Yu, *Adv. Energy Mater.*, 2018, **8**, 1701471.

[113] L. Ye, X. Jiao, H. Zhang, S. Li, H. Yao, H. Ade and J. Hou, *Macromolecules*, 2015, **48**, 7156–7163.

[114] Y.-L. Wang, Q.-S. Li and Z.-S. Li, *Phys. Chem. Chem. Phys.*, 2017, **19**, 23444–23453.

[115] Y.-L. Wang, Q.-S. Li and Z.-S. Li, *Phys. Chem. Chem. Phys.*, 2018, **20**, 14200–14210.

[116] Z. Fu, W. Shen, R. He, X. Liu, H. Sun, W. Yin and M. Li, *Phys. Chem. Chem. Phys.*, 2015, **17**, 2043–2053.

[117] M. Panneerselvam, A. Kathiravan, R. V. Solomon and M. Jaccob, *Phys. Chem. Chem. Phys.*, 2017, **19**, 6153–6163.

[118] Z. Fu, W. Shen, X. Tang, M. He, R. He and M. Li, *J. Phys. Chem. A*, 2015, **119**, 6884–6896.

[119] Q. Zhang, M. A. Kelly, N. Bauer and W. You, *Acc. Chem. Res.*, 2017, **50**, 2401–2409.

[120] X. Liu, C. Huang and M. Li, *J. Phys. Chem. C*, 2016, **120**, 27148–27158.

[121] J. E. Moussa, P. A. Schultz and J. R. Chelikowsky, *J. Chem. Phys.*, 2012, **136**, 204117.

[122] M. Niskanen and T. I. Hukka, *Phys. Chem. Chem. Phys.*, 2014, **16**, 13294–13305.

[123] P. Johari and S. P. Singh, *J. Phys. Chem. C*, 2015, **119**, 14890–14899.

[124] T. M. McCormick, C. R. Bridges, E. I. Carrera, P. M. DiCarmine, G. L. Gibson, J. Hollinger, L. M. Kozycz and D. S. Seferos, *Macromolecules*, 2013, **46**, 3879–3886.

[125] Y. Imamura, M. Tashiro, M. Katouda and M. Hada, *J. Phys. Chem. C*, 2017, **121**, 28275–28286.

[126] H. T. Turan, O. Kucur, B. Kahraman, S. Salman and V. Aviyente, *Phys. Chem. Chem. Phys.*, 2018, **20**, 3581–3591.

[127] M. J. Frisch, G. W. Trucks, H. B. Schlegel, G. E. Scuseria, M. A. Robb, J. R. Cheeseman, G. Scalmani, V. Barone, B. Mennucci, G. A. Petersson, H. Nakatsuji, M. Caricato, X. Li, H. P. Hratchian, A. F. Izmaylov, J. Bloino, G. Zheng, J. L. Sonnenberg, M. Hada, M. Ehara, K. Toyota, R. Fukuda, J. Hasegawa, M. Ishida, T. Nakajima, Y. Honda, O. Kitao, H. Nakai, T. Vreven, J. A. Montgomery, Jr., J. E. Peralta, F. Ogliaro, M. Bearpark, J. J. Heyd, E. Brothers, K. N. Kudin, V. N. Staroverov, R. Kobayashi, J. Normand, K. Raghavachari, A. Rendell, J. C. Burant, S. S. Iyengar, J. Tomasi, M. Cossi, N. Rega, J. M. Millam, M. Klene, J. E. Knox, J. B. Cross, V. Bakken, C. Adamo, J. Jaramillo, R. Gomperts, R. E. Stratmann, O. Yazyev, A. J. Austin, R. Cammi, C. Pomelli, J. W. Ochterski, R. L. Martin, K. Morokuma, V. G. Zakrzewski, G. A. Voth, P. Salvador, J. J. Dannenberg, S. Dapprich, A. D. Daniels, O. Farkas, J. B. Foresman,

J. V. Ortiz, J. Cioslowski and D. J. Fox, *Gaussian 09 Revision D.01*, 2009, Gaussian Inc. Wallingford CT 2009.

[128] X. Yang, L. Wang, C. Wang, W. Long and Z. Shuai, *Chem. Mater.*, 2008, **20**, 3205–3211.

[129] L. Wang, G. Duan, Y. Ji and H. Zhang, *J. Phys. Chem. C*, 2012, **116**, 22679–22686.

[130] H. Li, R. Zheng and Q. Shi, *J. Phys. Chem. C*, 2012, **116**, 11886–11894.

[131] W.-Q. Deng and W. A. Goddard, *J. Phys. Chem. B*, 2004, **108**, 8614–8621.

[132] V. Coropceanu, J. Cornil, D. A. da Silva Filho, Y. Olivier, R. Silbey and J.-L. Bredas, *Chem. Rev.*, 2007, **107**, 926–952.

[133] Y. A. Berlin, G. R. Hutchison, P. Rempala, M. A. Ratner and J. Michl, *J. Phys. Chem. A*, 2003, **107**, 3970–3980.

[134] H.-Y. Chen and I. Chao, *Chem. Phys. Lett.*, 2005, **401**, 539–545.

[135] Y.-K. Lan and C.-I. Huang, *J. Phys. Chem. B*, 2008, **112**, 14857–14862.

[136] H. Sahu and A. N. Panda, *Phys. Chem. Chem. Phys.*, 2014, **16**, 8563–8574.

[137] L. Wang, G. Nan, X. Yang, Q. Peng, Q. Li and Z. Shuai, *Chem. soc. Rev.*, 2010, **39**, 423–434.

[138] O. Kwon, V. Coropceanu, N. Gruhn, J. Durivage, J. Laquindanum, H. Katz, J. Cornil and J.-L. Bredas, *J. Chem. Phys.*, 2004, **120**, 8186–8194.

[139] X. Liu, M. Li, R. He and W. Shen, *Phys. Chem. Chem. Phys.*, 2014, **16**, 311–323.

[140] C. Risko, M. D. McGehee and J.-L. Bredas, *Chem. Sci.*, 2011, **2**, 1200–1218.

[141] T. Lu and F. Chen, *J. Comput. Chem.*, 2012, **33**, 580–592.

[142] X. Tang, X. Liu, W. Shen, W. Hu, R. He and M. Li, *RSC Adv.*, 2016, **6**, 102159–102171.

[143] S. Hedström, P. Henriksson, E. Wang, M. R. Andersson and P. Persson, *Phys. Chem. Chem. Phys.*, 2014, **16**, 24853–24865.

[144] A. Fradon, E. Cloutet, G. Hadziioannou, C. Brochon and F. Castet, *Chem. Phys. Lett.*, 2017, **678**, 9–16.

[145] M. E. Kose, W. J. Mitchell, N. Kopidakis, C. H. Chang, S. E. Shaheen, K. Kim and G. Rumbles, *J. Am. Chem. Soc.*, 2007, **129**, 14257–14270.

[146] R. Jin, X. Zhang, W. Xiao and D. Luo, *Int. J. Mol. Sci.*, 2017, **18**, 2178–2188.

[147] *TURBOMOLE V7.1 2016, a development of University of Karlsruhe and Forschungszentrum Karlsruhe GmbH, 1989-2007, TURBOMOLE GmbH, since 2007; available from* `http://www.turbomole.com`., 2016.

[148] M. Shavez, J. Goswami and A. N. Panda, *Comput. Theor. Chem.*, 2019, **1165**, 112564–112572.

[149] D. D. C. Rasi and R. A. J. Janssen, *Adv. Mater.*, 2019, **31**, 1806499.

[150] P. Yin, L. Wang, J. Liang, Y. Yu, L. Chen, C. Weng, C. Cui and P. Shen, *J. Mater. Chem. C*, 2020, **8**, 11223–11238.

[151] L. Meng, Y. Zhang, X. Wan, C. Li, X. Zhang, Y. Wang, X. Ke, Z. Xiao, L. Ding, R. Xia, H.-L. Yip, Y. Cao and Y. Chen, *Science*, 2018, **361**, 1094–1098.

[152] A. Abtahi, S. M. Mazza, S. M. Ryno, E. K. Loya, R. Li, S. R. Parkin, C. Risko, J. E. Anthony and K. R. Graham, *J. Phys. Chem. C*, 2018, **122**, 4757–4767.

[153] P. M. Beaujuge and J. M. Fréchet, *J. Am. Chem. Soc.*, 2011, **133**, 20009–20029.

[154] W. Ma, J. R. Tumbleston, M. Wang, E. Gann, F. Huang and H. Ade, *Adv. Energy Mater.*, 2013, **3**, 864–872.

[155] K. Budzinauskas, D. Fazzi, D. Hertel, S. Rüth, J. Schelter, P. Weitkamp, S. Diesing, K. Meerholz and P. H. van Loosdrecht, *J. Phys. Chem. C*, 2020, **124**, 21978–21984.

[156] J. R. Tumbleston, B. A. Collins, L. Yang, A. C. Stuart, E. Gann, W. Ma, W. You and H. Ade, *Nat. Photonics*, 2014, **8**, 385–391.

[157] Y. Zhang, J. Zou, C.-C. Cheuh, H.-L. Yip and A. K.-Y. Jen, *Macromolecules*, 2012, **45**, 5427–5435.

[158] K. Feng, X. Shen, Y. Li, Y. He, D. Huang and Q. Peng, *Polym. Chem.*, 2013, **4**, 5701–5710.

[159] J. Yao, T. Kirchartz, M. S. Vezie, M. A. Faist, W. Gong, Z. He, H. Wu, J. Troughton, T. Watson, D. Bryant and J. Nelson, *Phys. Rev. Appl.*, 2015, **4**, 014020.

[160] M. Wang, H. Wang, T. Yokoyama, X. Liu, Y. Huang, Y. Zhang, T.-Q. Nguyen, S. Aramaki and G. C. Bazan, *J. Am. Chem. Soc.*, 2014, **136**, 12576–12579.

[161] K. Vandewal, Z. Ma, J. Bergqvist, Z. Tang, E. Wang, P. Henriksson, K. Tvingstedt, M. R. Andersson, F. Zhang and O. Inganäs, *Adv. Funct. Mater.*, 2012, **22**, 3480–3490.

[162] D. Veldman, S. C. Meskers and R. A. Janssen, *Adv. Funct. Mater*, 2009, **19**, 1939–1948.

[163] Z. Wang, C. Song, J. Li, P. Li and H. Zhang, *J. Phys. Chem. C*, 2018, **123**, 1069–1081.

[164] A. Tang, B. Xiao, Y. Wang, F. Gao, K. Tajima, H. Bin, Z.-G. Zhang, Y. Li, Z. Wei and E. Zhou, *Adv. Funct. Mater.*, 2018, **28**, 1704507.

[165] R. Lenaerts, D. Devisscher, G. Pirotte, S. Gielen, S. Mertens, T. Cardeynaels, B. Champagne, L. Lutsen, D. Vanderzande, P. Adriaensens, P. Verstappen, K. Vandewal and W. Maes, *Dyes Pigm.*, 2020, **181**, 108577.

[166] C. Piliego, T. W. Holcombe, J. D. Douglas, C. H. Woo, P. M. Beaujuge and J. M. Fréchet, *J. Am. Chem. Soc.*, 2010, **132**, 7595–7597.

[167] J. Huang, Y. Zhao, W. He, H. Jia, Z. Lu, B. Jiang, C. Zhan, Q. Pei, Y. Liu and J. Yao, *Polym. Chem.*, 2012, **3**, 2832–2841.

[168] G. García, C. Adamo and I. Ciofini, *Phys. Chem. Chem. Phys.*, 2013, **15**, 20210.

[169] L. Huet, A. Perfetto, F. Muniz-Miranda, M. Campetella, C. Adamo and I. Ciofini, *J. Chem. Theory Comput.*, 2020, **16**, 4543.

[170] P. F. Barbara, T. J. Meyer and M. A. Ratner, *J. Phys. Chem.*, 1996, **100**, 13148–13168.

[171] M. Bixon and J. Jortner, in *Adv. Chem. Phys.*, 2007, pp. 35–202.

[172] J. Jortner, *J. Chem. Phys.*, 1976, **64**, 4860–4867.

[173] K. H. Hendriks, A. S. G. Wijpkema, J. J. van Franeker, M. M. Wienk and R. A. J. Janssen, *J. Am. Chem. Soc.*, 2016, **138**, 10026–10031.

[174] T. Unger, S. Wedler, F.-J. Kahle, U. Scherf, H. Bässler and A. Köhler, *J. Phys. Chem. C*, 2017, **121**, 22739–22752.

[175] Z. Zheng, N. R. Tummala, Y.-T. Fu, V. Coropceanu and J.-L. Brédas, *ACS Appl. Mater. & Interfaces*, 2017, **9**, 18095–18102.

[176] A. J. Ward, A. Ruseckas, M. M. Kareem, B. Ebenhoch, L. A. Serrano, M. Al-Eid, B. Fitzpatrick, V. M. Rotello, G. Cooke and I. D. Samuel, *Adv. Mater.*, 2015, **27**, 2496–2500.

[177] D. C. Coffey, B. W. Larson, A. W. Hains, J. B. Whitaker, N. Kopidakis, O. V. Boltalina, S. H. Strauss and G. Rumbles, *J. Phys. Chem. C*, 2012, **116**, 8916–8923.

[178] L. Cupellini, P. Wityk, B. Mennucci and J. Rak, *Phys. Chem. Chem. Phys.*, 2019, **21**, 4387–4393.

[179] Q.-Q. Pan, S.-B. Li, Y. Wu, G.-Y. Sun, Y. Geng and Z.-M. Su, *RSC Adv.*, 2016, **6**, 81164–81173.

[180] V. Lemaur, M. Steel, D. Beljonne, J.-L. Brédas and J. Cornil, *J. Am. Chem. Soc.*, 2005, **127**, 6077–6086.

[181] Z.-W. Zhao, Q.-Q. Pan, Y.-C. Duan, Y. Wu, Y. Geng, S.-X. Wu and Z.-M. Su, *J. Phys. Chem. C*, 2019, **123**, 6407–6415.

[182] H. Yin, Y. Geng, G.-Y. Sun and Z.-M. Su, *J. Phys. Chem. C*, 2017, **121**, 2125–2134.

[183] G. Sini, J. S. Sears and J.-L. Brédas, *J. Chem. Theory Comput.*, 2011, **7**, 602–609.

[184] Z.-Q. You, Y.-C. Hung and C.-P. Hsu, *J. Phys. Chem. B*, 2015, **119**, 7480–7490.

[185] O. J. J. Ronsin and J. Harting, *Ener. Tech.*, 2020, **8**, 1901468.

[186] H. Zhang, Y. Li, X. Zhang, Y. Zhang and H. Zhou, *Mater. Chem. Front.*, 2020, **4**, 2863–2880.

[187] A. M. Hiszpanski and Y.-L. Loo, *Energy. Environ. Sci.*, 2014, **7**, 592–608.

[188] H. I. Kim, M. Kim, C. W. Park, H. U. Kim, H.-K. Lee and T. Park, *Chem. Mater.*, 2017, **29**, 6793–6798.

[189] J. Chen and Y. Cao, *Acc. Chem. Res.*, 2009, **42**, 1709–1718.

[190] J. Yu, P. Chen, C. W. Koh, H. Wang, K. Yang, X. Zhou, B. Liu, Q. Liao, J. Chen, H. Sun, H. Y. Woo, S. Zhang and X. Guo, *Adv. Sci.*, 2018, 1801743.

[191] L. Yu, Y. Li, Y. Wang, X. Wang, W. Cui, S. Wen, N. Zheng, M. Sun and R. Yang, *ACS Appl. Mater. & Interfaces*, 2019, **11**, 31087–31095.

[192] Y. Chen, Y. Geng, A. Tang, X. Wang, Y. Sun and E. Zhou, *Chem. Comm.*, 2019, **55**, 6708–6710.

[193] K. Yang, X. Zhang, A. Harbuzaru, L. Wang, Y. Wang, C. Koh, H. Guo, Y. Shi, J. Chen, H. Sun, K. Feng, M. C. R. Delgado, H. Y. Woo, R. P. Ortiz and X. Guo, *J. Am. Chem. Soc.*, 2020, **142**, 4329–4340.

[194] M. Wang, X. Hu, P. Liu, W. Li, X. Gong, F. Huang and Y. Cao, *J. Am. Chem. Soc.*, 2011, **133**, 9638–9641.

[195] X. Guo, M. Zhang, L. Huo, F. Xu, Y. Wu and J. Hou, *J. Mater. Chem.*, 2012, **22**, 21024.

[196] X. Wang, P. Jiang, Y. Chen, H. Luo, Z. Zhang, H. Wang, X. Li, G. Yu and Y. Li, *Macromolecules*, 2013, **46**, 4805–4812.

[197] K. Lu, J. Fang, H. Yan, X. Zhu, Y. Yi and Z. Wei, *Org. Elec.*, 2013, **14**, 2652–2661.

[198] Y. Huang, X. Guo, F. Liu, L. Huo, Y. Chen, T. P. Russell, C. C. Han, Y. Li and J. Hou, *Adv. Mater.*, 2012, **24**, 3383–3389.

[199] L. Dou, W.-H. Chang, J. Gao, C.-C. Chen, J. You and Y. Yang, *Adv. Mater.*, 2012, **25**, 825–831.

[200] S. Liu, X. Bao, W. Li, K. Wu, G. Xie, R. Yang and C. Yang, *Macromolecules*, 2015, **48**, 2948–2957.

[201] D. Meng, D. Sun, C. Zhong, T. Liu, B. Fan, L. Huo, Y. Li, W. Jiang, H. Choi, T. Kim, J. Y. Kim, Y. Sun, Z. Wang and A. J. Heeger, *J. Am. Chem. Soc.*, 2015, **138**, 375–380.

[202] S. W. Kim, J. Choi, T. T. T. Bui, C. Lee, C. Cho, K. Na, J. Jung, C. E. Song, B. Ma, J.-Y. Lee, W. S. Shin and B. J. Kim, *Adv. Func. Mat.*, 2017, **27**, 1703070.

[203] R. A. Marcus, *Angew. Chem. Int. Ed.*, 1993, **32**, 1111–1121.

[204] M. Cossi, N. Rega, G. Scalmani and V. Barone, *J. Comput. Chem.*, 2003, **24**, 669–681.

[205] P. A. Denis, *New J. Chem.*, 2014, **38**, 5608–5616.

[206] X. Wang, Y. Sun, S. Chen, X. Guo, M. Zhang, X. Li, Y. Li and H. Wang, *Macromolecules*, 2012, **45**, 1208–1216.

[207] J. Liu, J. Ren, S. Zhang and J. Hou, *Polym. Chem.*, 2020, –.

[208] M. Du, Y. Chen, J. Li, Y. Geng, H. Ji, G. Li, A. Tang, Q. Guo and E. Zhou, *J. Phys. Chem. C*, 2019, **124**, 230–236.

[209] I. Bulut, P. Chávez, A. Mirloup, Q. Huaulmé, A. Hébraud, B. Heinrich, S. Fall, S. Méry, R. Ziessel, T. Heiser, P. Lévêque and N. Leclerc, *J. Mater. Chem. C*, 2016, **4**, 4296–4303.

[210] P. Josse, P. Chávez, C. Dindault, C. Dalinot, S. M. McAfee, S. Dabos-Seignon, D. Tondelier, G. Welch, P. Blanchard, N. Leclerc and C. Cabanetos, *Dyes Pigm.*, 2017, **137**, 576 – 583.

[211] E. Zaborova, P. Chávez, R. Bechara, P. Lévêque, T. Heiser, S. Méry and N. Leclerc, *Chem. Commun.*, 2013, **49**, 9938–9940.

[212] D. Zhu, X. Bao, Q. Zhu, C. Gu, M. Qiu, S. Wen, J. Wang, B. Shahid and R. Yang, *Energy Environ. Sci.*, 2017, **10**, 614–620.

[213] R. L. Martin, *J. Chem. Phys.*, 2003, **118**, 4775–4777.

[214] Z. Liao, K. Yang, L. Hou, J. Li, J. Lv, R. Singh, M. Kumar, Q. Chen, X. Dong, T. Xu *et al.*, *Macromolecules*, 2020, **53**, 9034–9042.

[215] Y. Du, H. Yao, L. Galuska, F. Ge, X. Wang, H. Lu, G. Zhang, X. Gu and L. Qiu, *Macromolecules*, 2019, **52**, 4765–4775.

[216] S. Zhang, L. Ma, L. Ye, Y. Qin, Y. Xu, X. Liu, Y. Wu, W. Zhao, H. Ade, H. Yao *et al.*, *Macromolecules*, 2019, **52**, 7929–7938.

[217] B. Xu, I. Pelse, S. Agarkar, S. Ito, J. Zhang, X. Yi, Y. Chujo, S. Marder, F. So and J. R. Reynolds, *ACS Appl. Energy Mater.*, 2018, **10**, 44583–44588.

[218] Q. Wang, Y. Wang, W. Zheng, B. Shahid, M. Qiu, D. Wang, D. Zhu and R. Yang, *ACS Appl. Energy Mater.*, 2017, **9**, 32126–32134.

[219] Q. Zhang, M. A. Kelly, A. Hunt, H. Ade and W. You, *Macromolecules*, 2016, **49**, 2533–2540.

[220] J. B. Howard, S. Ekiz, A. J. Cuellar De Lucio and B. C. Thompson, *Macromolecules*, 2016, **49**, 6360–6367.

[221] T. E. Kang, J. Choi, H.-H. Cho, S. C. Yoon and B. J. Kim, *Macromolecules*, 2016, **49**, 2096–2105.

[222] W. A. Braunecker, S. D. Oosterhout, Z. R. Owczarczyk, N. Kopidakis, E. L. Ratcliff, D. S. Ginley and D. C. Olson, *ACS Macro Lett.*, 2014, **3**, 622–627.

[223] Y. Zhang, Y. Shao, Z. Wei, L. Zhang, Y. Hu, L. Chen, S. Chen, Z. Yuan and Y. Chen, *ACS Appl. Mater. & Interfaces*, 2020, **12**, 20741–20749.

[224] H. Sun, T. Liu, J. Yu, T.-K. Lau, G. Zhang, Y. Zhang, M. Su, Y. Tang, R. Ma, B. Liu *et al.*, *Energy. Environ. Sci.*, 2019, **12**, 3328–3337.

[225] H. Yang, Y. Wu, Y. Dong, C. Cui and Y. Li, *ACS Appl. Mater. & Interfaces*, 2019, **11**, 40339–40346.

[226] W. Feng, Z. Lin, C. Lin, W. Wang and Q. Ling, *ACS Appl. Mater. & Interfaces*, 2019, **11**, 43441–43451.

[227] M. Hossain, M. A. Afroz, R. Garai and P. K. Iyer, *Sustainable Energy Fuels*, 2021, **5**, 874–879.

[228] Y. Chen, J. Liang, Y. Yu, L. Wang, C. Weng and P. Shen, *Org. Elec.*, 2021, **89**, 106015.

[229] P. Chao, M. Guo, Y. Zhu, H. Chen, M. Pu, H.-H. Huang, H. Meng, C. Yang and F. He, *Macromolecules*, 2020, **53**, 2893–2901.

[230] C. Chu, C. Ni, A. He and Y. Qin, *Synth. Met.*, 2020, **268**, 116509–116515.

[231] A. Tang, Q. Zhang, M. Du, G. Li, Y. Geng, J. Zhang, Z. Wei, X. Sun and E. Zhou, *Macromolecules*, 2019, **52**, 6227–6233.

[232] Y. Shi, Y. Tang, K. Yang, M. Qin, Y. Wang, H. Sun, M. Su, X. Lu, M. Zhou and X. Guo, *J. Mater. Chem. C*, 2019, **7**, 11142–11151.

[233] S. Yu, Y. Chen, L. Yang, P. Ye, J. Wu, J. Yu, S. Zhang, Y. Gao and H. Huang, *J. Mater. Chem. A*, 2017, **5**, 21674–21678.

[234] J. Yu, J. Yang, X. Zhou, S. Yu, Y. Tang, H. Wang, J. Chen, S. Zhang and X. Guo, *Macromolecules*, 2017, **50**, 8928–8937.

[235] C. L. Chochos, P. Chávez, I. Bulut, P. Lévêque, M. Spanos, E. Tatsi, A. Katsouras, A. Avgeropoulos, V. G. Gregoriou and N. Leclerc, *J. Chem. Phys.*, 2018, **149**, 124902.

[236] C. Duan, J. J. van Franeker, M. M. Wienk and R. A. Janssen, *Polym. Chem.*, 2016, **7**, 5730–5738.

[237] Y. Zhao and D. G. Truhlar, *J. Phys. Chem. A*, 2006, **110**, 13126–13130.

[238] J. Tomasi, B. Mennucci and R. Cammi, *Chem. Rev.*, 2005, **105**, 2999–3094.

[239] J. Ku, Y. Lansac and Y. H. Jang, *J. Phys. Chem. C*, 2011, **115**, 21508–21516.

[240] G. Zhang and C. B. Musgrave, *J. Phys. Chem. A*, 2007, **111**, 1554–1561.

[241] M. J. Frisch, G. W. Trucks, H. B. Schlegel, G. E. Scuseria, M. A. Robb, J. R. Cheeseman, G. Scalmani, V. Barone, B. Mennucci, G. A. Petersson, H. Nakatsuji, M. Caricato, X. Li, H. P. Hratchian, A. F. Izmaylov, J. Bloino, G. Zheng, J. L. Sonnenberg, M. Hada, M. Ehara, K. Toyota, R. Fukuda, J. Hasegawa, M. Ishida, T. Nakajima, Y. Honda, O. Kitao, H. Nakai, T. Vreven, J. A. Montgomery, Jr., J. E. Peralta, F. Ogliaro, M. Bearpark, J. J. Heyd, E. Brothers, K. N. Kudin, V. N. Staroverov, R. Kobayashi, J. Normand, K. Raghavachari, A. Rendell, J. C. Burant, S. S. Iyengar, J. Tomasi, M. Cossi, N. Rega, J. M. Millam, M. Klene, J. E. Knox, J. B. Cross, V. Bakken, C. Adamo, J. Jaramillo, R. Gomperts, R. E.

Stratmann, O. Yazyev, A. J. Austin, R. Cammi, C. Pomelli, J. W. Ochterski, R. L. Martin, K. Morokuma, V. G. Zakrzewski, G. A. Voth, P. Salvador, J. J. Dannenberg, S. Dapprich, A. D. Daniels, O. Farkas, J. B. Foresman, J. V. Ortiz, J. Cioslowski and D. J. Fox, *Gaussian 16 Revision C.01*, 2016, Gaussian Inc. Wallingford CT 2016.

[242] B. A. Jones, A. Facchetti, M. R. Wasielewski and T. J. Marks, *J. Am. Chem. Soc.*, 2007, **129**, 15259–15278.

[243] K. Sun, X. Tang, Y. Ran, R. He, W. Shen and M. Li, *Phys. Chem. Chem. Phys.*, 2018, **20**, 1664–1672.

[244] G. C. Welch, R. C. Bakus, S. J. Teat and G. C. Bazan, *J. Am. Chem. Soc.*, 2013, **135**, 2298–2305.

[245] J. Liu, J. Ren, S. Zhang and J. Hou, *Polym. Chem.*, 2020, **11**, 5019–5028.

[246] K. Kawashima, Y. Tamai, H. Ohkita, I. Osaka and K. Takimiya, *Nat. Communications*, 2015, **6**, 10085.

[247] S. M. Swick, W. Zhu, M. Matta, T. J. Aldrich, A. Harbuzaru, J. T. L. Navarrete, R. P. Ortiz, K. L. Kohlstedt, G. C. Schatz, A. Facchetti, F. S. Melkonyan and T. J. Marks, *Proc. Natl. Acad. Sci. U. S. A.*, 2018, **115**, E8341–E8348.

[248] G. Boschetto, M. Krompiec and C.-K. Skylaris, *J. Phys. Chem. C*, 2019, **123**, 25585–25595.

[249] Y. Imamura, M. Suganuma and M. Hada, *J. Phys. Chem. C*, 2019, **123**, 17678–17685.

[250] H. Feng, X. Song, Z. Zhang, R. Geng, J. Yu, L. Yang, D. Baran and W. Tang, *Adv. Funct. Mater.*, 2019, **29**, 1903269.

Appendices

Appendix A

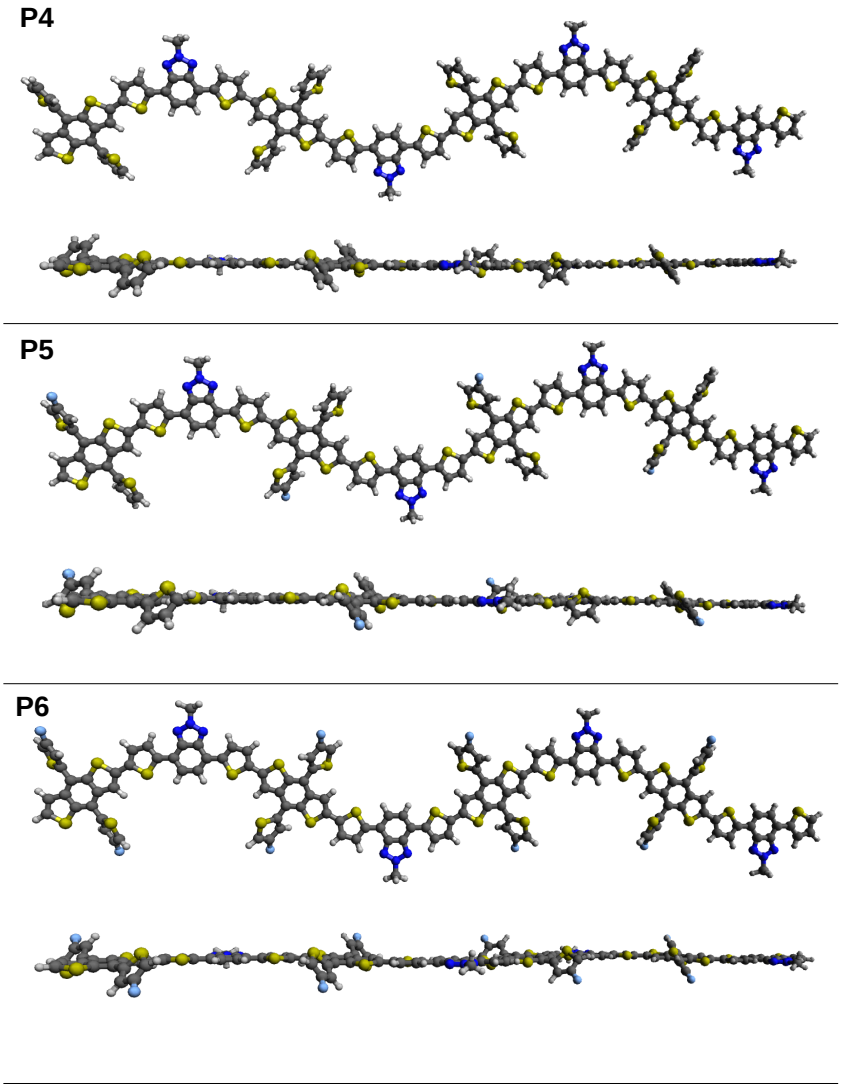

FIGURE A1: Optimized ground state geometries for tetramers of **P4-P6** calculated at HSE06/6-31G(d,p) level. Colour code: white (H), grey (C), yellow (S), blue (N) and cyan (F).

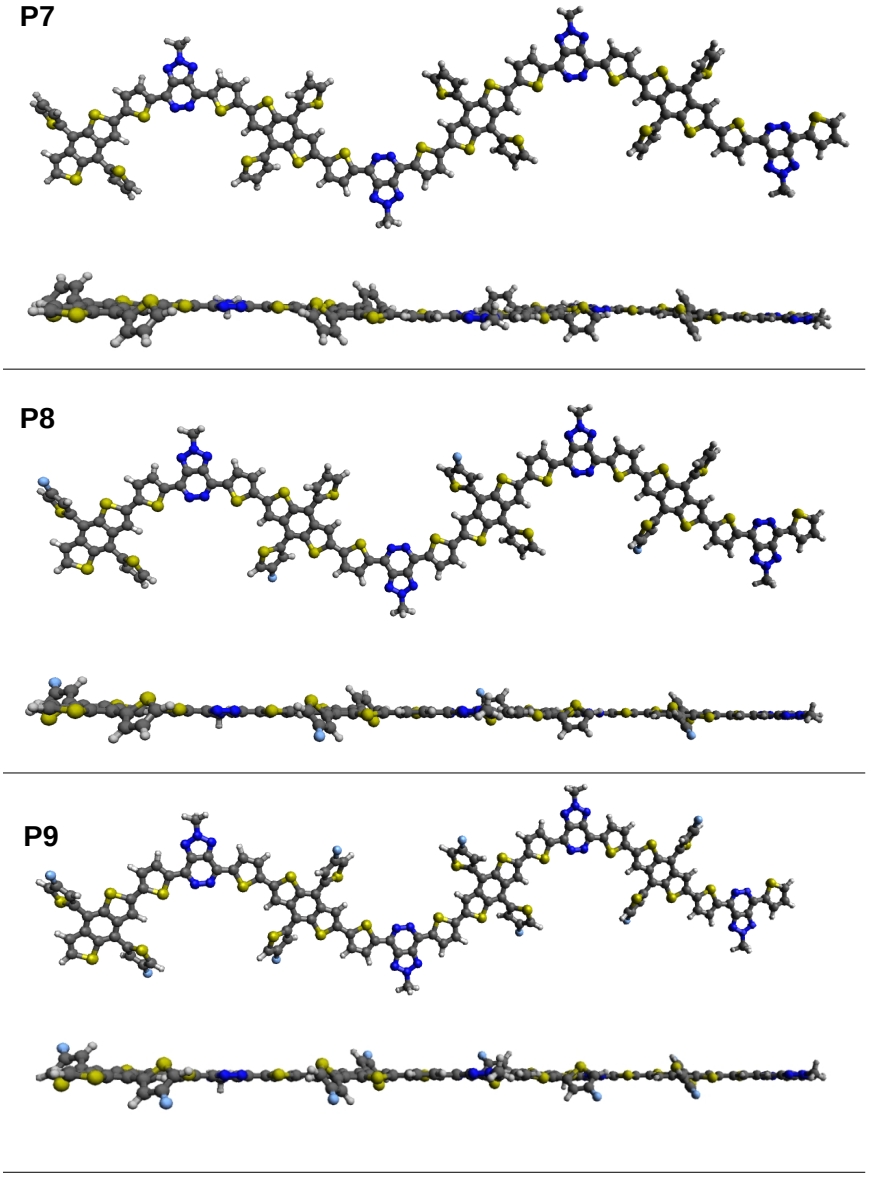

FIGURE A2: Optimized ground state geometries for tetramers of **P7**-**P9** calculated at HSE06/6-31G(d,p) level. Colour code: white (H), grey (C), yellow (S), blue (N) and cyan (F).

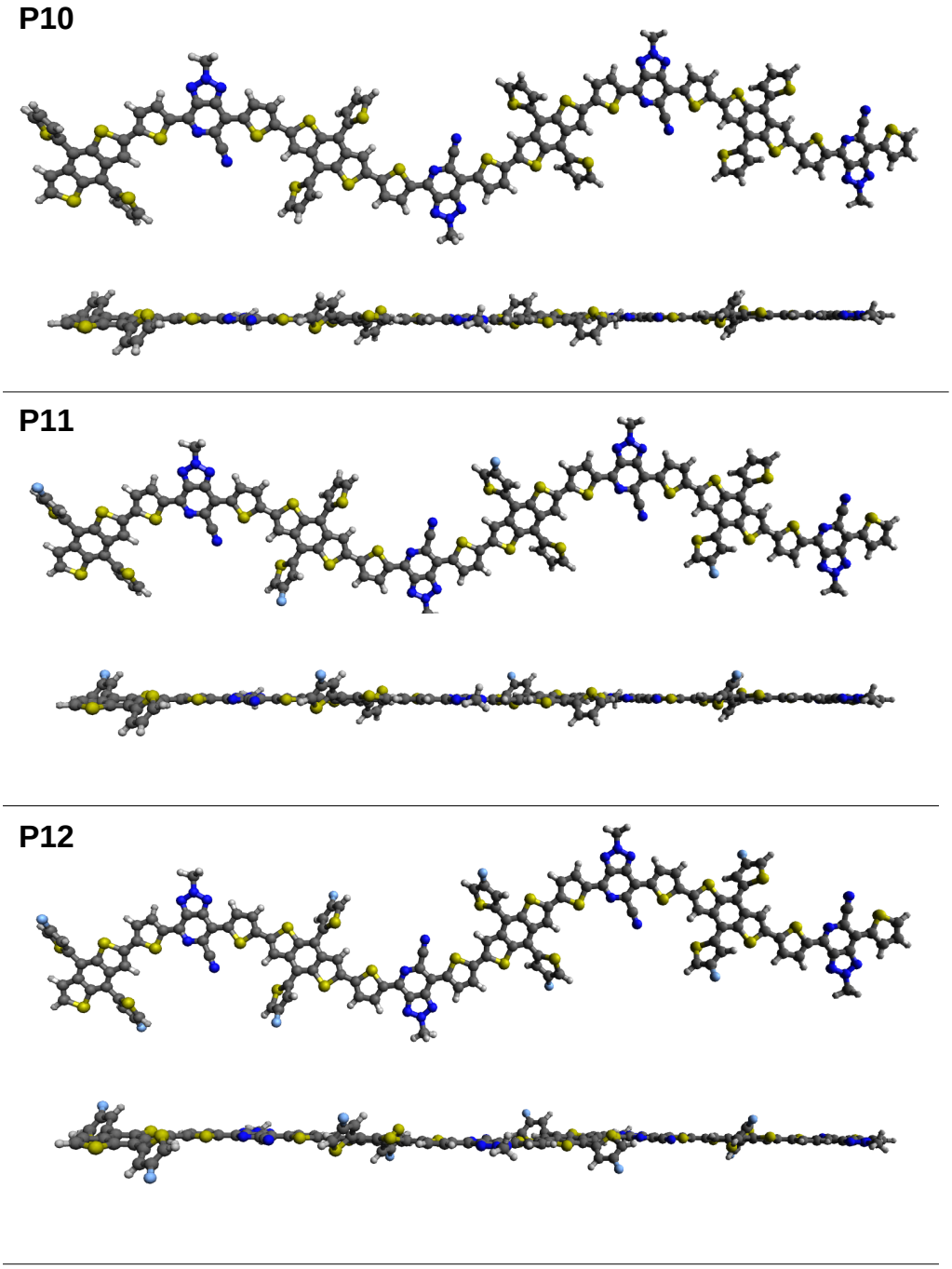

FIGURE A3: Optimized ground state geometries for tetramers of **P10**-**P12** calculated at HSE06/6-31G(d,p) level. Colour code: white (H), grey (C), yellow (S), blue (N) and cyan (F).

TABLE A1: Energies of the HOMOs (in eV) of all tetramer oligomers. Experimental energies are -5.29, -5.66 and -5.67 eV for **P1**, **P2** and **P3**, respectively. Considering **P1**, **P2** and **P3** only, the mean absolute errors are 0.84, 0.25, 0.40 and 1.30 for Models 1, 2, 3 and 4, respectively.

Compounds	Model 1	Model 2	Model 3	Model 4
P1	-4.55	-5.14	-5.06	-4.03
P2	-4.73	-5.33	-5.12	-4.27
P3	-4.81	-5.39	-5.22	-4.41
P4	-4.58	-5.15	-5.08	-4.02
P5	-4.65	-5.21	-5.15	-4.08
P6	-4.72	-5.28	-5.22	-4.15
P7	-4.76	-5.33	-5.14	-4.23
P8	-4.83	-5.40	-5.22	-4.29
P9	-4.91	-5.48	-5.23	-4.34
P10	-4.82	-5.38	-5.29	-4.36
P11	-4.90	-5.46	-5.38	-4.42
P12	-4.97	-5.53	-5.46	-4.49

TABLE A2: Energies of the LUMOs (in eV) of all tetramer oligomers. Experimental energies are -2.87, -3.73 and -3.83 eV for **P1**, **P2** and **P3**, respectively. Considering **P1**, **P2** and **P3** only, the mean absolute errors are 0.51, 1.09, 1.65, 1.93, 0.25 and 0.11, for Models 1, 2, 3, 4, 5 and 6, respectively.

Compounds	Model 1	Model 2	Model 3	Model 4	Model 5	Model 6
P1	-2.74	-2.16	-1.60	-1.57	-3.07	-3.15
P2	-3.00	-2.41	-1.84	-1.58	-3.20	-3.41
P3	-3.16	-2.58	-2.03	-1.49	-3.39	-3.54
P4	-2.77	-2.20	-1.65	-1.58	-3.09	-3.16
P5	-2.84	-2.27	-1.72	-1.58	-3.16	-3.22
P6	-2.91	-2.33	-1.79	-1.58	-3.23	-3.29
P7	-3.00	-2.42	-1.87	-1.60	-3.20	-3.38
P8	-3.07	-2.48	-1.93	-1.61	-3.27	-3.45
P9	-3.13	-2.54	-1.99	-1.62	-3.34	-3.52
P10	-3.15	-2.59	-2.04	-1.51	-3.37	-3.51
P11	-3.22	-2.64	-2.10	-1.55	-3.37	-3.57
P12	-3.28	-2.70	-2.19	-1.53	-3.51	-3.64

TABLE A3: Bond lengths, L_is (in Å), of the optimized structures of all oligomers in their neutral ground states obtained at HSE06/6-31G(d,p) level. L_1-L_{15} are shown in Figure 1.

$n=1$	**P1**	**P2**	**P3**	**P4**	**P5**	**P6**	**P7**	**P8**	**P9**	**P10**	**P11**	**P12**
L_1	1.43	1.44	1.44	1.44	1.43	1.44	1.44	1.44	1.43	1.44	1.44	1.44
L_2	1.44	1.43	1.44	1.44	1.44	1.44	1.43	1.43	1.44	1.44	1.44	1.44
L_3	1.45	1.44	1.45	1.44	1.45	1.45	1.45	1.44	1.44	1.45	1.45	1.45
$n=2$	**P1**	**P2**	**P3**	**P4**	**P5**	**P6**	**P7**	**P8**	**P9**	**P10**	**P11**	**P12**
L_1	1.43	1.44	1.43	1.44	1.43	1.44	1.44	1.44	1.43	1.44	1.44	1.44
L_2	1.44	1.43	1.44	1.44	1.44	1.44	1.43	1.43	1.44	1.44	1.44	1.44
L_3	1.44	1.44	1.44	1.44	1.44	1.44	1.43	1.44	1.44	1.43	1.43	1.44
L_4	1.44	1.44	1.43	1.44	1.43	1.44	1.44	1.44	1.43	1.44	1.44	1.44
L_5	1.43	1.43	1.44	1.44	1.44	1.44	1.43	1.43	1.44	1.44	1.44	1.44
L_6	1.44	1.44	1.44	1.44	1.44	1.44	1.44	1.44	1.44	1.44	1.43	1.44
L_7	1.45	1.44	1.45	1.44	1.45	1.45	1.45	1.44	1.44	1.45	1.45	1.45
$n=3$	**P1**	**P2**	**P3**	**P4**	**P5**	**P6**	**P7**	**P8**	**P9**	**P10**	**P11**	**P12**
L_1	1.43	1.44	1.43	1.44	1.43	1.44	1.44	1.44	1.43	1.44	1.44	1.44
L_2	1.44	1.43	1.44	1.44	1.44	1.44	1.43	1.43	1.44	1.44	1.44	1.44
L_3	1.44	1.44	1.44	1.44	1.44	1.44	1.44	1.44	1.44	1.44	1.43	1.44
L_4	1.43	1.44	1.43	1.44	1.43	1.44	1.44	1.44	1.43	1.44	1.44	1.44
L_5	1.44	1.43	1.44	1.44	1.44	1.44	1.43	1.43	1.44	1.44	1.44	1.44
L_6	1.44	1.44	1.44	1.44	1.44	1.44	1.43	1.44	1.44	1.44	1.43	1.44
L_7	1.44	1.44	1.44	1.43	1.44	1.44	1.44	1.44	1.44	1.44	1.43	1.44
L_8	1.43	1.44	1.43	1.44	1.43	1.44	1.44	1.44	1.43	1.44	1.44	1.44
L_9	1.44	1.43	1.44	1.44	1.44	1.44	1.43	1.43	1.44	1.44	1.44	1.44
L_{10}	1.44	1.44	1.44	1.44	1.44	1.43	1.44	1.44	1.44	1.44	1.43	1.44
L_{11}	1.45	1.44	1.45	1.44	1.45	1.45	1.45	1.44	1.44	1.45	1.44	1.45
$n=4$	**P1**	**P2**	**P3**	**P4**	**P5**	**P6**	**P7**	**P8**	**P9**	**P10**	**P11**	**P12**
L_1	1.43	1.44	1.43	1.44	1.43	1.44	1.44	1.44	1.43	1.44	1.44	1.44
L_2	1.44	1.43	1.44	1.44	1.44	1.44	1.43	1.43	1.44	1.44	1.44	1.44
L_3	1.44	1.44	1.44	1.44	1.44	1.44	1.44	1.44	1.44	1.44	1.43	1.44
L_4	1.43	1.44	1.43	1.44	1.43	1.44	1.44	1.44	1.43	1.44	1.44	1.44
L_5	1.44	1.43	1.44	1.44	1.44	1.44	1.43	1.43	1.44	1.44	1.44	1.44
L_6	1.44	1.44	1.44	1.44	1.44	1.44	1.43	1.44	1.44	1.44	1.43	1.44
L_7	1.44	1.44	1.44	1.44	1.44	1.44	1.44	1.44	1.44	1.44	1.43	1.44
L_8	1.43	1.44	1.43	1.44	1.43	1.44	1.44	1.44	1.43	1.44	1.44	1.44
L_9	1.44	1.43	1.44	1.44	1.44	1.44	1.43	1.43	1.44	1.44	1.44	1.44
L_{10}	1.44	1.44	1.44	1.44	1.43	1.44	1.43	1.44	1.44	1.44	1.43	1.44
L_{11}	1.44	1.44	1.44	1.44	1.44	1.44	1.44	1.44	1.44	1.44	1.43	1.44
L_{12}	1.43	1.44	1.43	1.44	1.43	1.44	1.44	1.44	1.43	1.44	1.44	1.44
L_{13}	1.44	1.43	1.44	1.44	1.44	1.44	1.43	1.43	1.44	1.44	1.44	1.44
L_{14}	1.44	1.44	1.44	1.44	1.43	1.44	1.44	1.44	1.44	1.44	1.43	1.44
L_{15}	1.45	1.44	1.45	1.44	1.45	1.45	1.45	1.44	1.44	1.45	1.44	1.45

TABLE A4: Selected dihedral angles(ϕ (deg)) of the optimized structures of all oligomers in their neutral ground states at HSE06/6-31G(d,p) level. ϕ_1-ϕ_{15} are seen in Figure 1.

$n=1$	**P1**	**P2**	**P3**	**P4**	**P5**	**P6**	**P7**	**P8**	**P9**	**P10**	**P11**	**P12**
ϕ_1	2.87	2.38	2.31	-10.19	-9.72	-9.07	-11.03	-10.34	-10.95	11.00	9.93	11.16
ϕ_2	-0.04	-0.05	-0.05	1.74	2.05	1.87	0.42	0.44	0.40	-0.26	-0.32	-0.24
ϕ_3	-0.50	-0.03	-1.13	-0.49	-0.48	-0.35	-0.04	-0.39	-0.06	-0.67	-0.96	-1.06
$n=2$	**P1**	**P2**	**P3**	**P4**	**P5**	**P6**	**P7**	**P8**	**P9**	**P10**	**P11**	**P12**
ϕ_1	0.96	1.32	0.14	-10.09	-9.62	-9.51	-10.88	-10.41	-10.82	-10.05	-10.73	-10.73
ϕ_2	0.22	0.00	0.00	2.14	1.98	2.09	0.38	0.36	0.32	0.44	0.49	0.49
ϕ_3	-0.81	-0.12	-0.81	-0.43	-0.54	-0.86	-0.03	-0.04	-0.11	0.93	0.21	0.21
ϕ_4	3.45	1.12	0.62	-0.02	-1.02	1.36	-2.10	-2.11	0.82	-10.38	-7.18	-7.18
ϕ_5	2.96	1.17	0.43	-3.47	-1.25	-1.31	-2.43	-0.06	2.40	10.00	10.36	10.36
ϕ_6	-0.10	-0.04	-0.10	0.46	0.18	0.09	-0.03	-0.07	-0.03	-0.12	0.24	-0.24
ϕ_7	-0.30	0.03	-0.82	-0.46	-0.43	-0.39	0.01	0.00	0.00	-1.19	-0.61	-0.61
$n=3$	**P1**	**P2**	**P3**	**P4**	**P5**	**P6**	**P7**	**P8**	**P9**	**P10**	**P11**	**P12**
ϕ_1	1.44	2.06	0.14	-10.70	-9.20	-8.88	-11.44	-9.93	-10.17	-10.92	-10.73	-10.84
ϕ_2	0.00	-0.03	0.00	1.84	1.89	2.02	0.38	0.38	0.35	0.37	0.49	0.38
ϕ_3	-0.59	-0.10	-0.01	-0.60	-2.05	-1.95	-0.13	-0.06	-0.09	0.21	0.21	-0.18
ϕ_4	1.39	1.19	0.63	-1.20	8.71	7.91	-0.57	-1.05	0.96	-7.18	-8.18	-8.67
ϕ_5	0.88	1.28	0.44	-2.28	-7.98	-7.44	-0.06	0.69	0.86	10.36	10.30	10.07
ϕ_6	0.00	-0.07	-0.11	0.26	1.60	1.81	0.00	-0.09	-0.11	0.24	-0.25	-0.073
ϕ_7	-0.56	-0.01	-0.82	-1.61	-1.69	-1.53	-0.05	-0.11	-0.20	-0.61	-0.57	-0.12
ϕ_8	1.72	1.05	1.28	1.28	8.79	8.16	9.87	9.46	8.22	10.12	10.94	11.01
ϕ_9	0.51	0.42	0.32	-9.33	-8.24	-7.97	-9.89	-9.03	-9.40	-10.73	-10.73	-10.44
ϕ_{10}	0.21	0.02	-0.04	1.98	1.93	2.04	0.39	0.43	0.38	0.49	0.49	0.39
ϕ_{11}	-0.45	-0.06	-0.25	-0.34	-0.32	-0.28	-0.05	-0.05	-0.04	0.21	0.21	-0.22
$n=4$	**P1**	**P2**	**P3**	**P4**	**P5**	**P6**	**P7**	**P8**	**P9**	**P10**	**P11**	**P12**
ϕ_1	-0.04	1.00	0.14	-11.08	-8.46	-8.03	-10.32	-10.13	-10.35	-11.06	-10.15	-11.05
ϕ_2	0.11	0.00	0.00	1.70	2.11	2.31	0.48	0.41	0.42	0.41	0.47	0.41
ϕ_3	-0.44	-0.10	-0.81	2.34	-1.80	-1.64	-0.33	-0.39	-0.36	0.72	0.22	0.51
ϕ_4	0.62	0.47	0.62	8.81	8.94	8.39	9.94	9.50	8.94	-10.16	-10.91	-10.19
ϕ_5	0.00	0.72	0.43	-9.21	-8.66	-8.42	-9.35	-8.38	-8.54	9.49	10.36	10.36
ϕ_6	0.09	-0.06	-0.11	1.33	1.41	1.53	0.11	0.10	0.12	-0.15	0.24	0.24
ϕ_7	-0.48	-0.02	-0.82	-1.89	-1.95	-1.87	-0.08	-0.09	-0.06	-1.28	-0.60	-0.60
ϕ_8	0.89	1.11	1.28	8.20	8.45	7.63	9.61	9.86	9.49	10.46	11.12	11.19
ϕ_9	0.31	0.70	0.32	-9.45	-7.92	-7.51	-9.47	-9.20	-9.47	-10.52	-10.73	-10.73
ϕ_{10}	0.17	-0.04	0.06	1.88	1.97	2.21	0.50	0.40	0.37	0.31	0.49	0.49
ϕ_{11}	-0.41	-0.12	-0.25	-1.95	-1.85	-1.66	-0.30	-0.36	-0.37	0.43	0.20	0.21
ϕ_{12}	0.86	0.76	-1.32	9.34	9.22	8.88	10.64	10.06	8.86	-10.46	-7.18	-7.18
ϕ_{13}	0.40	0.88	-2.68	-9.07	-8.17	-7.94	-9.80	-8.79	-9.14	9.63	10.36	10.36
ϕ_{14}	0.08	-0.06	-0.15	1.73	1.71	1.78	0.09	0.13	0.09	-0.17	0.24	0.24
ϕ_{15}	-0.36	0.01	-4.49	-0.25	-0.27	-0.25	0.02	0.02	0.02	-0.91	-0.61	0.11

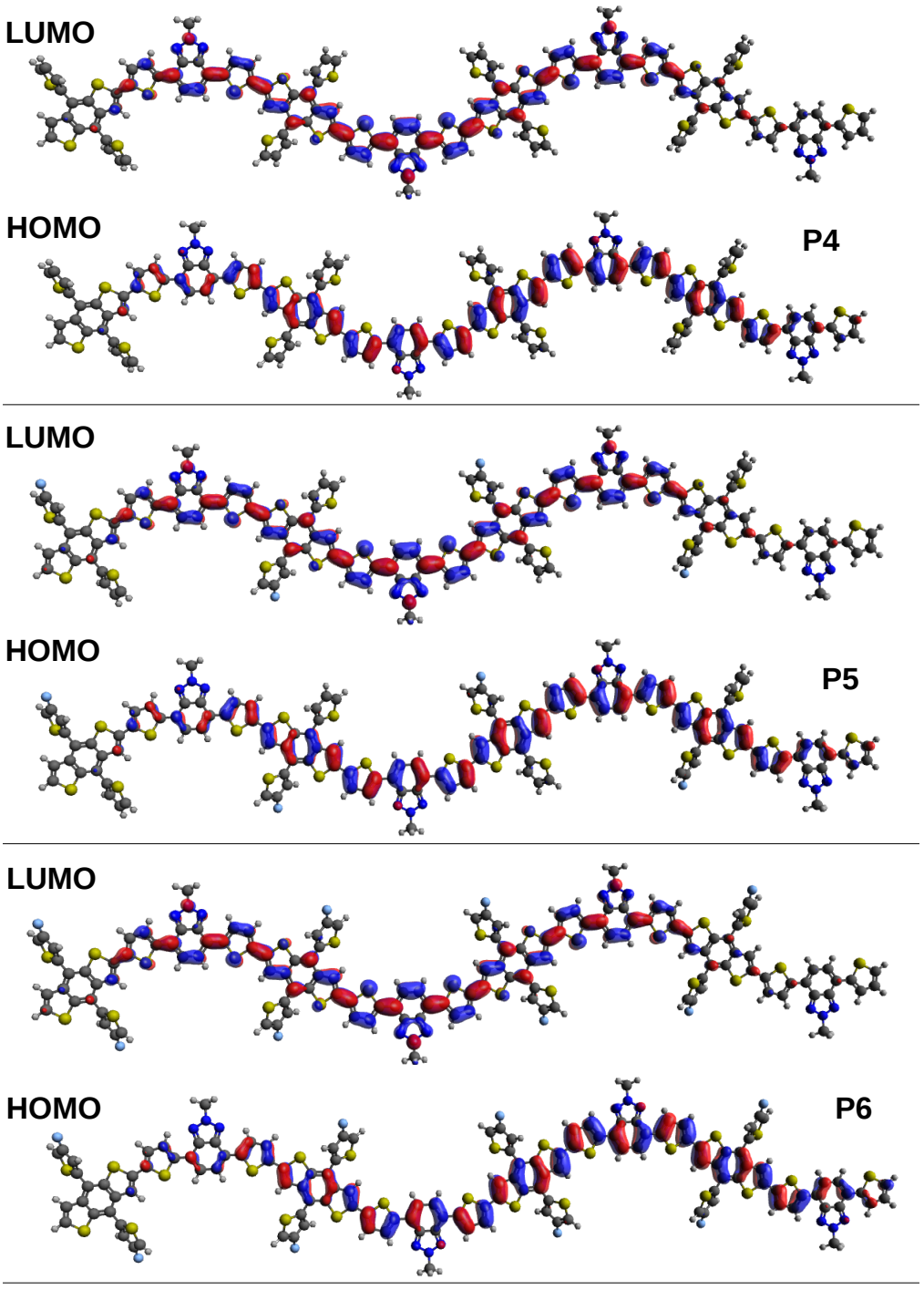

FIGURE A4: The contour plots of the HOMO and LUMO orbitals for the tetramers of **P4** -**P6** at HSE06/6-31G(d,p) level.

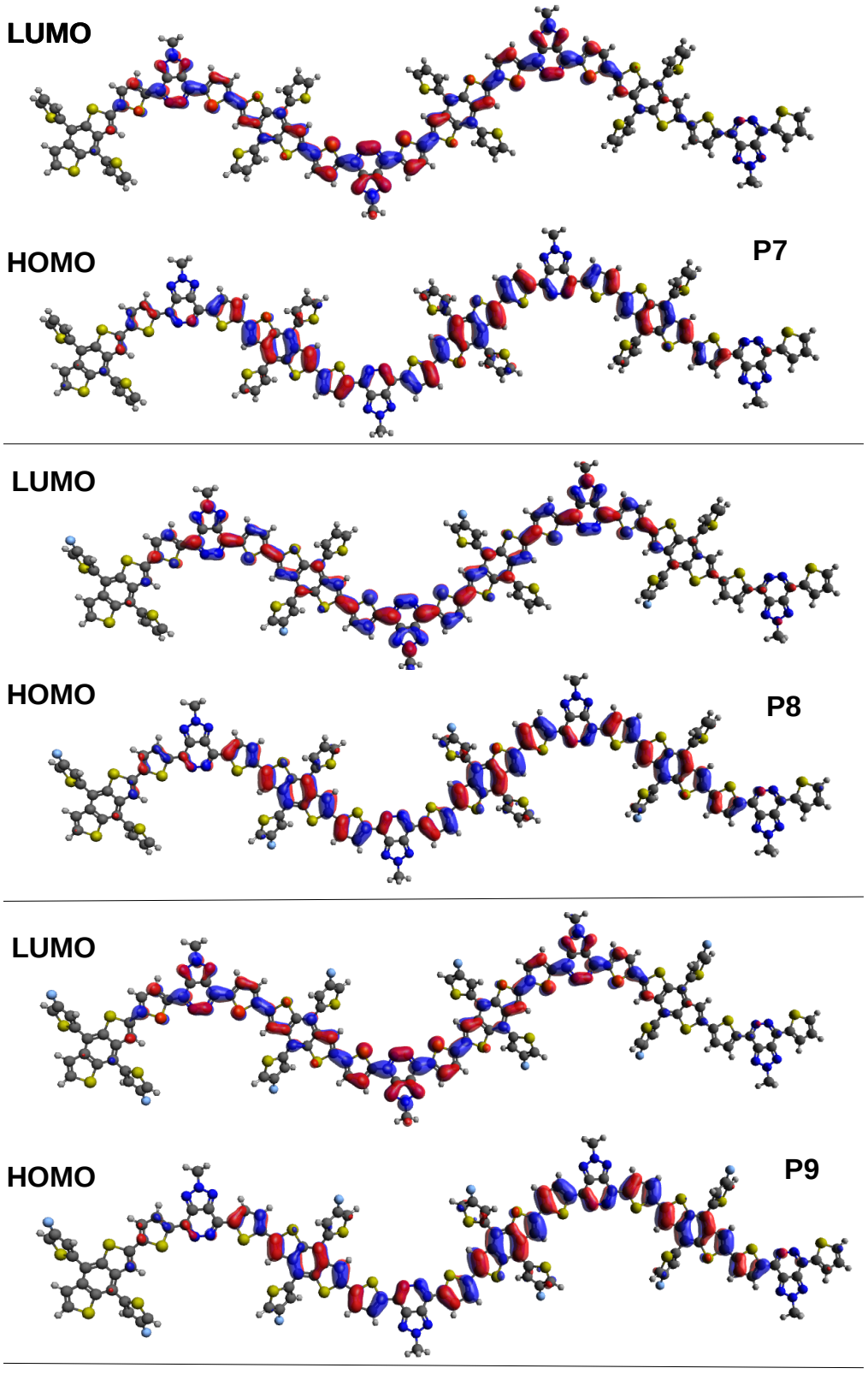

FIGURE A5: The contour plots of the HOMO and LUMO orbitals for the tetramers of **P7** -**P9** at HSE06/6-31G(d,p) level.

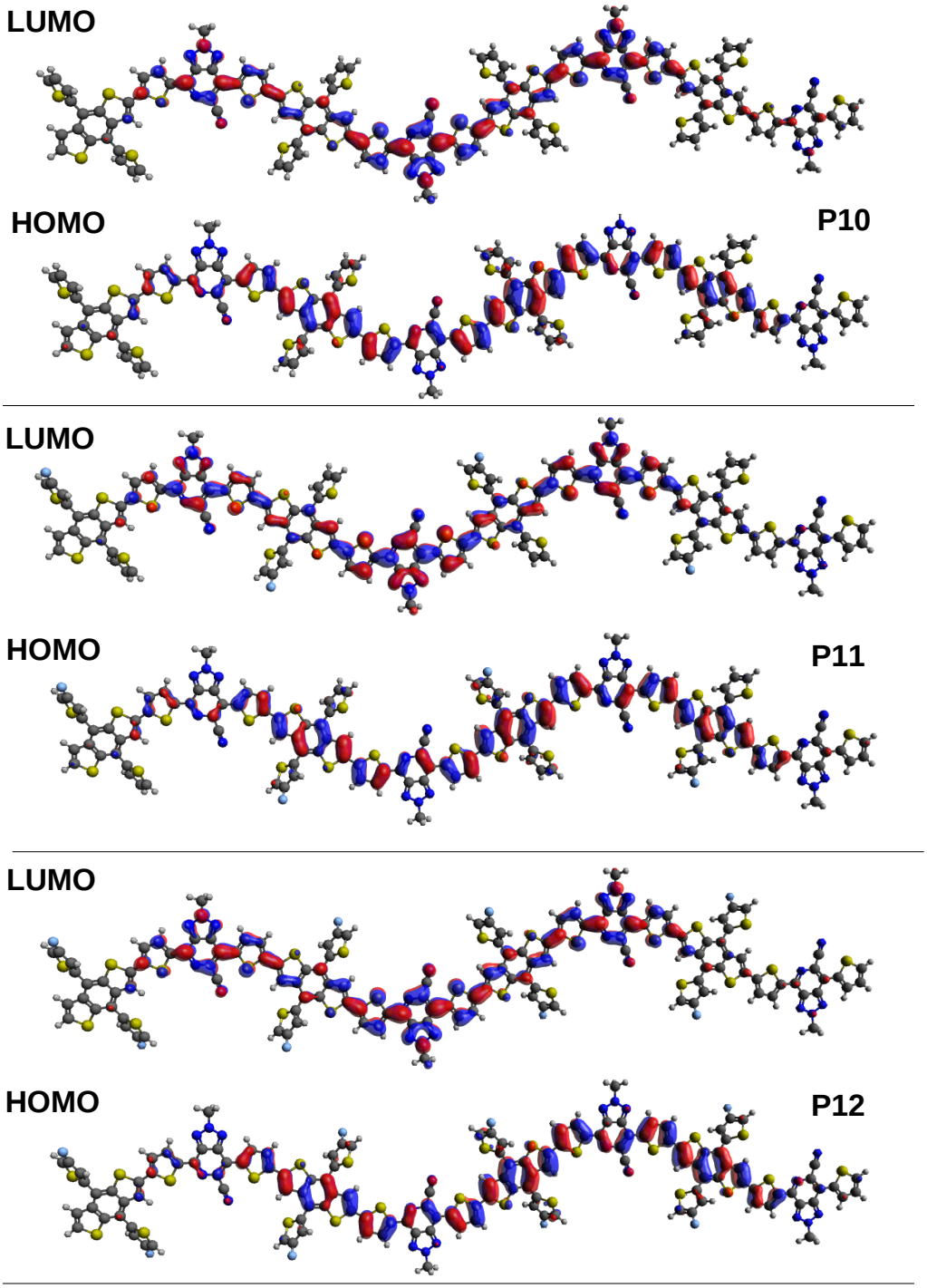

FIGURE A6: The contour plots of the HOMO and LUMO orbitals for the tetramers of **P10** -**P12** at HSE06/6-31G(d,p) level.

TABLE A5: Percentage contributions of different fragments to HOMOs ($\%_{HOMO}$) and LUMOs ($\%_{LUMO}$) of **P1**- **P12** tetramers.

Fragments	**P1**		**P2**		**P3**		**P4**		**P5**		**P6**	
	$\%_{HOMO}$	$\%_{LUMO}$	$\%_{HOMO}$	$\%_{LUMO}$	$\%_{HOMO}$	$\%_{LUMO}$	$\%_{HOMO}$	$\%_{LUMO}$	$\%_{HOMO}$	$\%_{LUMO}$	$\%_{HOMO}$	$\%_{LUMO}$
1	1.62	1.62	2.12	1.23	2.04	0.76	2.54	1.94	2.95	3.81	2.85	3.82
2	11.44	9.48	12.34	9.91	16.47	6.00	11.17	9.40	11.77	9.49	11.27	9.45
3	18.13	11.82	19.23	12.33	21.89	8.50	18.09	11.28	19.20	11.58	19.25	11.38
4	10.66	4.22	11.23	4.35	8.45	3.26	10.83	4.51	11.86	4.47	11.88	4.97
5	1.84	2.69	1.99	2.53	1.98	2.16	1.74	2.75	1.62	2.84	1.72	2.94
6	3.83	4.44	3.85	4.58	3.87	4.85	3.62	4.60	3.52	4.52	3.54	4.53
7	6.85	8.49	6.75	8.46	6.65	7.08	6.58	8.97	6.57	8.77	6.55	8.37
8	8.20	9.03	8.45	9.36	8.20	9.14	8.19	9.23	8.29	9.73	8.99	9.78
9	8.17	6.80	8.32	6.92	8.20	6.85	8.07	6.80	8.27	6.90	8.57	6.95
10	6.69	5.10	6.93	5.13	6.95	5.20	6.59	5.20	6.69	5.40	6.79	5.42
11	3.42	1.29	3.45	1.35	2.28	1.62	3.32	1.27	3.34	1.29	3.84	1.25
12	0.53	0.31	0.51	0.33	0.47	0.59	1.27	0.30	1.28	0.27	1.25	0.31
13	2.59	6.39	2.23	7.98	2.50	7.44	2.50	6.42	2.32	6.53	2.33	6.52
14	6.99	16.35	4.39	20.52	5.08	20.10	6.89	16.55	6.99	15.54	7.00	15.58
15	6.93	10.91	3.84	15.12	4.16	16.01	6.91	10.95	6.71	11.85	6.78	11.82
16	2.02	0.98	0.88	1.79	0.89	2.11	1.90	1.30	2.41	0.83	2.48	0.82
Fragments	**P7**		**P8**		**P9**		**P10**		**P11**		**P12**	
	$\%_{HOMO}$	$\%_{LUMO}$	$\%_{HOMO}$	$\%_{LUMO}$	$\%_{HOMO}$	$\%_{LUMO}$	$\%_{HOMO}$	$\%_{LUMO}$	$\%_{HOMO}$	$\%_{LUMO}$	$\%_{HOMO}$	$\%_{LUMO}$
1	2.09	1.50	2.07	1.84	2.05	1.46	2.43	1.33	2.41	1.32	2.64	1.63
2	16.20	7.49	16.21	7.84	16.12	7.85	16.94	7.11	16.84	7.09	16.58	7.04
3	24.09	9.68	24.08	9.58	23.01	9.50	23.74	9.05	23.54	9.03	22.33	9.43
4	12.64	3.93	12.53	3.96	12.20	3.90	11.70	3.90	11.60	3.89	11.05	3.78
5	1.55	2.60	1.53	2.65	1.54	2.62	1.65	2.38	1.62	2.35	1.52	2.33
6	3.84	4.56	3.82	4.55	3.80	4.53	3.99	3.64	3.97	3.62	3.94	3.65
7	6.05	8.36	6.12	8.35	6.11	8.32	6.08	7.04	6.05	7.02	6.02	7.21
8	8.75	9.26	8.74	9.21	8.24	9.17	7.40	7.66	7.42	7.63	7.41	7.62
9	8.13	6.98	8.12	6.96	8.15	6.93	7.66	6.18	7.62	6.21	7.61	6.22
10	6.84	5.23	6.85	5.21	6.82	5.20	8.12	6.23	8.14	6.22	8.12	6.21
11	3.51	1.33	3.52	1.32	3.52	1.32	2.05	1.13	2.05	1.09	2.03	1.08
12	0.50	0.34	0.51	0.36	0.50	0.36	0.45	0.54	0.44	0.52	0.42	0.51
13	1.64	8.31	1.61	8.38	1.59	8.28	2.49	7.42	2.47	7.32	2.45	7.33
14	4.18	19.87	4.18	19.21	4.16	19.12	5.01	19.65	5.03	19.20	5.02	20.01
15	3.76	13.73	3.74	13.24	3.72	13.22	4.12	16.02	4.11	16.12	4.07	16.31
16	0.91	1.68	0.90	1.65	0.89	1.64	0.87	2.13	0.86	2.11	0.75	2.08

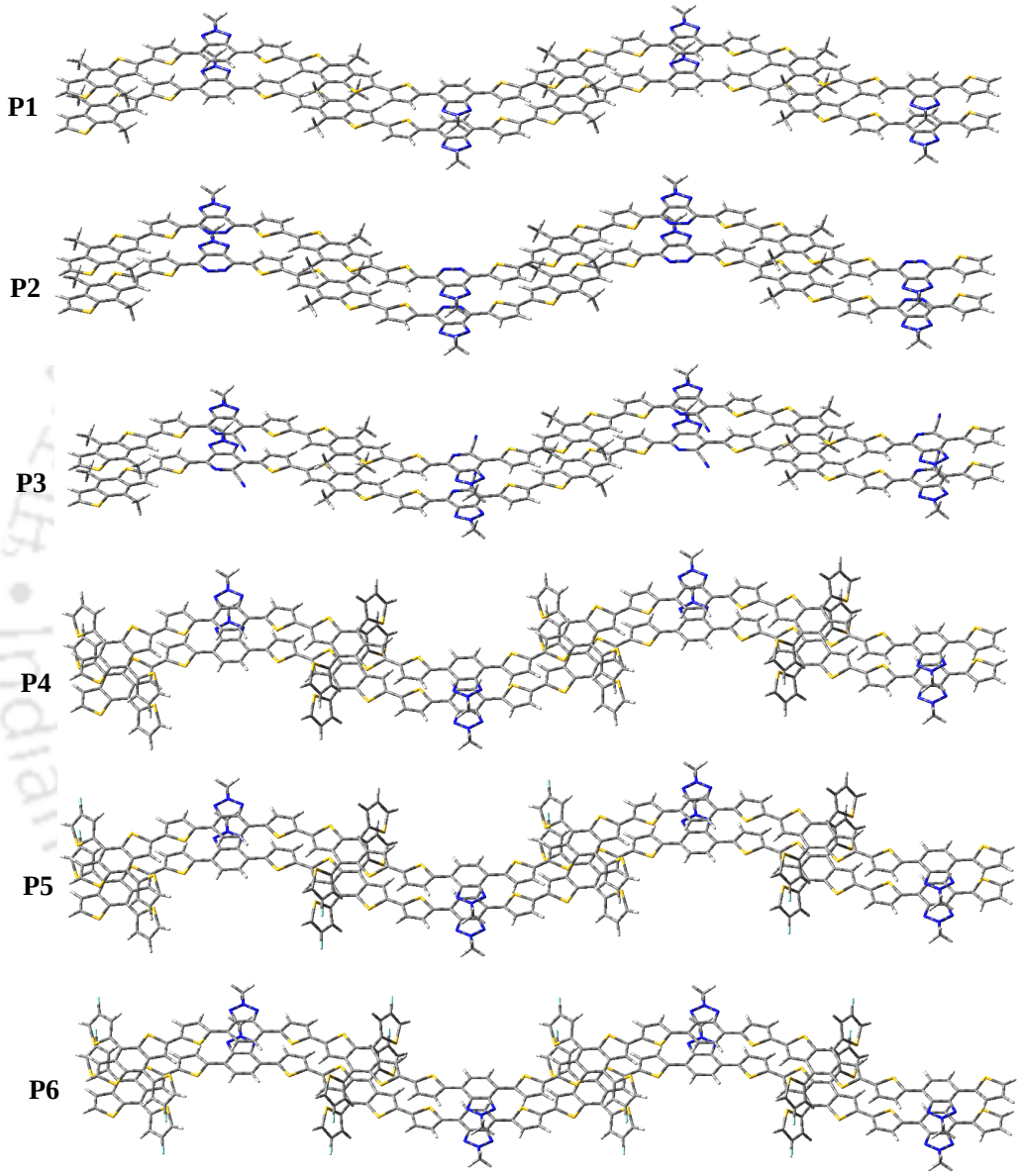

FIGURE A7: Three-dimensional π-stacked structures of two adjacent tetramer fragments for **P1** to **P6**.

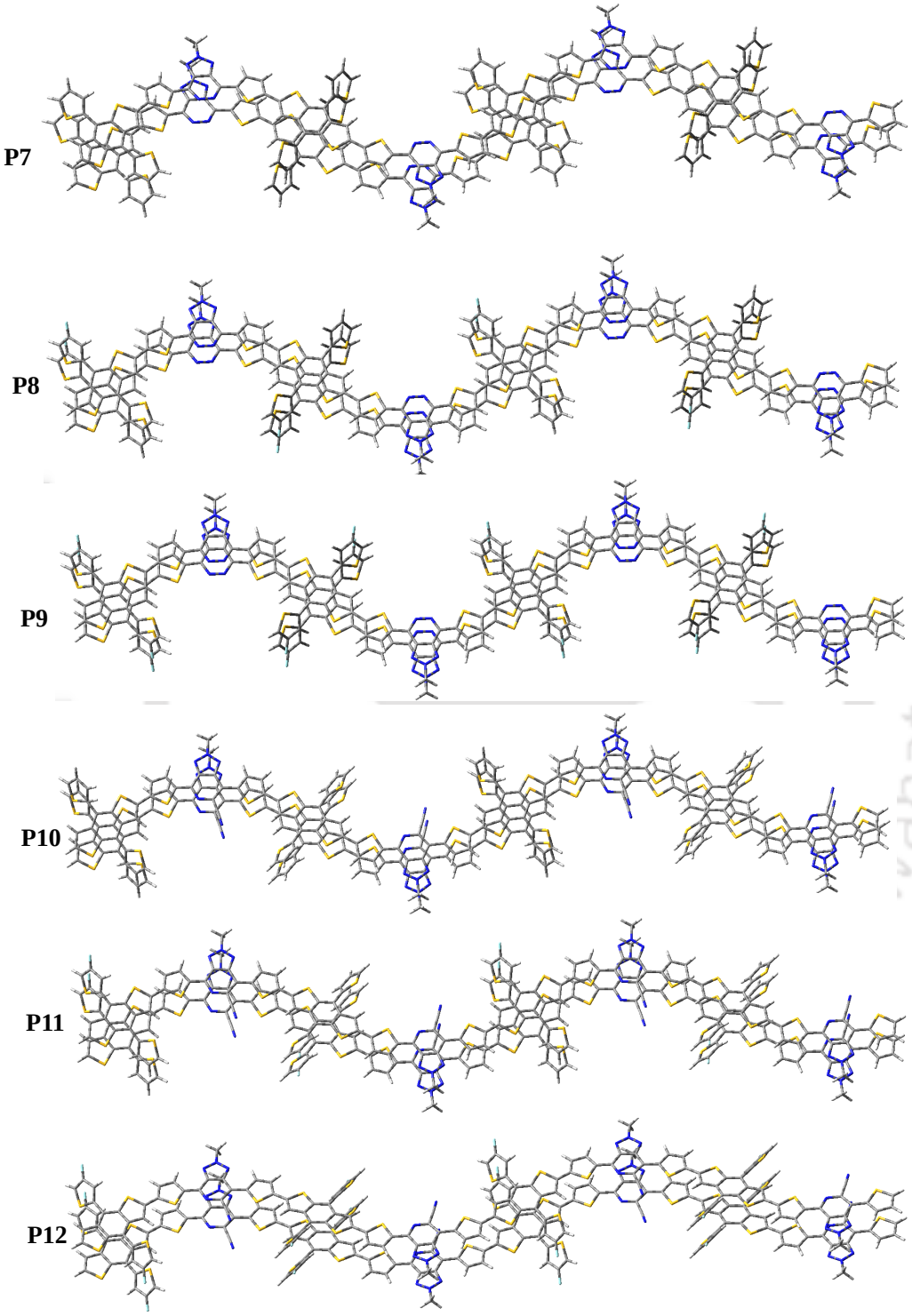

FIGURE A8: Three-dimensional π-stacked structures of two adjacent tetramer fragments for **P7** to **P12**.

Appendix B

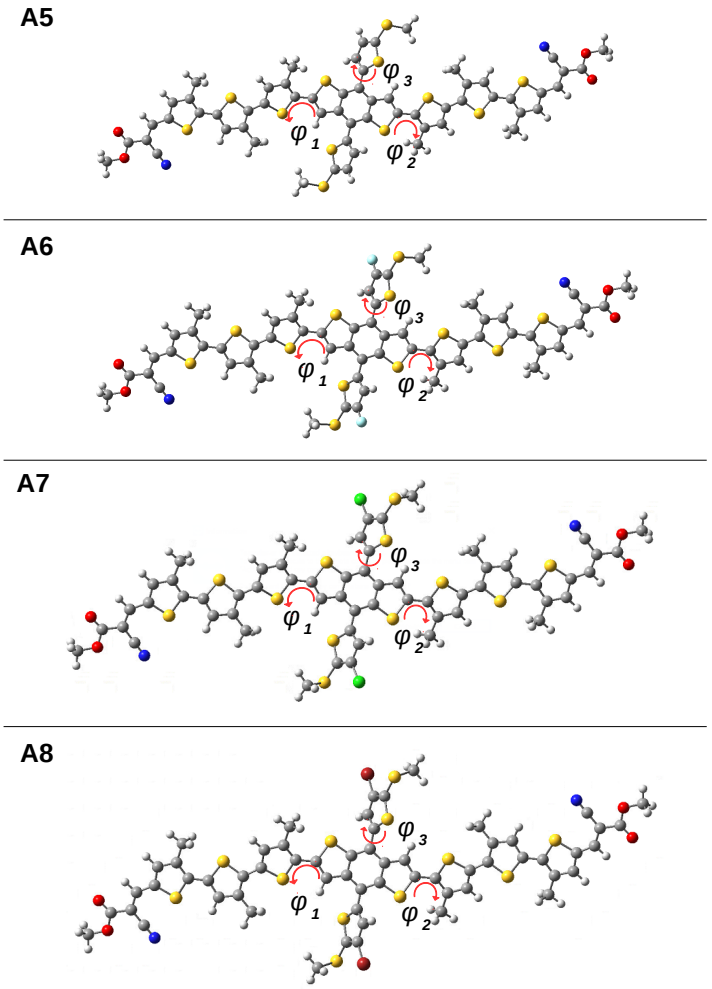

FIGURE B1: Optimized ground state geometries for **A5**-**A8** calculated at PBE0/6-31G(d,p) level.

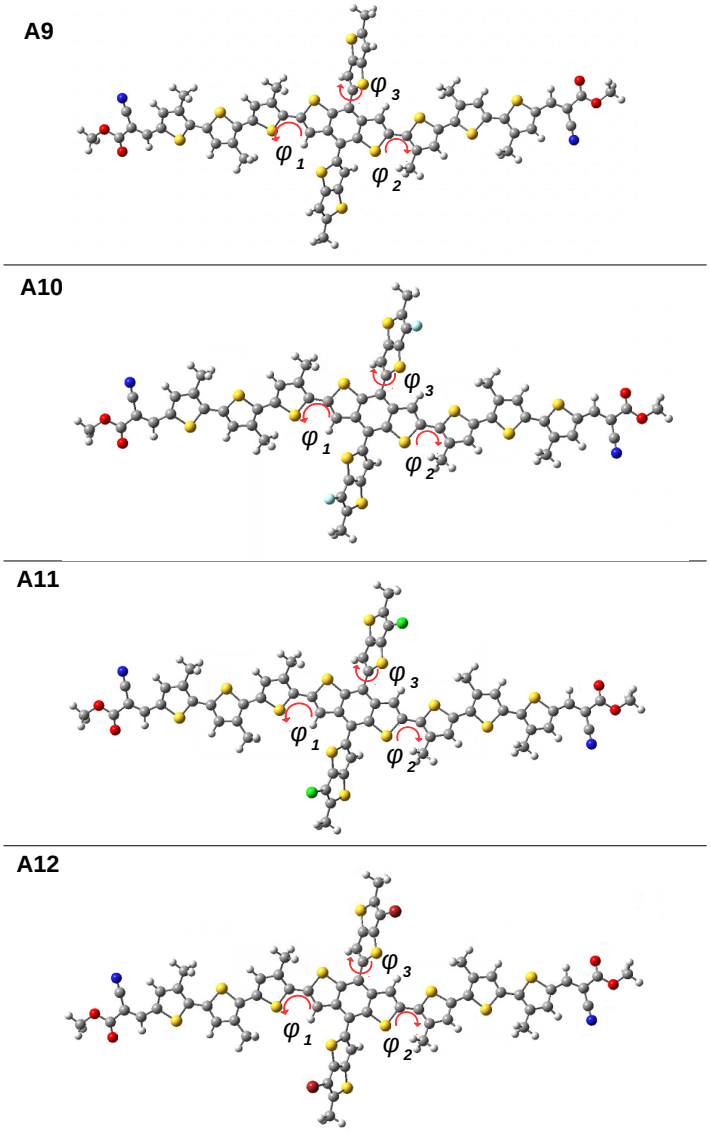

FIGURE B2: Optimized ground state geometries for **A9**-**A12** calculated at PBE0/6-31G(d,p) level.

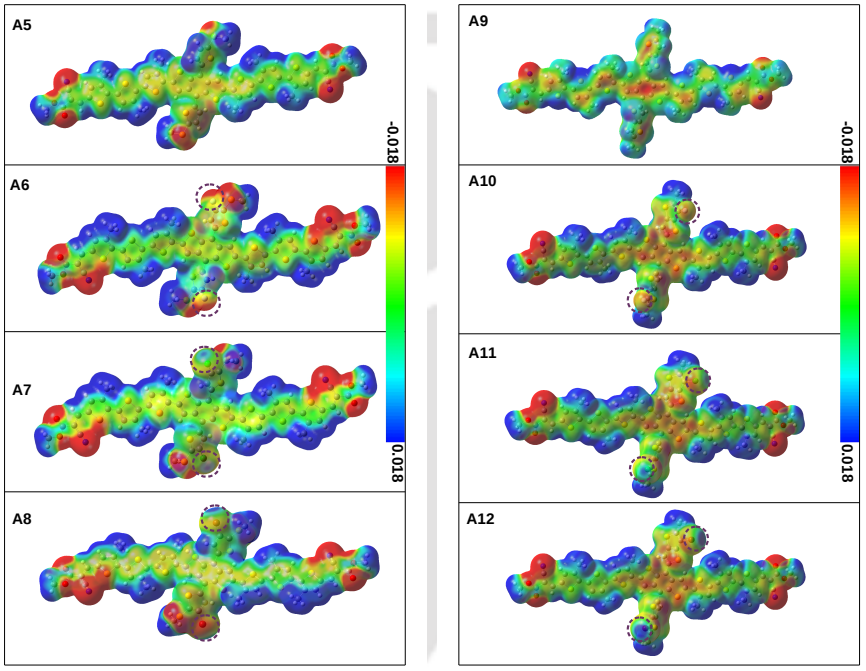

FIGURE B3: The molecular electrostatic potentials (ESPs) drawn on isosurfaces of electron density for **A5-A8**, and **A9-A12**. An isovalue of 0.001 is used. Brown colored circles indicate the locations of the halogen atoms.

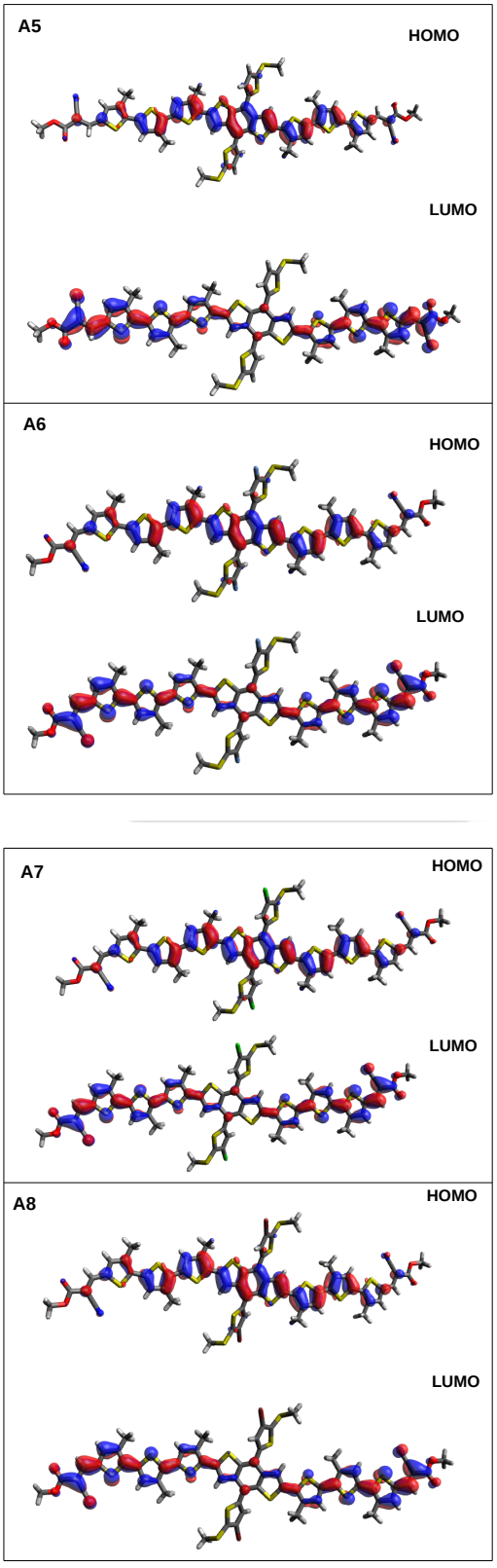

FIGURE B4: HOMOs and LUMOs of the **A5**-**A6** and **A7**-**A8** computed at the PBE0/6-31G(d,p) level (isovalue of 0.02 a.u.).

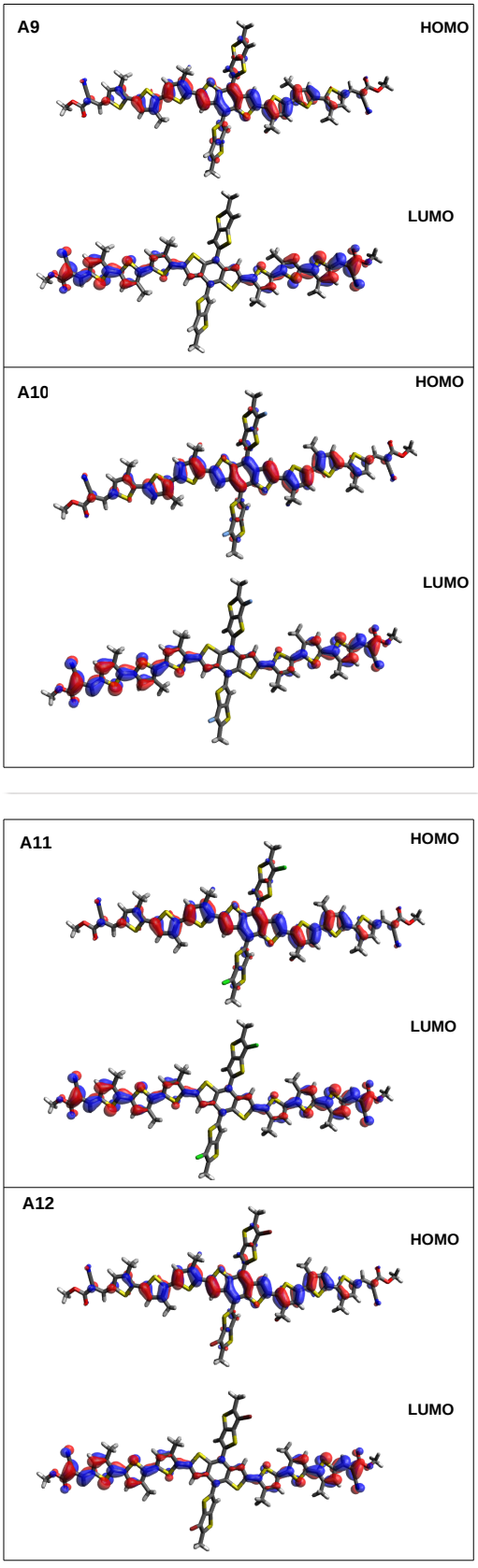

FIGURE B5: HOMOs and LUMOs of the **A9**-**A10** and **A11**-**A12** computed at the PBE0/6-31G(d,p) level (isovalue of 0.02 a.u.).

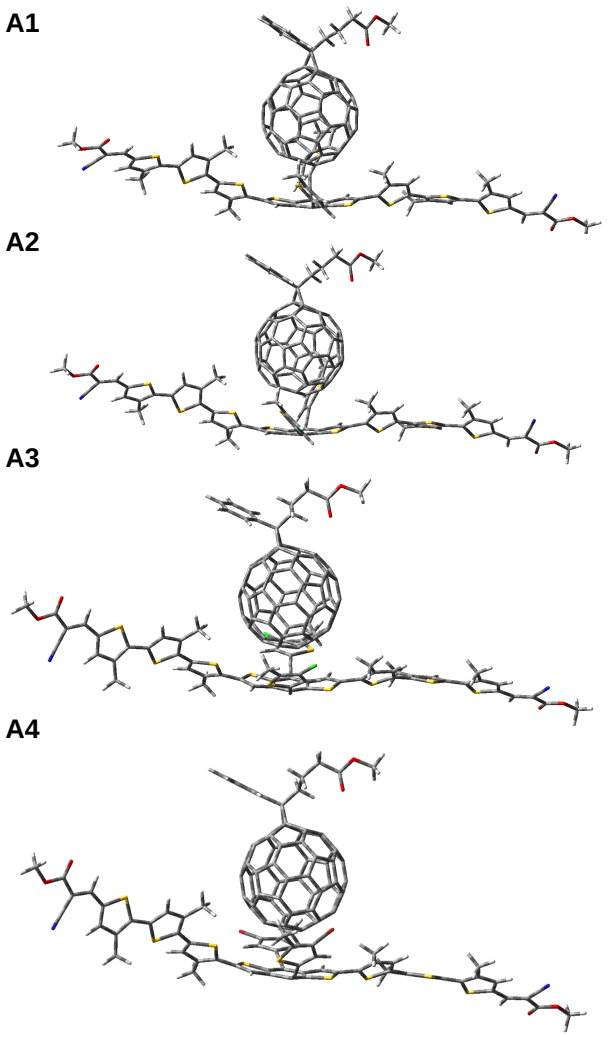

FIGURE B6: Optimized geometries of **A1-A4/PCBM** composite systems.

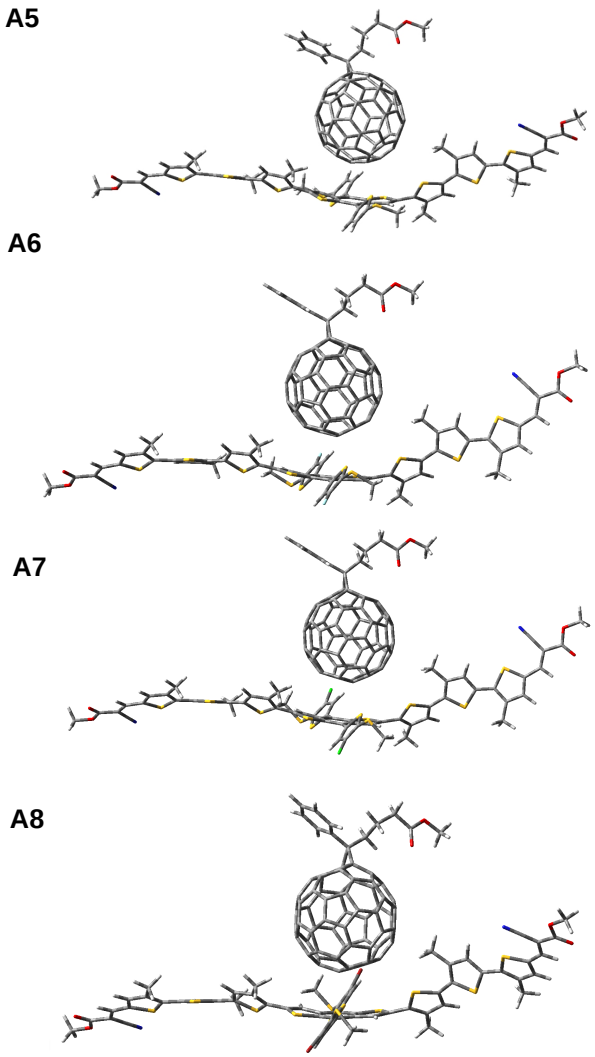

FIGURE B7: Optimized geometries of **A5-A8/PCBM** composite systems.

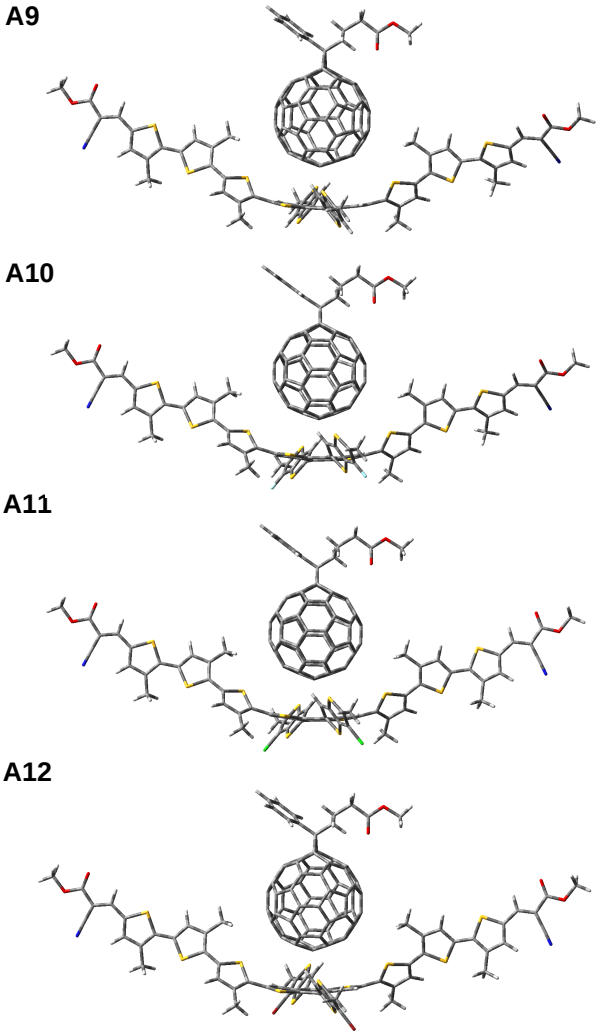

FIGURE B8: Optimized geometries of **A9-A12/PCBM** composite systems.

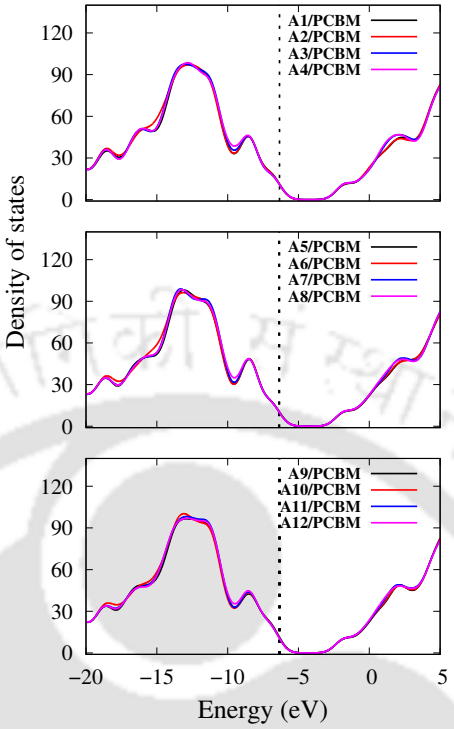

FIGURE B9: TDOS for **A1-A12/PCBM** systems.

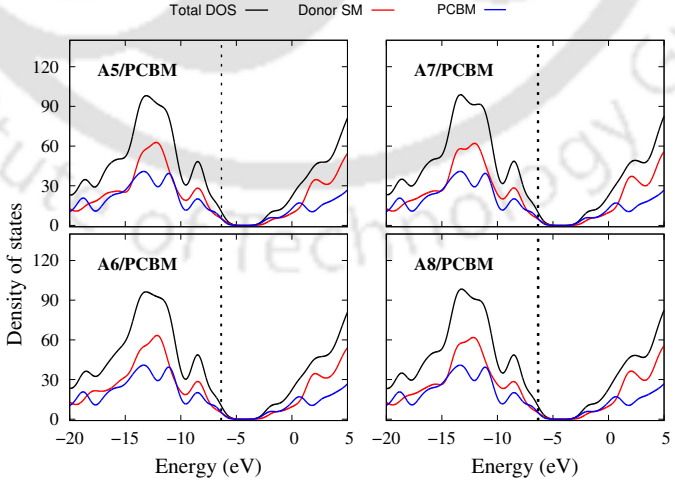

FIGURE B10: TDOS, and PDOSs from SM donor and **PCBM** acceptor fragments for **A5-A8/PCBM** blends.

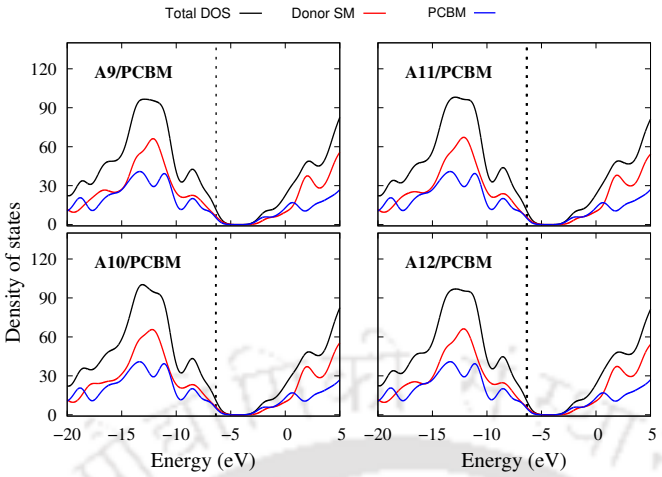

FIGURE B11: TDOS, and PDOSs from SM donor and **PCBM** acceptor fragments for **A9**-**A12**/**PCBM** blends.

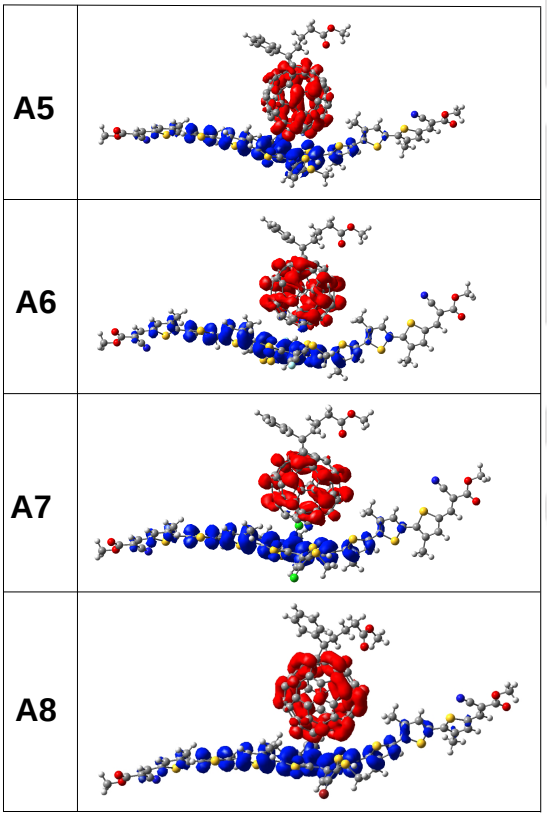

FIGURE B12: Charge density difference (CDD) maps for the S_{16}, S_{19}, S_{19}, S_{15} states of **A5**, **A6**, **A7** and **A8** composite systems, respectively. These states are the first ICT states for these systems. Red and blue colors represent electrons and holes, respectively.

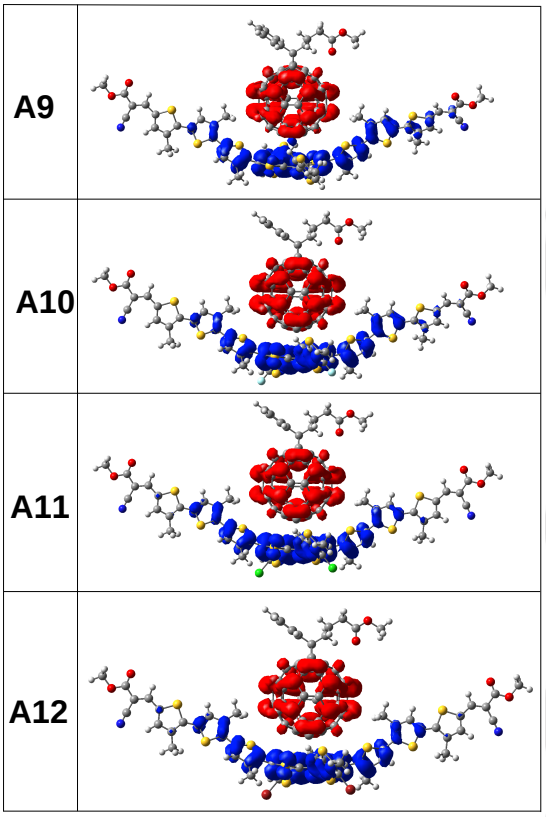

FIGURE B13: Charge density difference (CDD) maps for the first ICT states of **A9**, **A10**, **A11** and **A12** composite systems. For each of these four composites, S_{17} is the first ICT state. Red and blue colors represent electrons and holes, respectively.

Appendix C

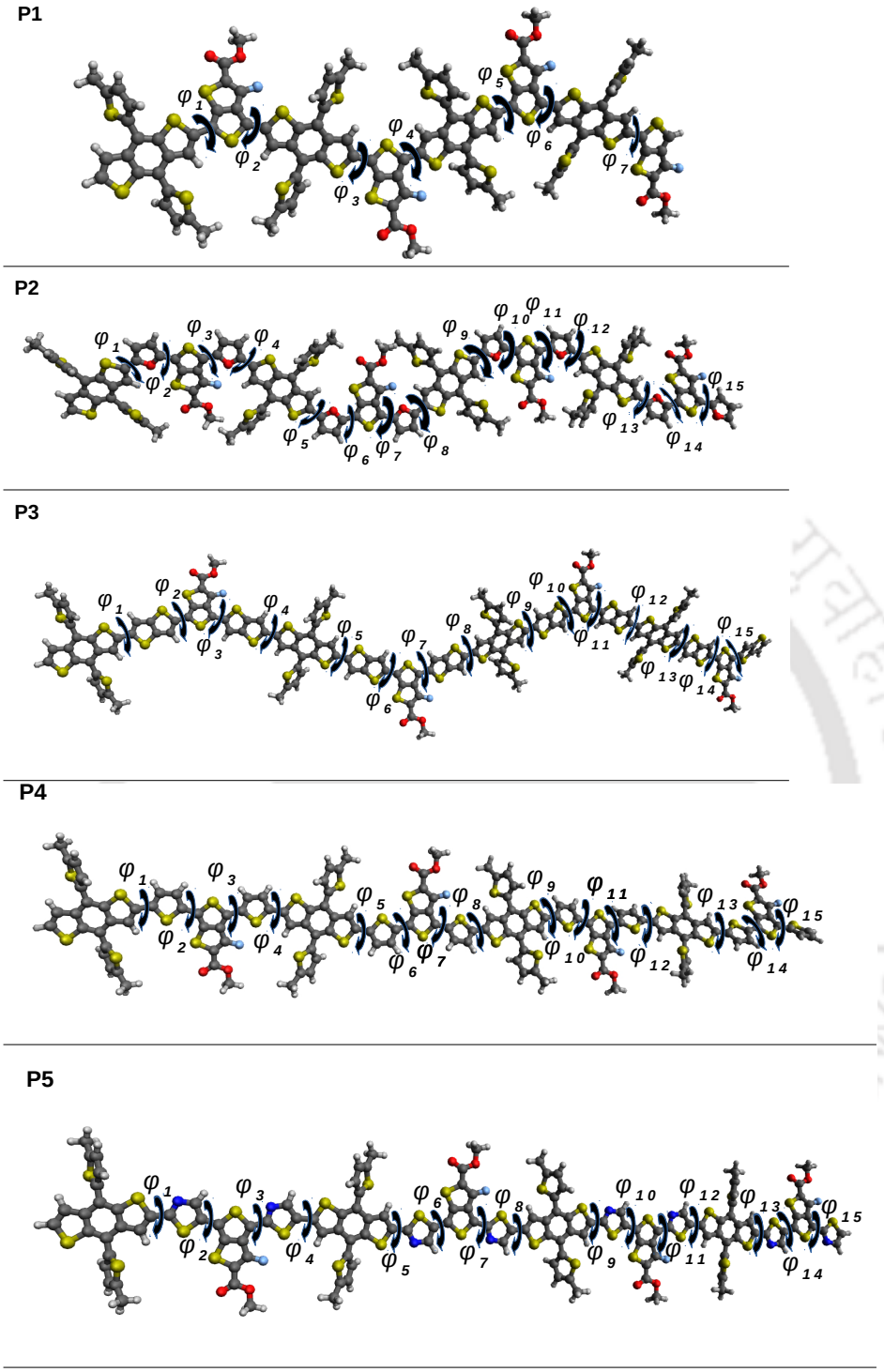

FIGURE C1: Various dihedral angles used to analyze the changes in the geometries upon π-bridge insertion are showin in the figure. Colour code: white (H), grey (C), yellow (S), red (O) and cyan (F).

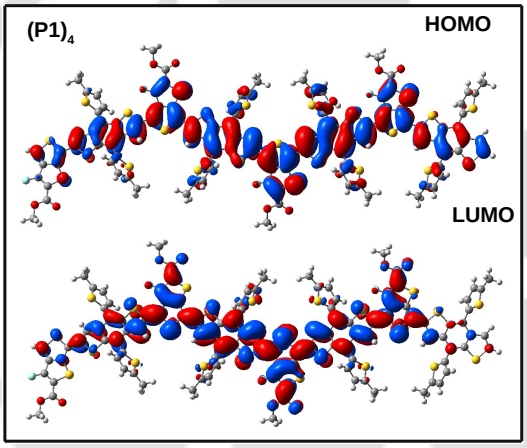

FIGURE C2: HOMO and LUMO for $(\mathbf{P1})_4$ at CPCM-PBE0/6-311G(d,p) level.

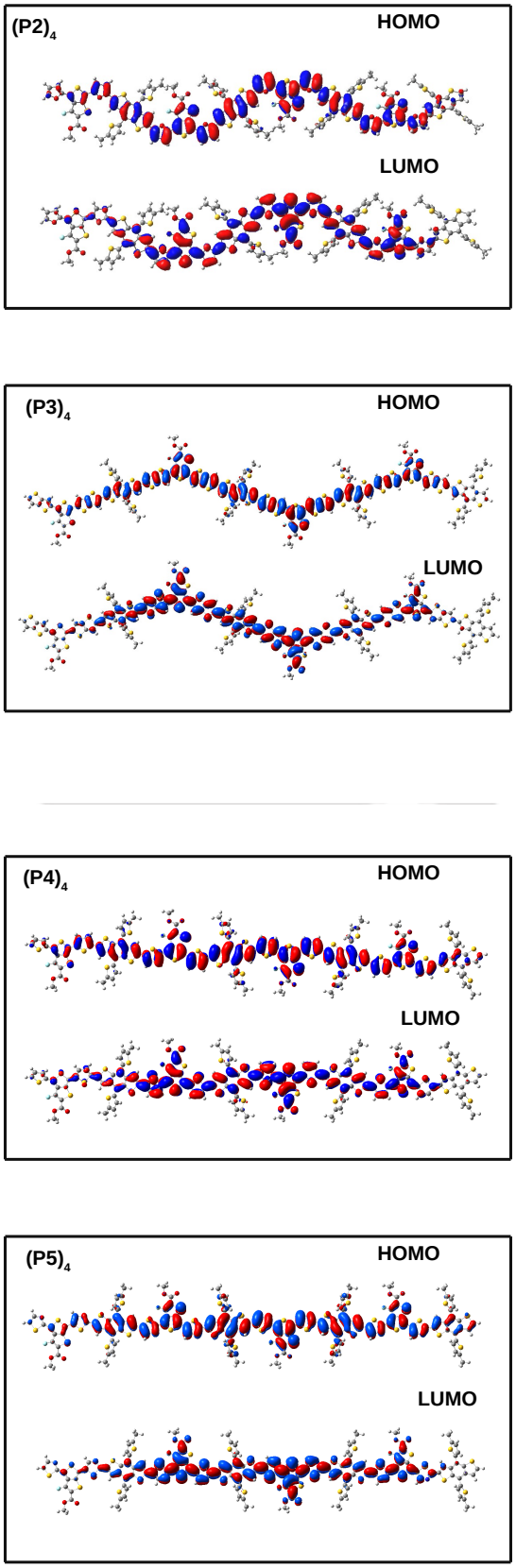

FIGURE C3: HOMOs and LUMOs for $(\mathbf{P2})_4$, $(\mathbf{P3})_4$, $(\mathbf{P4})_4$ and $(\mathbf{P5})_4$ at CPCM-PBE0/6-311G(d,p) level.

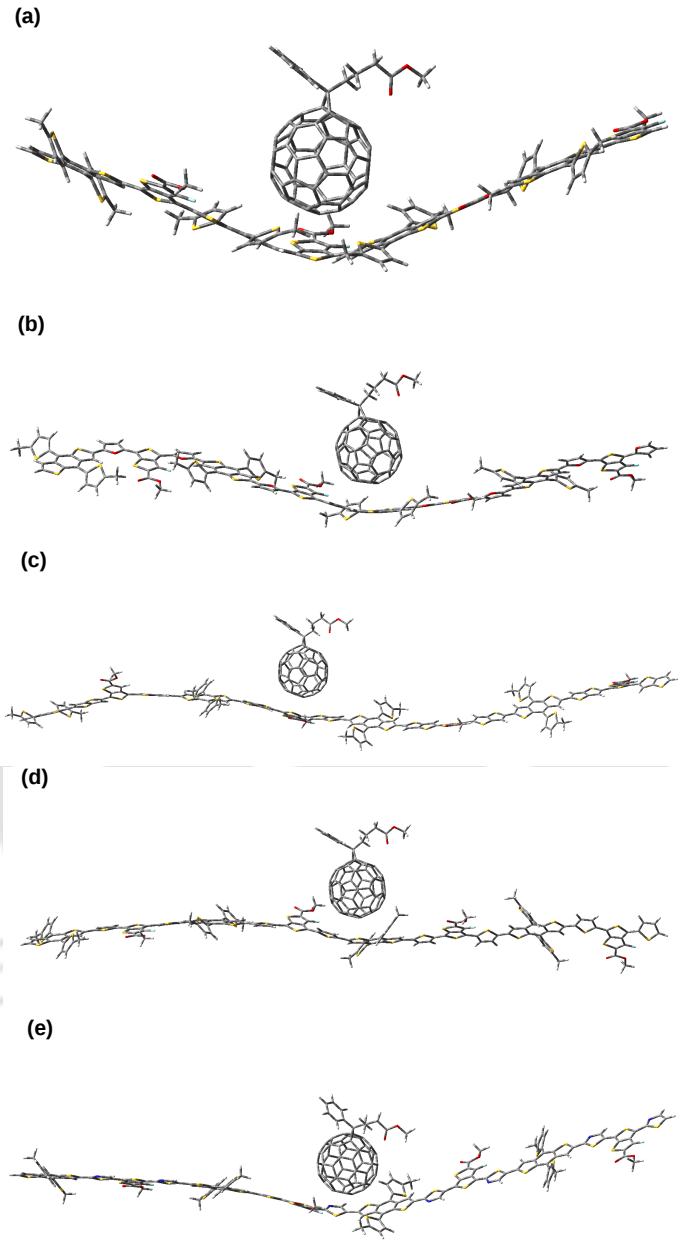

FIGURE C4: Optimized geometries of **P1-P5/PCBM** composite systems. a-e are for **P1-P5/PCBM**, respectively. Results are obtained at RI-PBE-D3/def2-SV(P) level.

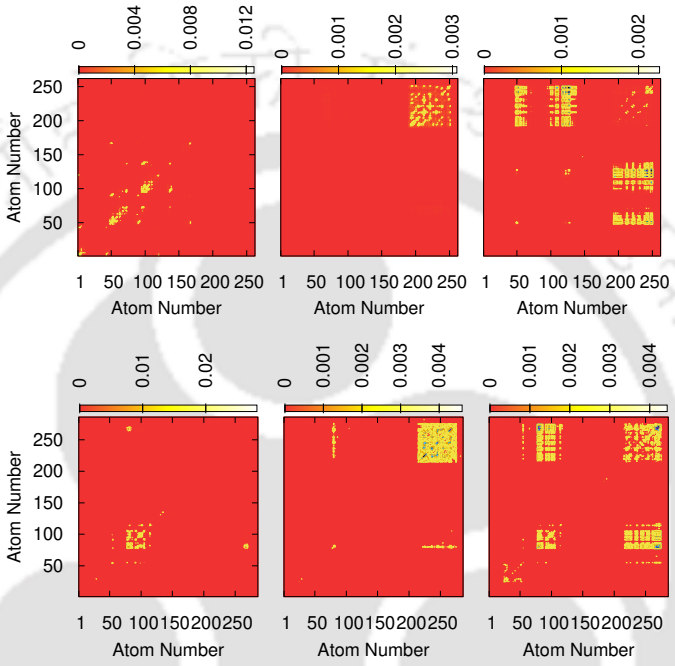

FIGURE C5: Top panel: Two-dimensional site representation of the transition density matrix (TDM) for S_1, S_4, and S_6 excited states (from left to right) of the **P2/PCBM** composite system. Bottom panel: Two-dimensional site representation of the transition density matrix (TDM) for S_1, S_4, and S_6 excited states (from left to right) of the **P3/PCBM** composite system. Both X and Y- axes represent the atom numbers. Atom numbers 1-188 are for the donor **P2** and from 189 onwards are for the acceptor **PCBM**. Hydrogen atoms are ignored here. Atom numbers 1-212 are for the donor **P3** and from 213 onwards are for the acceptor **PCBM**. Hydrogen atoms are ignored here. These results are obtained at TD-CPCM-CAMB3LYP/6-311G(d,p) level of theory.

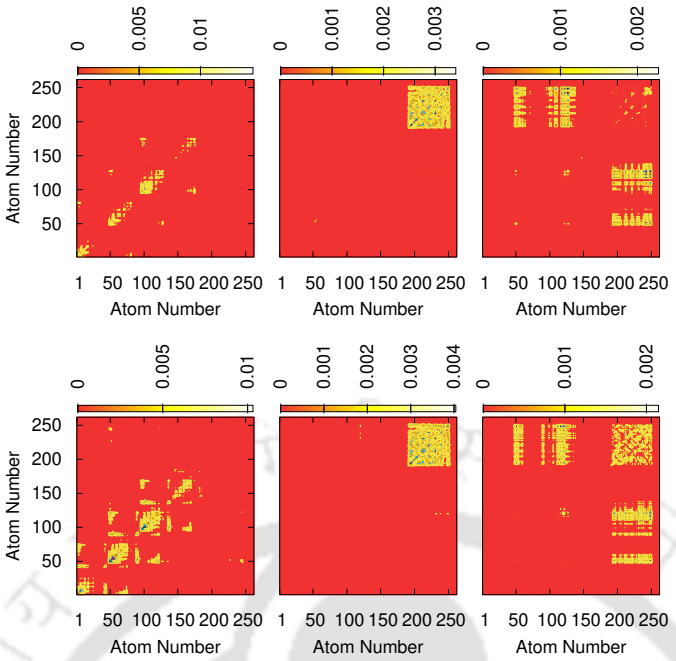

FIGURE C6: Top panel: Two-dimensional site representation of the transition density matrix (TDM) for S_1, S_4, and S_9 excited states (from left to right) of the **P4**/**PCBM** composite system. Both X and Y- axis represent the atom numbers. Atom numbers 1-188 are for the donor **P4** and from 189 onwards are for the acceptor **PCBM**. Hydrogen atoms are ignored here. Bottom panel: Two-dimensional site representation of the transition density matrix (TDM) for S_1, S_4, and S_{11} excited states (from left to right) of the **P5**/**PCBM** composite system. Atom numbers 1-188 are for the donor **P5** and from 189 onwards are for the acceptor **PCBM**. Hydrogen atoms are ignored here. These results These results are obtained at TD-CPCM-CAMB3LYP/6-311G(d,p) level of theory.

TABLE C1: Vertical IPs, EAs, interfacial lowest excitation energies ($E^1_{\mathrm{g,Blend}}$) and exciton binding energies (E_{b}) of the D/A blends.

Compounds	IP (eV)	EA (eV)	$E^1_{\mathrm{g,Blend}}$	E_{b}
P1/**PCBM**	5.61	3.44	1.89	0.28
P2/**PCBM**	5.48	3.41	2.00	0.07
P3/**PCBM**	5.61	3.45	1.97	0.19
P4/**PCBM**	5.58	3.42	2.01	0.15
P5/**PCBM**	5.88	3.47	2.00	0.41

Appendix D

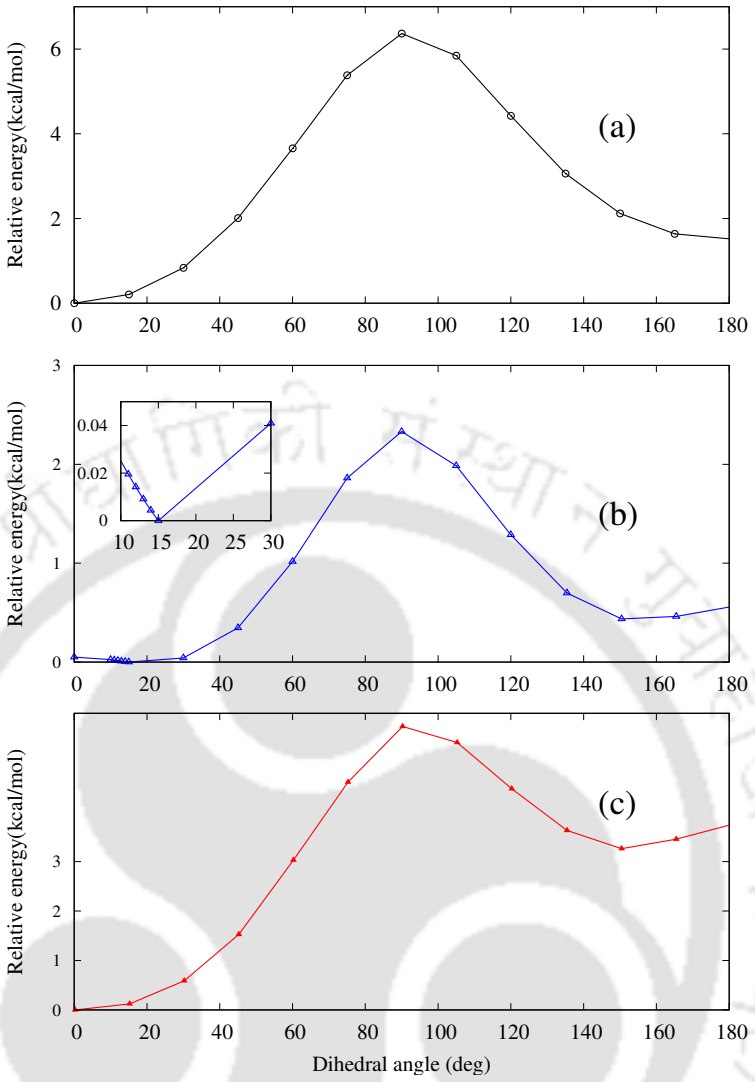

FIGURE D1: Relaxed torsional potentials along ϕ_2 (a), ϕ_3 (b) and ϕ_4 (c) dihedral angles **TzP1**. The inset in (b) shows a zoomed version of the full curve between 10 and 30 degrees, and clearly indicates the minimum at $\sim$ 15 deg. All the above relaxed torsional scans are carried out at the M06/6-311G(d,p) level. Instead of taking the full dimer for these scans, only the two rings involved in making ϕ_2, ϕ_3 or ϕ_4 are considered.

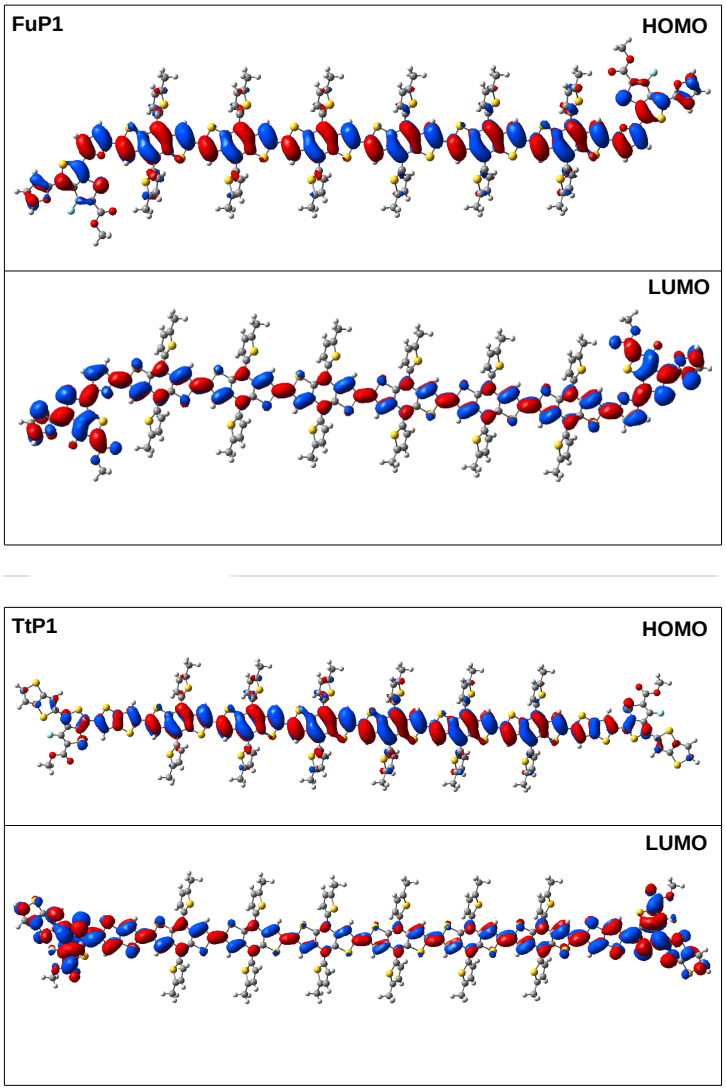

FIGURE D2: HOMOs and LUMOs for **FuP1-TtP1** computed at the M06/6-311G(d,p) level (isovalue of 0.01 a.u.).

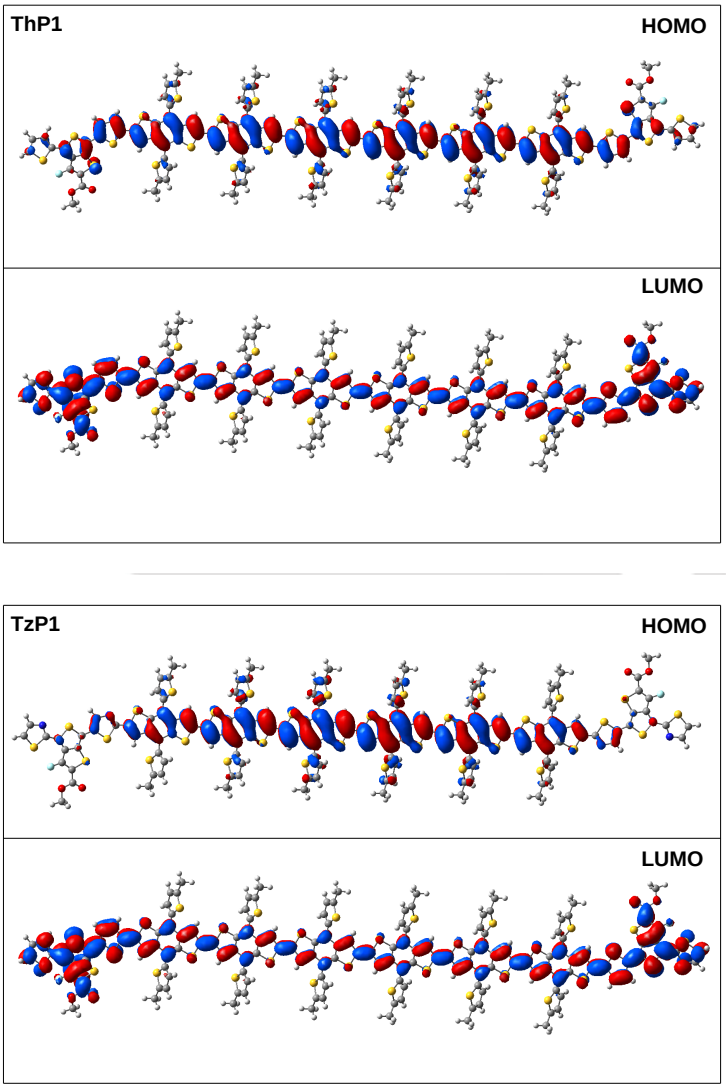

FIGURE D3: HOMOs and LUMOs for **ThP1-TzP1** computed at the M06/6-311G(d,p) level (isovalue of 0.01 a.u.).

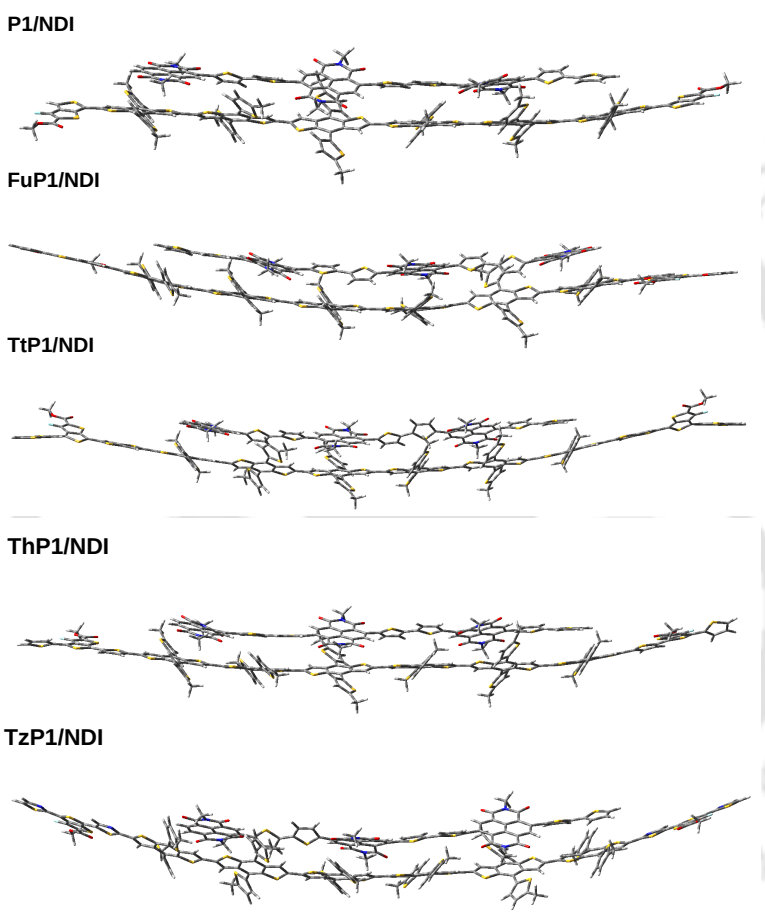

FIGURE D4: Optimized geometries of **P1**-**TzP1**/**NDI** blend systems.

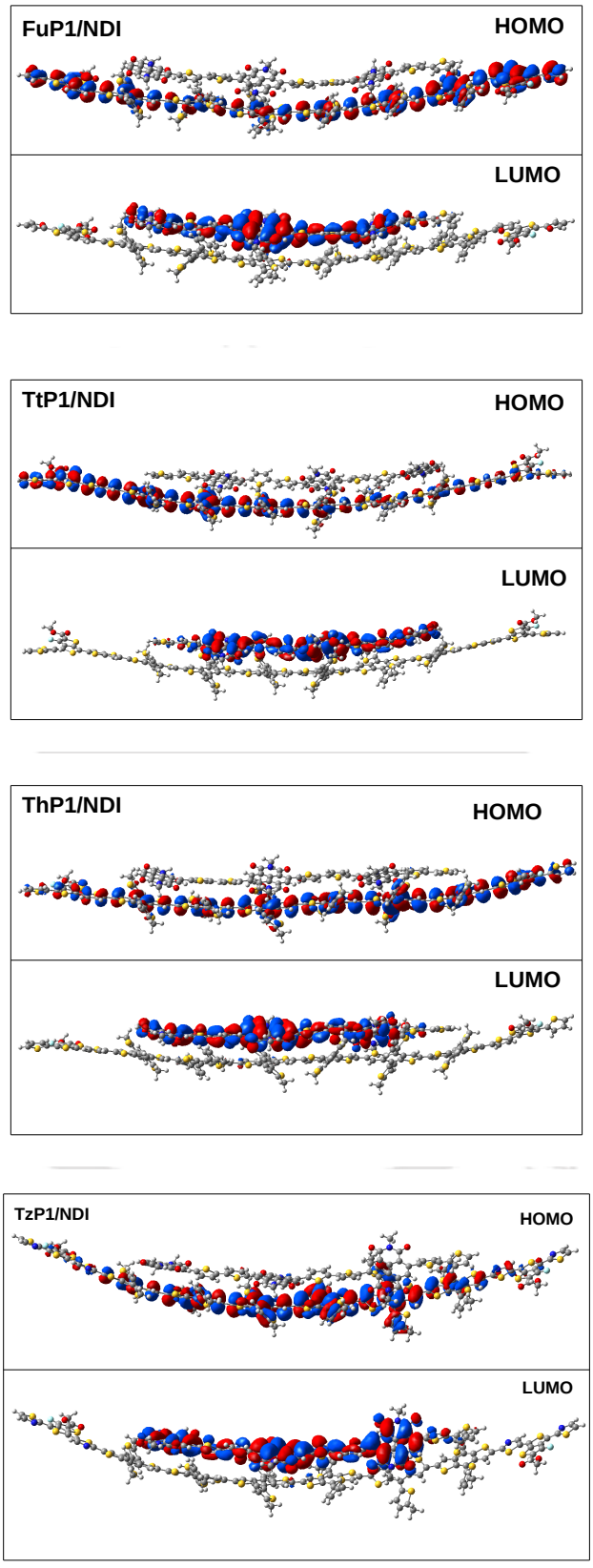

FIGURE D5: HOMOs and LUMOs for **FuP1-TzP1/NDI** blend system computed at M06/6- 311G(d,p) level.

List of articles published/submitted

1. Mohd Shavez and Aditya N. Panda, Assessing effects of different π-bridges on photovoltaic performance of random benzodithiophene-thienothiophene donor and non-fullerene acceptor based active layer, *J. Phys. Chem. A*, **2021**, 125, 9852–9864.

2. Mohd Shavez, Anuj Kumar Ray and Aditya N. Panda, Effect of halogenation of the side chains in donor-acceptor based small molecules for photovoltaic applications: Energetics and charge-transfer properties from DFT/TDDFT studies, *Chemistry Select*, **2021**, 6, 5254–5265.

3. Mohd Shavez and Aditya N. Panda, Effects of π-bridge units on the properties of donor-π-acceptor type benzodithiophene-thienothiophene based polymers for organic solar cells, *Chemical Physics Letters*, **2020**, 756, 137810–137818.

4. Mohd Shavez, Juri Goswami and Aditya N. Panda, Effect of fluorination of the donor unit on the properties of benzodithiophene-triazole based donor-acceptor systems for polymer solar cells: A computational investigation, *Computational and Theoretical Chemistry*, **2019**, 1165, 112564–112572.

Conferences Attended

1. Poster presentation in Frontiers in Chemical Sciences 2018, IIT Guwahati

2. Poster presentation in Research Conclave 2018, IIT Guwahati

3. Poster presentation in TCS 2021, IISER Kolkata